INFRARED ATTENUATED TOTAL REFLECTION SPECTROSCOPY FOR MONITORING BIOLOGICAL SYSTEMS

A Thesis
Presented to
The Academic Faculty

by

Liqun Wang

In Partial Fulfillment
of the Requirements for the Degree
Doctor of Philosophy in Chemistry

Georgia Institute of Technology
May 2009

INFRARED ATTENUATED TOTAL REFLECTION SPECTROSCOPY FOR MONITORING BIOLOGICAL SYSTEMS

Approved by:

Dr. Boris Mizaikoff, Advisor
School of Chemistry and Biochemistry
Georgia Institute of Technology

Dr. Facundo M. Fernandez
School of Chemistry and Biochemistry
Georgia Institute of Technology

Dr. Robert Whitten
School of Chemistry and Biochemistry
Georgia Institute of Technology

Dr. Richard A. Palmer
Department of Chemistry
Duke University

Dr. Thomas Orlando
School of Chemistry and Biochemistry
Georgia Institute of Technology

Date Approved: December 16, 2008

This thesis is dedicated to my family

ACKNOWLEDGEMENTS

I wish to thank my advisor and mentor Dr. Boris Mizaikoff for giving me the opportunity to work in the Applied Sensors Laboratory at Georgia Institute of Technology. Dr. Boris Mizaikoff and Dr. Christine Kranz are an excellent team; their guidance, inspiration and encouragement are deeply appreciated. I would also like to give my thanks to all past and present members of ASL for their support and help throughout the work.

This thesis work is partially in collaboration with Dr. Richard Palmer at Duke University. I am grateful to his endless help and advice. Special thanks are extended to everyone at Duke University for helping me during my stay there, especially Jessica Chapman, Todd Alter, Aya Eguchi, Dr. Olaf von Ramm, Dr. Brett Hooper, Ellen Dixon-Tulloch.

I would also like to thank Dr. Facundo Fernandez, Dr. Thomas Orlando, and Dr. Robert Whetten for serving as committee members and providing me the critical feedback and input.

In addition, I would also like to thank Dr. Janusz Kowalik from school of Chemistry at Georgia Institute of Technology for collaborative work on the synthesis of dithiophenylpyrrole.

At last, this would not have been possible without the unconditional love and support from my family and friends.

TABLE OF CONTENTS

LIST OF TABLES

LIST OF FIGURES

Page

LIST OF ABBREVIATIONS

AFM	Atomic force microscopy
AgX	Silver halide
Al_2O_3	Sapphire
ATR	Attenuated total reflection
AsSeTe	Chalcogenide
BSG	Borosilicate glass
CV	Cyclic voltammetry
EQCM	Electrochemical quartz crystal microbalance
ESTM	Electrochemical scanning tunneling microscope
FEL	Free electron laser
FEW	Fiber-optic evanescent wave
FPA	Focal plane array
FT-IR	Fourier transformed infrared
GaAs	Gallium arsenide
HWG	Hollow waveguide
IR	Infrared
IR-ATR	Infrared attenuated total reflectance spectroscopy
LDA	Linear discriminant analysis
LV	Latent variable
MCT	Mercury-cadmium-telluride
MIR	Mid-infrared

NIR	Near-infrared
NSOM	Near-field scanning optical microscopy
OAPM	Off-axis parabolic mirror
PBG	Photonic band gap
PC	Principle component
PCA	Principal component analysis
PCR	Principal component regression
PEM	Photoelectrochemical
Poly(SNS)	Polymer of 2,5-di-(2-thienyl)-pyrrol
PLS-DA	Partial least square-discriminant analysis
QCM	Quartz crystal microbalance
RMSECV	Root-mean square error of cross validation
SECM	Scanning electrochemical microscopy
SNS	Dithiophenylpyrrole, 2,5-di-(2-thienyl)-pyrrol
SPM	Scanning probe microscopy
SPR	Surface plasmon resonance
STM	Scanning tunneling microscope
TIR	Total internal reflection
UME	Ultramicroelectrode
ZnS	Zinc sulfide
ZnSe	Zinc selenide

SUMMARY

Mid-infrared (MIR) spectroscopy has been recognized as an important analytical technique, and is widely applied for qualitative and quantitative analysis of materials with an increasing interest in addressing complex organic or biologic constituents. In the presented thesis, (a) the fundamental principles for IR spectroscopic applications *via in vivo* catheters in combination with multivariate data analysis technique were developed, and (b) the combination with a second analytical technique – scanning electrochemical microscopy (SECM) - for enhancing the information obtained at complex or frequently changing matrices was demonstrated.

The first part of this thesis focused on the combination of different MIR measurement techniques with specific focus on evanescent field absorption spectroscopy along with multivariate data analysis methods, for the discrimination of atherosclerotic and normal rabbit aorta tissues. Atherosclerotic and normal rabbit aorta tissues are characterized by marked differences in chemical composition governed by their water, lipid, and protein content. Strongly overlapping infrared absorption features of the different constituents and the complexity of the tissue matrix render the direct evaluation of molecular spectroscopic characteristics obtained from IR measurements challenging for classification. We have successfully applied multivariate data analysis and classification techniques based on principal component analysis (PCA), partial least squares regression (PLS), and linear discriminant analysis (LDA) to IR spectroscopic data obtained by infrared attenuated total reflectance (IR-ATR) measurements, reflection IR microscopy,

and a recently developed IR-ATR catheter prototype for future *in vivo* diagnostic applications. Training and test data were collected *ex vivo* at atherosclerotic and normal rabbit aorta samples. The successful classification results at atherosclerotic and normal aorta samples utilizing the developed data evaluation routines reveals the potential of IR spectroscopy combined with multivariate classification strategies for *in vitro*, and – in future - *in vivo* applications.

The second part of this thesis aimed at the development of a novel multifunctional analytical platform by combining SECM with single-bounce IR-ATR spectroscopy for *in situ* studies of electrochemically active or electrochemically induced processes at the IR waveguide surface via simultaneous evanescent field absorption spectroscopy. The utility of the developed SECM-IR-ATR platform was demonstrated by spectroscopically monitoring microstructured polymer depositions induced *via* feedback mode SECM experiments using a 25µm Pt disk ultramicroelectrode (UME). The surface of a ZnSe ATR crystal was coated with a thin layer of 2,5-di-(2-thienyl)-pyrrole (SNS), which was then polymerized in a $Ru(bpy)_3^{2+}$-mediated feedback mode SECM experiment. The polymerization reaction was simultaneously spectroscopically monitored by recording the absorption intensity changes of specific IR bands characteristic for SNS, thereby providing information on the polymerization progress, mechanism, and level of surface modification.

Furthermore, a novel current-independent approach mechanism for positioning the UME in aqueous electrolyte solution was demonstrated by monitoring IR absorption changes of borosilicate glass (BSG) shielding the UME, and of water within the penetration depth of the evanescent field. The experimental results demonstrated that the UME penetrates into the exponentially decaying evanescent field extending several μm above the ATR crystal surface resulting in correlated intensity changes of the absorption spectra characteristic for borosilicate glass or water. Consequently, current-independent positioning of the UME close to the substrate surface and as required for SECM experiments is enabled with the developed SECM-IR-ATR platform.

CHAPTER 1

INTRODUCTION

Thesis Objectives:

The objectives of this thesis were the development and application of mid-infrared attenuated total reflection spectroscopy (IR-ATR) techniques for the *in situ* analysis of biological/biomedical samples, and their combination with scanning electrochemical microscopy (SECM) for simultaneously obtaining localized electrochemical and spectroscopic information.

Original Contributions of This Thesis:

- Hollow waveguide IR-ATR (HWG-IR-ATR) and reflection IR spectroscopy were combined with multivariate data analysis techniques for the classification of aorta tissue samples, and was successfully applied to the identification of lesion and normal rabbit aorta tissues. (Chapter 3)
- IR-ATR spectroscopy was combined with scanning electrochemical microscopy (SECM), and the analytical capabilities of this combination were demonstrated by simultaneous *in situ* optical monitoring of locally induced polymerization processes of dithiophenylpyrrole (SNS) by feedback mode SECM. (Chapter 4)
- IR-ATR spectroscopy was introduced as a novel mechanism for determining the distance between ultramicro electrodes and IR transparent substrates. (Chapter 5)

1.1 Chapter Overview

Chapter 2 of this thesis provides an overview on the background and theory of IR spectroscopy and IR-ATR sensing principles.

Chapter 3 focuses on IR-ATR applications for the identification of atherosclerotic and normal rabbit aorta tissue samples.

Chapter 4 describes the combination of SECM with IR-ATR spectroscopy, and demonstrates the analytical capabilities of this analytical platform by studying the dithiophenylpyrrole polymerization process as sample system.

Chapter 5 presents the concept of controlling the distance between UME and optically transparent substrates *via* IR-ATR; mathematical modeling of the obtained signals along with experiments spectroscopically monitoring the UME approach in air and liquid are provided.

Chapter 6 summarizes the contributions of the presented studies, and provides an outlook for the continuation of this work.

1.2 Biomedical Diagnosis by Optical Spectroscopy

Biological species usually comprise DNA/RNA, proteins, carbohydrates, lipids, and water as main molecular constituents, which can be characterized by distinct features in the optical spectral regime.[1-4] Some prominent IR vibrational bands frequently determined in biological samples are tentatively assigned and listed in **Table 1.1**.[1-3]

Table 1.1: Assignment of vibrational bands frequently determined in biological FT-IR spectra.[1-3]

Frequency regime (cm^{-1})	Assignment
~3800-3000	N-H str of proteins, O-H str of hydroxyl groups (eg. from water)
~3000-2900	C-H str (asym) of $-CH_2-$ and $-CH_3$ (eg. from lipids)
~2900-2800	C-H str (sym) of $-CH_2-$ and $-CH_3$ (eg. from lipids)
~1800-1680	>C=O str (eg. from DNA, carbonic acids and lipid esters)
~1700-1600	Amide I of proteins
~1600-1500	Amide II of proteins
~1350-1240	Amide III of proteins
~1250-1220	P=O str (asym) of $>PO_2^-$ phosphodiesters of DNA
~1200-900	C-O and C-C str; C-O-H and C-O-C deformation of carbohydrates
~1090-1085	P=O str (sym) of $>PO_2^-$ phosphodiesters of DNA
~720	C-H rocking of $>CH_2$

*str – stretching; asym – asymmetric; sym – symmetric.

The chemical composition and structure of cells, tissues, and the components of bio-fluids of biological entities are subject to variations at the molecular level, if affected by environmental factors, diseases, cancers, or other pathologies/abnormalities. Optical spectroscopy not only differentiates cells and tissues based on their characteristic spectral properties reflecting the chemical composition and structure, but has the potential to serve as a diagnostic tool for detecting and discriminating different diseases or disease progression due to the induced changes of chemical composition and structure in the biological matrix. Conventional biomedical diagnostics such as studies of cancerous cell or tissue are usually time consuming and labor intensive, and require expertise in sample preparation, as well as in cytology, histology, and pathology. In contrast to these traditional techniques, optical spectroscopy holds promise as a rapid, label-free analytical strategy, which is potentially labor- and time- saving, and requires a minimum amount of training, in particular if appropriate data processing and mining is an integral component of a diagnostic system. The most widely applied optical spectroscopy techniques in biomedical diagnosis are briefly described in the following text.

1.2.1 Fluorescence Spectroscopy

Fluorescence spectroscopy has been used to identify cells and tissues based on endogenous or exogenous chromophores, either *in vitro* or *in vivo*.[5-9] It is currently considered the most sensitive optical technique, with the potential for single-molecule detection. [10, 11] However, fluorescence techniques provide limited discriminatory information due to broad and frequently overlapping absorption and emission spectra obtained from tissue chromophores, and therefore usually require distinct labeling of the constituents of interest.[4]

1.2.2 Raman Spectroscopy

Raman spectroscopy is a viable alternative to IR spectroscopic techniques with substantial advantages for aqueous or hydrated biological samples. [12-16] While MIR absorption spectroscopy is strongly affected by the vibrational signature of water, aqueous matrices show negligible scattering effects, which is the fundamental mechanism giving rise to Raman signatures in the same spectral regime providing signatures complementary to IR data. However, Raman techniques are usually less sensitive, and significantly slower in collecting high-resolution data.[17]

1.2.3 Near-Infrared Spectroscopy

Near-infrared (NIR) spectroscopy is among the most common IR techniques currently applied in biomedical diagnostic studies.[18] NIR spectroscopy ideally complements mid-infrared [19] spectroscopy, as the absorption bands in the NIR regime ranging from approximately 13,000-4000 cm^{-1} result from overtones or combinations of the fundamental vibrational modes excited in the MIR spectral range with the results that NIR is usually much weaker and has unspecific features compared to mid-infrared spectroscopy. [20] Water is the major molecular component within biological matrices, and strongly affects the utility of selected electromagnetic spectral regimes due to strong O-H absorptions, especially in the MIR region. However, water has a relatively broad transmission window in the NIR, thereby enabling direct measurements of biological specimen. However, despite the merits of operating in the NIR regime, the information content and data interpretation of biological NIR spectra are frequently affected by relatively weak and highly convoluted absorption features.[20]

1.2.4 Mid-Infrared Spectroscopy

MIR spectroscopy is based on the absorption of radiation in the range of approximately 4000-400 cm^{-1}, and is currently considered among the most promising optical spectroscopic techniques for applications requiring direct molecular selectivity in biomedical diagnostics.[20] In contrast to NIR, fundamental vibrational transitions rather than overtones are addressed in the MIR, providing inherently higher signal intensities given the increased absorption cross-section. Furthermore, at wavelengths larger than 10 μm – also called the “fingerprint” regime - individual and combination vibrations of molecular species provide unique absorption patterns for each constituent, which enable direct constituent identification at a molecular level. A wide variety of MIR spectroscopy techniques have been applied to biomedical studies, including transmission[21-33] and reflection IR spectroscopy/microscopy,[34] IR-ATR techniques, [34-41] MIR mapping/imaging microscopy,[42, 43] and finally, fiber-optic evanescent wave (FEW) spectroscopic techniques utilizing IR-transparent fibers coupled to FT-IR spectrometers or lasers.[44-51] A potential disadvantage in the MIR regime results from rather pronounced water absorptions prevalent in the 3-20 μm spectral range. IR-ATR is a surface sensitive analytical technique detecting molecular species via absorption spectroscopy within an exponentially decaying evanescent field generated at the surface of an appropriate total internal reflection (TIR) element.[52] Hence, only molecules present within the analytical volume probed in vicinity of the TIR element surface are detected. The volume is determined by penetration depths of evanescent field extending up to a few micrometers into the contacted sample surface or adjacent medium at MIR wavelengths. Of all MIR techniques, IR-ATR is the most promising strategy to mitigate water matrix effects without requiring sample dehydration, water signal subtraction, or the preparation of thin sample slices for hydrated specimens. While this technology is certainly also useful in the NIR regime, penetration depths at 1.5 μm and below in the NIR significantly reduce the analytically probed volume at the waveguide surface. The relative similarity of the refractive index of commonly used NIR waveguide materials, such as e.g., silica, vs. the adjacent aqueous sample matrix also contribute to this effect. Thus, ATR techniques in the MIR appear particularly promising for studying biological samples with a minimum, or ideally without any sample pretreatment.

With the development of more advanced optical fibers and waveguide technologies for radiation delivery and as active sensor heads in the MIR region,[53, 54] The combination of IR-ATR with MIR waveguides has the potential to be applicable for *in vivo* diagnostics, providing spectroscopic guidance during e.g., laser surgery.

1.3 References

(1) Jackson, M.; Mantsch, H. H. *Infrared Spectroscopy of Biological Molecles*; Wiley-Liss: New York, 1996.

(2) Naumann, D. *FT-infrared and FT-Raman spectroscopy in biomedical research*, Appl. Spectrosc. Rev. **2001**, *36*, 239-298.

(3) Petrich, W. *Mid-infrared and raman spectroscopy for medical diagnostics*, Appl. Spectrosc. Rev. **2001**, *36*, 181-237.

(4) Morris, M. D. *Biomedical Photonics Handbook Edited by Tuan Vo-Dinh*, 2004.

(5) Bindig, U.; Rohde, E.; Mueller, G. *Advances of optical sensors in biomedicine*, Opt. Appl. **2003**, *32*, 545-568.

(6) Bottiroli, G.; Croce Anna, C. *Autofluorescence spectroscopy of cells and tissues as a tool for biomedical diagnosis*, Photochem. Photobiol. Sci. **2004**, *3*, 189-210.

(7) Richards-Kortum, R.; Sevick-Muraca, E. *Quantitative optical spectroscopy for tissue diagnosis*, Annu. Rev. Phys. Chem. **1996**, *47*, 555-606.

(8) Schneckenburger, H.; Sailer, R.; Stock, K.; Strauss, W. S. L.; Steiner, R. W. *Fluorescence techniques in biomedical diagnostics*, Proc. SPIE-Int. Soc. Opt. Eng. **2003**, *5068*, 122-133.

(9) Vo-Dinh, T.; Cullum, B. M. *Fluorescence spectroscopy for biomedical diagnostics*, Biomed. Photonics Handb. **2003**, 28/21-28/50.

(10) Hesse, J.; Sonnleitner, M.; Schutz Gerhard, J. *Ultra-sensitive fluorescence reader for bioanalysis*, Curr Pharm Biotechnol **2004**, *5*, 309-319.

(11) Kelso, D. M. *Biomedical applications of single molecule detection*, Proc. SPIE-Int. Soc. Opt. Eng. **1997**, *2985*, 206-212.

(12) Moreira, L. M.; Silveira, L., Jr.; Santos, F. V.; Lyon, J. P.; Rocha, R.; Zangaro, R. A.; Villaverde, A. B.; Pacheco, M. T. T. *Raman spectroscopy: A powerful technique for biochemical analysis and diagnosis*, Spectroscopy **2008**, *22*, 1-19.

(13) Lin, S.-Y.; Li, M.-J.; Cheng, W.-T. *FT-IR and Raman vibrational microspectroscopies used for spectral biodiagnosis of human tissues*, Spectroscopy **2007**, *21*, 1-30.

(14) Krafft, C.; Sergo, V. *Biomedical applications of Raman and infrared spectroscopy to diagnose tissues*, Spectroscopy **2006**, *20*, 195-218.

(15) Ellis, D. I.; Goodacre, R. *Metabolic fingerprinting in disease diagnosis: biomedical applications of infrared and Raman spectroscopy*, Analyst **2006**, *131*, 875-885.

(16) Ozaki, Y. *Medical application of Raman spectroscopy*, Appl. Spectrosc. Rev. **1988**, *24*, 259-312.

(17) Ferraro, J. R.; Nakamoto, K.; Brown, C. W. *Introductory Raman Spectroscopy, Second Edition*, 2003.

(18) Rempel, S. P.; Mantsch, H. H. *Biomedical applications of near-infrared spectroscopy: A review*, Can. J. Anal. Sci. Spectrosc. **1999**, *44*, 171-179.

(19) Marcu, L.; Fang, Q.; Jo, J. A.; Papaioannou, T.; Dorafshar, A.; Reil, T.; Qiao, J.-H.; Baker, J. D.; Freischlag, J. A.; Fishbein, M. C. *In vivo detection of macrophages in a rabbit atherosclerotic model by time-resolved laser-induced fluorescence spectroscopy*, Atherosclerosis **2005**, *181*, 295-303.

(20) Stuart, B. H. *Infrared Spectroscopy-Fundamentals and Applications. (Analytical Techniques in the Sciences (AnTs))*, 2004.

(21) Arai, T.; Mlzuno, K.; Fujikawa, A.; Makagawa, M.; Kikuchl, M. *Infrared absorption spectra ranging from 2.5 to 10 µm at various layers of human normal abdominal aorta and Fibrofatty atheroma in vitro*, Lasers Surg. Med. **1990**, *10*, 3561.

(22) Lasch, P.; Naumann, D. *Ft-IR microspectroscopic imaging of human carcinoma thin sections based on pattern recognition techniques*, Cell. Mol. Biol. **1998**, *44*, 189-202.

(23) Liu, K. Z.; Schultz, C. P.; Johnston, J. B.; Beck, F. W. J.; Al-Katib, A. M.; Mohammad, R. M.; Mantsch, H. H. *Infrared spectroscopic study of bryostatin 1-induced membrane alterations in a B-CLL cell line*, Leukemia **1999**, *13*, 1273-1280.

(24) Martin, T. C.; Moecks, J.; Belooussov, A.; Cawthraw, S.; Dolenko, B.; Eiden, M.; von Frese, J.; Koehler, W.; Schmitt, J.; Somorjai, R.; Udelhoven, T.; Verzakov, S.; Petrich, W. *Classification of signatures of Bovine Spongiform Encephalopathy in serum using infrared spectroscopy*, Analyst **2004**, *129*, 897-901.

(25) Sahu, R. K.; Zelig, U.; JUleihel, M.; Brosh, N.; Talyshinsky, M.; Ben-Harosh, M.; Mordenchai, S.; Kapelushnik, J. *Continuos monitoring of WBC (biochemistry) in an adult leukemia patient using advanced FTIR-spectroscopy*, Leuk Res **2006**, *30*, 687-693.

(26) Vonach, R.; Buschmann, J.; Falkowski, R.; Schindler, R.; Lendl, B.; Kellner, R. *Application of mid-infrared transmission spectrometry to the direct determination of glucose in whole blood*, Appl. Spectrosc. **1998**, *52*, 820-822.

(27) Chiriboga, L.; Xie, P.; Vigorita, V.; Zarou, D.; Zakim, D.; Diem, M. *Infrared spectroscopy of human tissue. II. A comparative study of spectra of biopsies of cervical squamous epithelium and of exfoliated cervical cells*, Biospectroscopy **1998**, *4*, 55-59.

(28) Chiriboga, L.; Xie, P.; Yee, H.; Vigorita, V.; Zarou, D.; Zakim, D.; Diem, M. *Infrared spectroscopy of human tissue. I. Differentiation and maturation of epithelial cells in the human cervix*, Biospectroscopy **1998**, *4*, 47-53.

(29) Diem, M.; Boydston-White, S.; Pacifico, A.; Chiriboga, L. *Distinction between normal and neoplastic human cells and tissues by infrared microspectroscopy*, Spectrosc. Biol. Mol.: New Dir., Eur. Conf., 8th, Enschede, Netherlands, Aug. 29-Sept. 2, 1999 **1999**, 479-482.

(30) Eysel, H. H.; Jackson, M.; Nikulin, A.; Somorjai, R. L.; Thomson, G. T. D.; Mantsch, H. H. *A novel diagnostic test for arthritis: multivariate analysis of infrared spectra of synovial fluid*, Biospectroscopy **1997**, *3*, 161-167.

(31) Manoharan, R.; Baraga, J. J.; Rava, R. P.; Dasari Ramachandra, R.; Fitzmaurice, M.; Feld Michael, S. *Biochemical analysis and mapping of atherosclerotic human artery using FT-IR microspectroscopy*, Atherosclerosis **1993**, *103*, 181-193.

(32) Sahu, R. K.; Moderdechai, M. *Infrared trasform infrared spectroscopy in cancer detection*, Future Oncol. **2005**, *1*, 635-647.

(33) Shaw, R. A.; Eysel, H. H.; Liu, K. Z.; Mantsch, H. H. *Infrared spectroscopic analysis of biomedical specimens using glass substrates*, Anal. Biochem. **1998**, *259*, 181-186.

(34) Wang, J.; Sowa, M.; Mantsch, H. H.; Bittner, A.; Heise, H. M. *Comparison of different infrared measurement techniques in the clinical analysis of biofluids*, TrAC, Trends Anal. Chem. **1996**, *15*, 286-296.

(35) Baraga, J. J.; Feld Michael, S.; Rava, R. P. *Detection of atherosclerosis in human artery by mid-infrared attenuated total reflectance*, Appl. Opt. **1991**, *45*, 709-711.

(36) Fabian, H.; Lasch, P.; Naumann, D. *Analysis of biofluids in aqueous environment based on mid-infrared spectroscopy*, J. Biomed. Opt. **2005**, *10*, 031103/031101-031103/031110.

(37) Heise, H. M.; Marbach, R.; Janatsch, G.; Kruse-Jarres, J. D. *Multivariate determination of glucose in whole blood by attenuated total reflection infrared spectroscopy*, Anal. Chem. **1989**, *61*, 2009-2015.

(38) Heise, H. M.; Voigt, G.; Lampen, P.; Kupper, L.; Rudloff, S.; Werner, G. *Multivariate calibration for the determination of analytes in urine using mid-infrared attenuated total reflection spectroscopy*, Appl. Spectrosc. **2001**, *55*, 434-443.

(39) Janatsch, G.; Kruse-Jarres, J. D.; Marbach, R.; Heise, H. M. *Multivariate calibration for assays in clinical chemistry using attenuated total reflection infrared spectra of human blood plasma*, Anal. Chem. **1989**, *61*, 2016-2023.

(40) Mordechai, S.; Sahu, R. K.; Hammody, Z.; Mark, S.; Kantarovich, K.; Guterman, H.; Podshyvalov, A.; Goldstein, J.; Argov, S. *Possible common biomarkers from FTIR microspectroscopy of cervical cancer and melanoma*, J. Microsc. **2004**, *215*, 86-91.

(41) Sahu, R. K.; Argov, S.; Salman, A.; Huleihel, M.; Grossman, N.; Hammody, Z.; Kapelushnik, J.; Mordechai, S. *Characteristic absorbance of nucleic acids in the mid-IR region as possible common biomarkers for diagnosis of malignancy*, Technol. Cancer Res. Treat. **2003**, *3*, 629-638.

(42) Colley, C. S.; Kazarian, S. G.; Weinberg, P. D.; Lever, M. J. *Spectroscopic imaging of arteries and atherosclerotic plaques*, Biopolymers **2004**, *74*, 328-335.

(43) Kazarian, S. G.; Chan, K. L. A. *Applications of ATR-FTIR spectroscopic imaging to biomedical samples*, Biochim. Biophys. Acta **2006**, *1758*, 858-867.

(44) Afanasyeva, N. I.; Bruch, R. F.; Katzir, A. *Infrared fiber optic evanescent wave spectroscopy: applications in biology and medicine*, Proc. SPIE-Int. Soc. Opt. Eng. **1999**, *3596*, 152-164.

(45) Bindig, U.; Gersonde, I.; Meinke, M.; Becker, Y.; Mueller, G. *Fibre-optic IR-spectroscopy for biomedical diagnostics*, Spectroscopy **2003**, *17*, 323-344.

(46) Eytan, O.; Sela, B.-A.; Katzir, A. *Fiber-optic evanescent-wave spectroscopy and neural networks: Application to chemical blood analysis*, Appl. Opt. **2000**, *39*, 3357-3360.

(47) Gotshal, Y.; Adam, I.; Katzir, A. *Glucose measurements in solutions using fiberoptic evanescent wave spectroscopy and tunable CO2 laser*, Proc. SPIE-Int. Soc. Opt. Eng. **1998**, *3262*, 192-196.

(48) Heise, H. M.; Bittner, A.; Kupper, L.; Butvina, L. N. *Comparison of evanescent wave spectroscopy based on silver halide fibers with conventional ATR-IR spectroscopy*, J. Mol. Struct. **1997**, *410-411*, 521-525.

(49) Heise, H. M.; Kupper, L.; Butvina, L. N. *Attenuated total reflection mid-infrared spectroscopy for clinical chemistry applications using silver halide fibers*, Sens. Actuators **1998**, *B51*, 84-91.

(50) Heise, H. M.; Kupper, L.; Butvina, L. N. *Bio-analytical applications of mid-infrared spectroscopy using silver halide fiber-optic probes*, Spectrochim. Acta **2002**, *57B*, 1649-1663.

(51) Lambrecht, A.; Beyer, T.; Hebestreit, K.; Mischler, R.; Petrich, W. *Continuous glucose monitoring by means of fiber-based, mid-infrared laser spectroscopy*, Appl. Spectrosc. **2006**, *60*, 729-736.

(52) Harrick, N. J. *Internal reflection spectroscopy*; Interscience Publishers: New York, 1967.

(53) Charlton, C.; Giovannini, M.; Faist, J.; Mizaikoff, B. *Fabrication and characterization of molecular beam epitaxy grown thin-film GaAs waveguides for mid-infrared evanescent field chemical sensing*, Anal. Chem. **2006**, *78*, 4224-4227.

(54) Charlton, C.; Temelkuran, B.; Dellemann, G.; Mizaikoff, B. *Midinfrared sensors meet nanotechnology: Trace gas sensing with quantum cascade lasers inside photonic band-gap hollow waveguides*, Appl. Phys. Lett. **2005**, *86*, 194102/194101-194102/194103.

CHAPTER 2

BACKGROUND

In this Chapter, the fundamental principles of mid-infrared spectroscopy and attenuated total reflection infrared (IR-ATR) spectroscopy are introduced.

2.1 Fundamentals of Mid-Infrared Spectroscopy

Optical spectroscopy utilizes the interaction of electromagnetic radiation with matter. The MIR spectral range covers the electromagnetic frequency regime from approx. 4000 - 400 cm^{-1}, which enables excitation of vibrational or vibrational-rotational transitions of molecules involving transitions from/to rotational and/or vibrational levels in the same ground electronic state. [1-4] MIR spectra are frequently characteristic of various functional groups within a molecule, particularly in the so-called "fingerprint" regime (approx. 1200 - 400 cm^{-1}), the vibrations of the related specific bonds show absorption patterns that are highly substance specific. Consequently, MIR spectra can be used to determine the chemical nature and molecular structure of a constituent. Since its introduction, MIR spectroscopy has increasingly been recognized as an important analytical technique, and has been applied widely in qualitative and quantitative analysis of materials including organic, inorganic, and biological substances.

Commonly, IR spectra are measured in transmission-absorption mode with gas, liquid, or solid phase samples. During the measurement, radiation propagates directly through the sample and is absorbed at frequencies where resonant energy transfer occurs. The wavelength-dependant light reduction is calculated and defined as transmittance (T):

$$T = \frac{I}{I_0}$$

(Eq. 2. 1)

where I_0 is the intensity of incident radiation, and I is the intensity of radiation after passing through the sample. For quantitative applications of IR spectroscopy, Eq. 2.1 is usually rearranged and expressed as absorbance (A):

$$A = -\log(T) = -\log\left(\frac{I}{I_0}\right)$$

(Eq. 2. 2)

For quantitative measurements, absorbance may also be defined by the Lambert-Beer law:

$$A = \varepsilon Cl$$

(Eq. 2. 3)

where ε is the absorptivity, C is the concentration, l is the thickness of sample (optical path length of light through the sample). Therefore, equation 2.3 shows a linear dependence of absorbance on the thickness of the sample, or more generally, the absorption path length.

2.2 Fundamentals of Attenuated Total Reflection Spectroscopy

2.2.1 Principles of Attenuated Total Reflection Spectroscopy

Attenuated total reflection (ATR) spectroscopy derives from internal reflection spectroscopy, and was independently pioneered by Fahrenfort[5] and Harrick[6] in the early 1960's. When radiation propagates from an optically denser medium (refractive index n_1) toward an optically rarer medium (refractive index n_2, $n_1 > n_2$), total internal reflection will occur at the interface of the two media, if the radiation angle of incidence (θ) is exceeding the critical angle (θ_c). The critical angle can be defined as a function of the refractive indices of two media:

$$\theta_c = \sin^{-1}\left(\frac{n_2}{n_1}\right)$$

Eq. 2. 4

At each reflection, an evanescent field is extending into the adjacent optically rarer medium. This evanescent field may be described as a standing electric wave normal to the interface of the two media, and results from the superposition of the electric fields of the incident and reflected waves. The amplitude of this standing electric wave (E) exponentially decays with distance from the interface following[6]:

$$E = E_0 e^{-\left(\frac{z}{d_p}\right)}$$

Eq. 2. 5

where E_0 is the amplitude of the electric field at the interface ($z = 0$), z is the distance from the interface, and d_p is the penetration depth. The penetration depth (d_p) is defined as the distance where the amplitude of the electric field is $1/e$ of E_0, which is a function of refractive indices n_1 and n_2, the incidence angle θ, and the wavelength of the radiation λ[6]:

$$d_p = \frac{\lambda}{2\pi\sqrt{n_1^2 \sin^2\theta - n_2^2}}$$

Eq. 2. 6

The principle of TIR is schematically shown in **Figure 2. 1**.

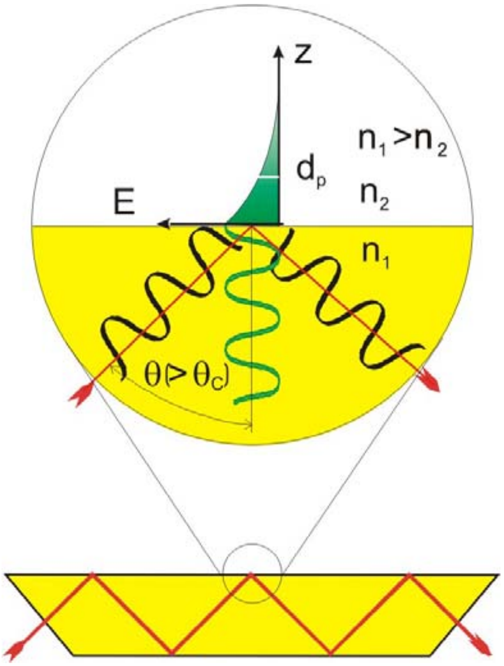

Figure 2. 1: Schematic representation of the TIR principle.

If the optically rarer medium – or constituents therein - is absorbing IR radiation, attenuated total reflection (ATR) is resulting at characteristic wavelengths corresponding to the vibrational resonant frequency. One of the main advantages of ATR spectroscopy is the fact that absorption spectra can be obtained at highly absorptive and/or scattering samples, such as turbid liquids or powder samples, given the minimal penetration into an otherwise opaque medium.

2.2.2 IR-ATR Waveguides

The availability of different IR-ATR waveguide materials and geometries contributes to the development of a variety of IR-ATR sensing schemes. IR-ATR waveguides commonly include IR transparent optical fibers and ATR crystals. The former are typically made from materials including but not limited to silver halides (AgX), sapphire (Al_2O_3), and chalcogenides (AsSeTe glasses)[7, 8]; the latter are typically made from zinc selenide (ZnSe), zinc sulfide (ZnS), Germanium (Ge), and silicon (Si)[9-12]. The physical properties and wavelength dependant transmittance of optical waveguides determines or limits their applicability for certain samples. The geometry and the dimensions (e.g., thickness, length, etc.) of optical waveguides can be adjusted to fulfill individual measurement requirements. In this thesis, prisms and hemispheres made from ZnSe were utilized for the development of different IR-ATR sensing instruments for a variety of applications.

2.3 References

(1) Avram, M.; Mateescu, G. D. *Infrared Spectroscopy: Applications in Organic Chemistry*, 1972.

(2) Christy, A. A.; Ozaki, Y.; Gregoriou, V. G. *Modern Fourier Transform Infrared Spectroscopy*, 2001.

(3) Stuart, B. H. *Infrared Spectroscopy-Fundamentals and Applications. (Analytical Techniques in the Sciences (AnTs))*, 2004.

(4) Theophanides, T. *Fourier Transform Infrared Spectroscopy: Industrial Chemical and Biochemical Applications*, 1984.

(5) Fahrenfort, J. *Attenuated total reflection. A new principle for the production of useful infrared reflection spectra of organic compounds*, Spectrochim. Acta **1961**, *17*, 698-709.

(6) Harrick, N. J. *Internal reflection spectroscopy*; Interscience Publishers: New York, 1967.

(7) Holst, G.; Mizaikoff, B. *Fiber optic sensors for environmental applications*, Handb. Opt. Fibre Sens. Technol. **2002**, 729-755.

(8) Mizaikoff, B. *Mid-IR fiber-optic sensors*, Anal. Chem. **2003**, *75*, 258A-267A.

(9) Specac Inc., http://www.specac.com/.

(10) MacroOptica Ltd, http://www.macrooptica.com/.

(11) PIKE Technologies, http://www.piketech.com/.

(12) Harrick Scientific Products, Http://www.harricksci.com/.

CHAPTER 3

IDENTIFICATION OF ATHEROSCLEROTIC AND NORMAL RABBIT AORTA TISSUES USING IR SPECTROSCOPY

In this chapter, a custom-built IR-ATR catheter prototype, commercially available reflectance microspectroscopy and IR-ATR spectroscopy were combined with multivariate data analysis techniques for the *in situ* identification of atherosclerotic and normal rabbit aorta tissues. Also presented is a background on artery atherosclerosis and specific multivariate data analysis techniques utilized in this thesis, such as principal component analysis (PCA), principle component regression (PCR), partial least square-discriminant analysis (PLS-DA), and Mahalanobis distance.

3.1 Motivation

Hooper et al. have demonstrated an IR-ATR catheter system coupled with a free electron laser (FEL) emitting in the MIR range that enables *in vitro* ablation of atherosclerotic lesion plaques in their natural state, facilitating a controlled ablation depth by evenascent field penetration. This technique has the potential to deliver MIR laser radiation into the body for minimally invasive surgical procedures (**Figure 3.1**).[1, 2] In order to ablate the lesion spot properly, lesion spot detection technique(s) are necessary to guide positioning of such IR-ATR catheters. The main components of this system are hollow glass waveguides (HWGs) and an ATR crystal tip, which are capable, respectively, of delivering and guiding FEL and IR radiation. By using the evanescent wave for ablation, the potential for damage to underlying or adjacent tissue is significantly reduced, if not eliminated. In addition, IR-ATR is particularly appropriate for the analysis of biological samples, as previously shown.[3-23] Hence, in principle laser coupled IR-ATR techniques have the potential to simultaneously ablate lesion spots that were *in situ* chemically identified by MIR spectroscopy/sensing during the same procedure. However, strongly overlapping infrared absorption features of different constituents, and the complexity of the tissue matrix usually render the direct evaluation of molecular spectroscopic characteristics obtained from such optical measurements challenging during tissue identification. Sophisticated multivariate data analysis technique have the power to deconvolute such complex signatures, and enable extracting the information of interest from highly convoluted spectra.[3] The aim of the studies presented herein was to reveal the potential of IR spectroscopy combined with multivariate classification strategies for *in situ* identification of atherosclerotic and normal aorta tissues during *in vitro*, and – in future - *in vivo* applications.[24, 25]

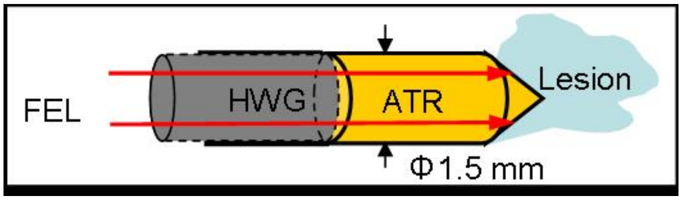

Figure 3.1: Scheme of an IR-ATR catheter for atherosclerotic lesion ablation. FEL – free electron laser; HWG – hollow glass waveguide.

3.2 Introduction

Histochemical analysis is the classical method to study atherosclerotic lesions, and their pathophysiological progression. However, this method usually requires trained personnel for the sample preparation, which includes slicing from artery wall tissue, and staining for optical microscopy, thereby rendering this procedure complex, time-consuming, and limited to *in vitro* conditions.

In biomedical diagnostics, optical spectroscopy is a powerful characterization tool sensitive to the variation of the molecular composition of the matrix, and has been applied for rapid classification of cell and tissue samples.[26-37] Recent studies have shown that the vulnerability of the atherosclerotic plaque is largely dependant on its chemical composition and ultrastructure.[38] Different spectroscopic techniques, including fluorescence spectroscopy, Raman specrtroscopy, and near-infrared (NIR) spectroscopy have been used for characterizing normal tissues and plaques in human artery samples. Fluorescence spectroscopy has been used to study normal and atherosclerotic tissues based on endogenous or exogenous tissue chromophores[39-52], thereby successfully classifying normal and plaque artery tissues *in vitro*. In a more recent study, Marcu's group demonstrated a catheter based time-resolved fluorescence spectroscopy technique that can differentiate and demark macrophage content versus collagen content in a rabbit atherosclerotic model *in vivo*[53]. Lucas group also developed a catheter-based fluorescence emission analysis technique and detected Russell's viper venom induced atherosclerotic plaque disruption in rabbit models both *in vitro* and *in vivo*[54]. The same fluorescence technique was also utilized by Lucas group for the analysis of quantitative changes in collagen and elastin during arterial remodeling in rabbit *in vivo* models[55]. However, fluorescence techniques provide limited discriminatory information due to broad and frequently overlapping absorption and emission spectra obtained from tissue chromophores. NIR FT-Raman has extensively been applied for qualitative and quantitative studies on the chemical composition of atherosclerotic plaques, and appears to be among the most promising techniques at present for the identification of vulnerable plaques[38, 56-65]. Until recently, *in vivo* Raman spectroscopy techniques have greatly improved for successful intravascular detection. The group of van der Laarse has employed commercially available fiber-optic probes (Visionex), and has obtained high quality *in vivo* Raman spectra for the characterization of artery walls in lamb and sheep.[59] Further progress on *in vivo* detection was achieved by the Feld group, which has developed an optical fiber probe based Raman system.[66] They demonstrated the first real-time collection of Raman spectra of human atherosclerosis *in vivo*. In addition, a variety of IR spectroscopic techniques including diffuse reflectance NIR spectroscopy[67-69], conventional transmission Fourier transform infrared (FT-IR) spectroscopy[70], IR-ATR spectroscopy[5], and FT-IR microscopy[23] have been used for characterizing and identifying atherosclerotic plaques. Different spectroscopic mapping/imaging techniques including fluorescence[71], Raman[72], reflectance NIR[73], transmission FT-IR microscopy[74], and IR-ATR[22] have also been used to characterize atherosclerotic plaques. Among the imaging techniques, micro-ATR FT-IR imaging[22] demonstrated by Colley *et al*. has the merits of enhanced sensitivity, and much faster acquisition times compared to Raman imaging, and much higher resolution compared to other FT-IR imaging techniques. In Colley's study, the cross sections of atherosclerotic rabbit arteries were analyzed with a spatial resolution of 3-4 μm at the cellular level. Furthermore, the distribution heterogeneity of cholesterol esters in plaque was revealed during these studies. Higher concentrations of cholesterol and its ester in atherosclerotic plaque in contrast to normal artery tissue[50] have also been confirmed by the IR techniques mentioned above. Among these techniques, ATR methods are of particular interest due to their lack of dependence on the sample thickness, which renders them ideal for thick, strongly absorbing, or possibly opaque materials such as tissue. In addition, ATR techniques are suitable for miniaturization, providing the potential to obtain spectroscopic signals and diagnostic information *in vivo*, if coupled with appropriate fiber optic signal delivery systems.

All data presented in this study were obtained from intact aorta samples, and all spectra were generated from the inner surface of the intima. Atherosclerotic and normal rabbit aorta samples show a significant difference in chemical composition governed by the water, lipid, and protein content.[75] However, initial IR studies by our group at rabbit aorta samples, especially hydrated samples, revealed that the difference between plaque and normal aorta tissue is very subtle due to the averaging of the spectra across the measured areas. Therefore, tissue classification by direct evaluation of the spectroscopic differences is virtually impossible. Principle components analysis (PCA) was combined with Raman spectroscopy in a study by Deinum *et al.* to identify three classes of human coronary artery.[61] Discriminant analysis using Mahalanobis distance was applied on PCA scores extracted from Raman spectra of human artery tissue, and were classified into three categories. Dao *et al.* and Weinmann *et al.* coupled partial least square (PLS) regression algorithms with Raman spectroscopy for quantifying the cholesterol and cholesterol ester concentration in human and rabbit aorta tissue[60, 65], which was suitable for identifying lipid-rich plaques prone to disruption. In the present study, instead of evaluating a few individual spectroscopic features for the identification of rabbit aorta samples, multivariate data analysis strategies were adopted. In particular, we have applied PCA/PCR, partial least squares discriminant analysis (PLS-DA) and linear discriminant analysis (LDA) along with Mahalanobis distance calculations to IR data obtained *via* an IR-ATR catheter prototype and IR reflection spectroscopy. In the presented work, we show that IR-ATR spectroscopy combined with multivariate classification techniques has the potential for *in situ* identification of atherosclerotic and normal aorta tissue, which provides a sound basis for the development of *in vivo* IR diagnostic devices integrated into a catheter format.

3.3 Background

3.3.1 Mechanisms of Atherosclerosis

Atherosclerosis is a disease condition of arteries where the fatty materials and plaque are deposited at the inner wall of the blood vessel resulting in the narrowing of the arterial lumen, and eventual blocking of the blood flow.[75] The top graph in **Figure 3.2** shows a schematic view of an artery wall section, which consists of three layers: inner layer – intima (endothelium), middle layer - media (muscle cells and elastic fiber), and outer layer - adventitia (connective tissue, collagen, and elastic fiber). The inner wall of normal arteries has a smooth texture. During atherosclerotic plaque development, the artery thickens and becomes less elastic. At the bottom of **Figure 3.2**, graphs (a – d) schematically describe atherosclerotic plaque development. At the very early stage (a), the monocytes move into the intima through injury to the inner lining. Inside the artery wall, they are transformed into foam cells, which are cholesterol/cholesterol ester-rich. Once the foam cells die, they release fatty materials forming extracellular lipid (b). At more advanced development stages, smooth muscle cells move from the media layer into the intima (c). Usually, only some of the plaques rupture and produce damage to individuals.

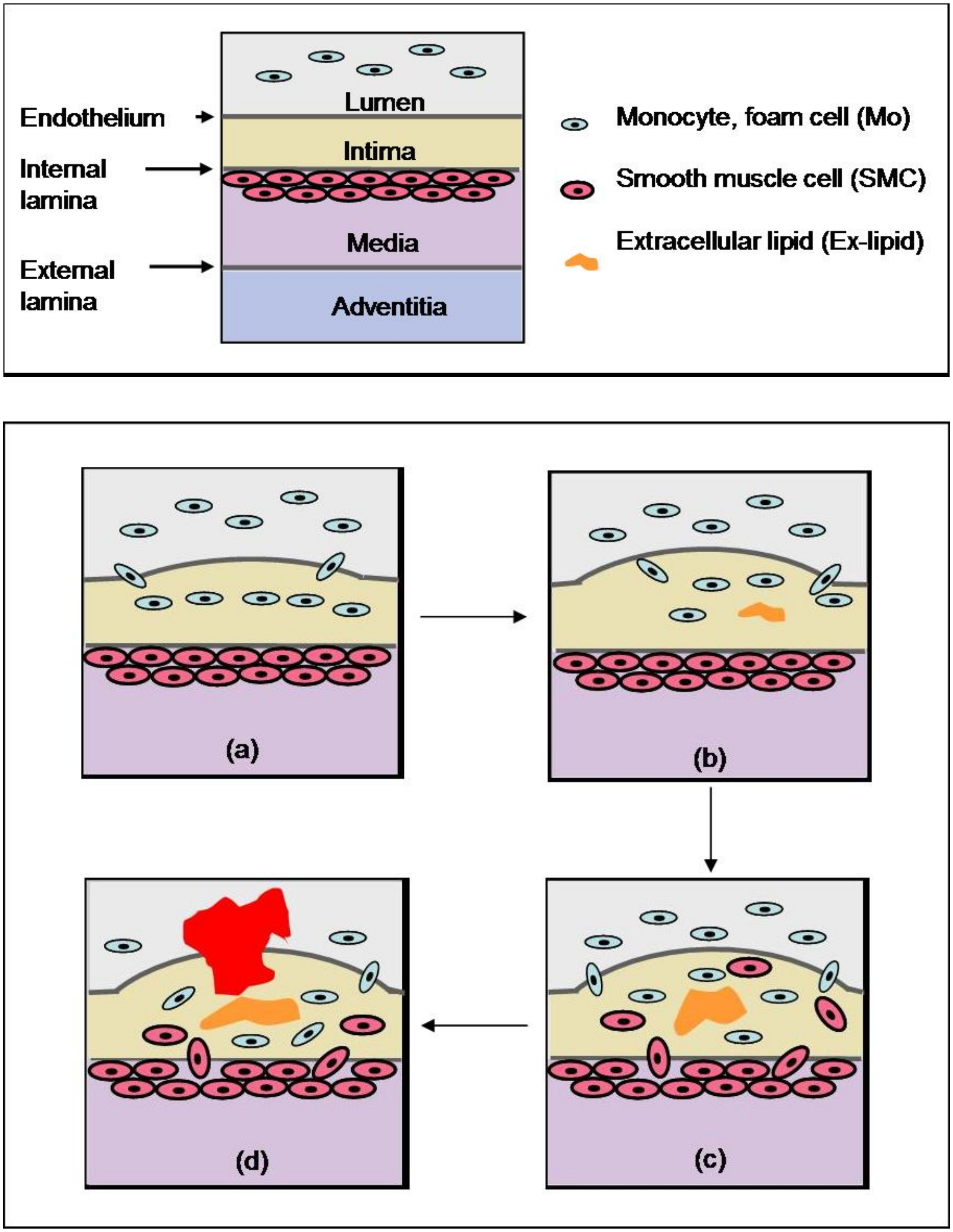

Figure 3.2: (top) – Schematic of the artery structure; (bottom) – Atherosclerotic plaque development process: (a) monocyte enters intima and artery starts thickening; (b) extracellular lipid forms; (c) muscle cell enters intima; (d) thrombus forms.

After rupture, platelets adhere to the lipid pool in the plaque, and cause the formation of a thrombus. Some of the thrombi may become free-travelers flowing with the blood stream, and lodge in the thin arteries resulting in a sudden and complete blockage of the blood flow in these vessels.

Some plaques could grow thick enough to block the lumen. In addition, the free thrombi have the fatal risk of sudden death. It is important to detect and remove the plaques at early stages to prevent the blood flow block or sudden death.

3.3.2 Multivariate Data Analysis

Multivariate data analysis (a.k.a., chemometrics) utilizes mathematical, statistical, and computer sciences to efficiently extract useful information from data generated *via* chemical measurements. Multivariate data analysis can be roughly divided into *multivariate classification* (pattern recognition) and *multivariate regression* techniques.[76-79]

The pattern recognition techniques can be further divided into two categories: *supervised* and *unsupervised* learning procedures. For both, a sufficiently large training set of well-defined samples is required to build a robust model. In unsupervised pattern recognition, no *a priori* knowledge about the training set samples class membership is required. Hence, samples will be grouped into a number of classes with certain communalities without initial qualification of the samples or their class assignment. Thereby, even without initial knowledge on the expected differences, structure within certain data sets may be recognized. On the contrary, supervised pattern recognition requires *a priori* knowledge of the classes contained within the training samples, i.e., which sample belongs to which class such as (e.g., clearly identifying samples from disease cases vs. samples from healthy cases). Consequently, unsupervised pattern recognition techniques are exploratory methods for data analysis, which seek inherent similarities of data, and group data in a 'natural' way. Using this data analysis technique, unexpected grouping within a training sample set may be discovered that may not be initially evident, e.g., that a group of disease-related samples might additionally separate into two or more distinctly different classes. Supervised pattern recognition techniques are different, as they group data into predefined classes already identified during the training procedures, thereby allowing a more precise classification within the class boundaries. Clearly, each approach has strength and weaknesses, and its appropriate applications.

Multivariate regression is frequently applied to analyze one or multiple constituents in a complex sample that are subject to significantly overlapping analytical signals. A training data set with known concentrations of interest is used to build a calibration model; consequently, the concentration levels in unknown samples are predicted based on the established model. In general, sufficient accuracy and robustness of classification and predictive regression models have to be evaluated with an appropriate set of validation samples prior to the analysis of unknowns. In the following, several pattern recognition methodologies and one regression method utilized in this work are briefly introduced.

3.3.2.1 Principal Component Analysis (PCA)

PCA is a commonly applied unsupervised pattern recognition technique based on evaluating the total variances within a data set *via* eigenanalysis, which provides two distinct benefits. First, it is a powerful data reduction technique that can condense the original data with a large number of initial variables to a dataset with only a few variables reflecting the most relevant analytical information. Simply summarizing, by transforming the coordinate system of the (multi-dimensional) data set generated by the analytical measurement (e.g., MIR spectra) into a coordinate system representing the orthogonal directions of largest variances within the data set, the usually rather large number of variables contributing to the total variance is reduced to a much smaller set of so called *principal components* (PCs). This operation is graphically demonstrated in **Figure 3.3**. This - and similar - data reduction processes are the fundamental basis of many multivariate data analysis techniques, with the main advantage that classification and regression of unknowns in this transformed coordinate system is processed much faster given much fewer relevant variables. Secondly, PCA assists in resolving overlapping spectral features, as rather than selecting an individual wavelength for constituent-specific evaluation, variance across the entire spectral range or within selected frequency regimes is taken into account. The unique scores derived for each data set can be used to group/classify data in the PC-based coordinate system, or to regress to concentration information. However, PCA is only capable of recognizing total variance regarding a whole data set, and not capable of identifying within-group and among-group variances.

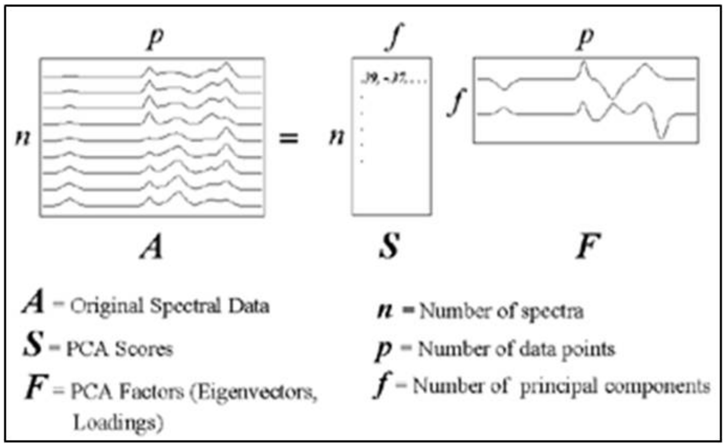

Figure 3.3: Demonstration of PCA compression.

3.3.2.2 Principal Component Regression (PCR)

During PCR, PCA is used to compress and decompose the original spectra generated from training samples into fewer variables (PCs), capturing the relevant variances within the data set, and then using the scores derived from the training data to create a quantitative model. During the prediction of unknowns, the score vectors of the unknowns are derived based on their unique spectra, and regressed against the PC vectors obtained from the calibration samples for retrieving a quantitative prediction of the unknown concentration. PCR was also successfully implemented as a classification tool by Haaland *et al.*, and was applied to classify cell and tissue samples.[80]

3.3.2.3 Partial least squares – Discriminant Analysis (PLS-DA)

PLS-DA is a supervised discriminant method derived from PLS regression models.[81] **Figure 3.4** shows the process of PLS calculation. Similar to PCA, PLS is also a powerful data compression technique that can condense the original data with a large number of initial variables to a dataset with only a few variables. In contrast to PCA, PLS not only considers the variation in the original multi-dimensional dataset generated by analytical measurement (e.g., MIR spectra, matrix ***A*** in Figure 3.4), but also simultaneously takes into account the variation in the original multidimensional value dataset (e.g., concentration, matrix ***C*** in Figure 3.4). In short, a PLS model will try to find the multidimensional direction in the analytical measurement sample data matrix **(*A*)** that explains the maximum multidimensional variance direction in the actual sample value matrix (***C***). The orthogonal directions of largest variances within the original analytical measurement or actual value dataset (the usually rather large number of variables contributing to the total variance) is reduced to a much smaller set of so-called *latent variables* (LVs).

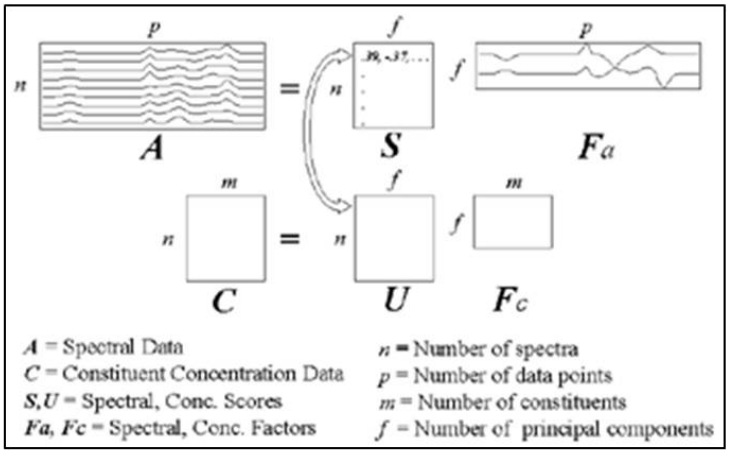

Figure 3.4 Demonstration of PLS compression and regression.

During the PLS-DA, PLS is adjusted for classification purposes such that training samples from different classes are assigned a different number, usually ‘1’ or ‘0’. Thus, the prediction results will give a ‘yes’ or ‘no’ answer regarding the relationship to a specific class. A threshold in PLS-DA needs to be established for separating the predicted values for class assignment purposes. Here, the threshold for separating two classes is calculated using the observed distribution (P_1, $P_2 \ldots P_n$; n = number of classes; P_n = probability of one object belonging to class n) of the predicted values, and the Bayesian theorem, which calculates the probability of one object belonging to a certain class by the ratio of $P_i/\sum P_n$ for discriminating different classes. For classification applications, PLS is guided by among-group variance, while PCA is guided only by the total variance and cannot discriminate among-group from within-group variance. It is explicit that PLS-DA provides favorable discrimination in contrast to PCA, in particular if the within-group difference dominates over the among-group difference, since PLS inherently considers class differences (while PCA does not) during the data compression.

3.3.2.4 Mahalanobis Distance

The Mahalanobis distance[82, 83] is a specific linear discriminant analysis method particularly suitable for classification because it maximizes the among-class difference relative to the within-class difference. In the work presented here, this procedure is performed by first compressing the spectral data into principle components or latent variables and corresponding scores by using PCA or PLS. After this, the mean score vector S_{mn}, and the mean-centered scores S_{mc} for each class were calculated, and the covariance matrix M of S_{mc} for each class was computed. For the prediction of an unknown sample, its score was calculated from the measured spectrum and principal components or latent variables, and mean-centered by the S_{mn} of one class. The distance D^2_j of the mean-centered unknown score t_j from S_{mn} of this class was computed and normalized by M following **Eq. 3. 1**.

$$D_j^2 = (t_j)M^{-1}(t_j)'$$

Eq. 3. 1

where $M = \frac{S_{mn}' S_{mn}}{m-1}$ with m indicating the number of training samples in one class. The distance calculation of an unknown sample to the center of covariance distribution of mean-centered scores of one specific class is graphically illustrated in **Figure 3.5**. The distance of an unknown sample to the centers of the classes determines which class the unknown belongs to. The class that has less distance to the unknown will incorporate the unknown sample.

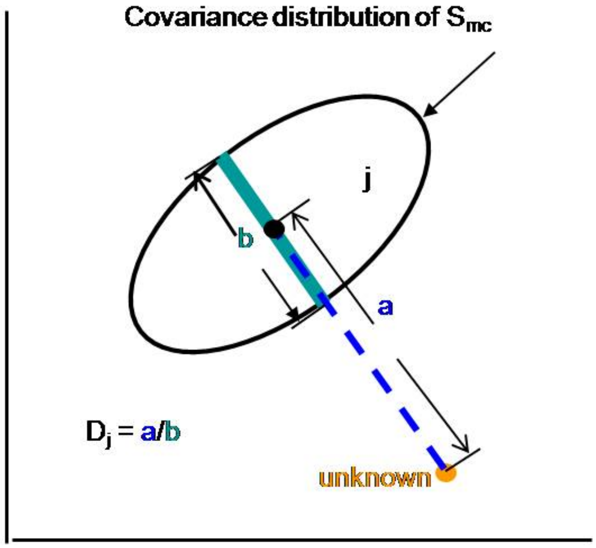

Figure 3.5: 2-D demonstration of Mahalanobis distance calculation for an unknown to the covariance distribution center of mean-centered scores of one class. a – distance of unknown to the center of group *j*; b – ellipse diameter of covariance distribution of mean-centered scores for group *j* along the direction of unknown to the group *j* center.

3.4 Experimental

3.4.1 Aorta Sample Preparation

Five New Zealand White male rabbits were used to obtain the training sample set for building the classification models in this study. Two of the rabbits (13 weeks-old) were fed with a normal diet of rabbit chow. The remaining three rabbits were fed rabbit chow supplemented with 1% (w/w) cholesterol (Harlan Teklad, Indianapolis/Indiana) daily for 8 weeks to induce atherosclerotic lesions.[84] The aorta biopsy preparation process is schematically displayed in **Figure 3.6**. One more normal-fed and one more cholesterol-fed rabbit (approx. 13 weeks old) were used to obtain the first set of test samples (12 in total) for validation of the established classification models. Their weight and blood cholesterol level were monitored every other week. For harvesting the aorta tissue, the rabbit was anesthetized and treated with an overdose of sodium pentobarbital. After euthanasia, the aorta tissue was excised and stored in 0.9% sodium chloride (NaCl) solution. Normal and atherosclerotic aortas (or aorta areas) were identified by visual inspection. Aortas from the rabbits on normal diet appeared inconspicuous without evident lesions. One cholesterol diet rabbit revealed lesion streak scattering along the inner wall of the aorta; two cholesterol diet rabbits were characterized by atherosclerotic aortas, where the aorta inner wall was entirely covered by lesions. Tissue samples were cut into segments with a diameter of 4mm using a biopsy device (Bio-punch, Health Link, Jacksonville/Florida) for spectroscopic measurement. The work discussed above was assisted by Ellen Dixon- Tulloch (Duke University, Dept. of Biomedical Engineering) and performed during a research stay at Duke University in collaboration with Dr. Richard Palmer (Duke University, Dept. of Chemistry).

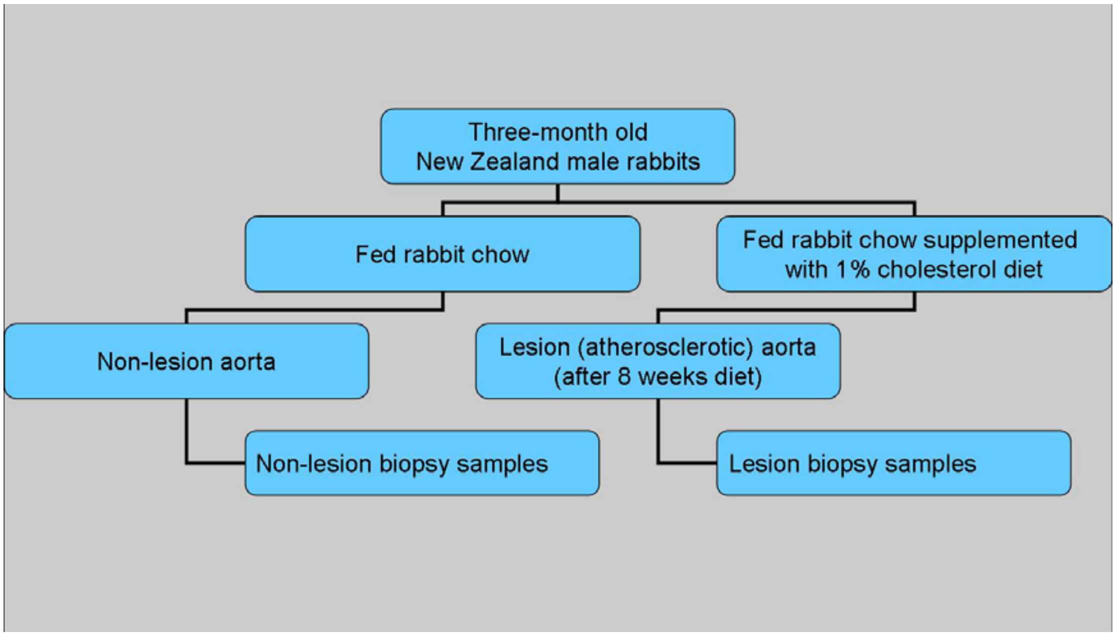

Figure 3.6: Scheme of rabbit aorta biopsy sample preparation.

3.4.2 Instrumentation and Data Acquisition

3.4.2.1 Custom-Built IR-ATR Catheter

A recently developed IR-ATR catheter prototype for future *in vivo* diagnostic and therapeutic applications was used *ex vivo* to collect spectra from normal and atherosclerotic aorta samples.[1, 2] This catheter is composed of two silica hollow waveguides (HGW; Polymicron Technologies, Phoenix/AZ) with a length of 1m and an inner diameter of 500µm (840µm outer diameter) connected to a cylindrical ZnSe ATR tip with a 45° tip cone providing a top surface area of approx. 1.57mm^2 (**Figure 3.7**). The HGWs provide low attenuation losses in the spectral range of 2-10µm (approx. 0.15dB/m), and a small numerical aperture (NA; 3° at full angle). The small NA provides for IR radiation to be reflected at the interface of the ATR tip and the tissue, rather than being refracted into the tissue. Additional losses are encountered if the HGW is bent, with

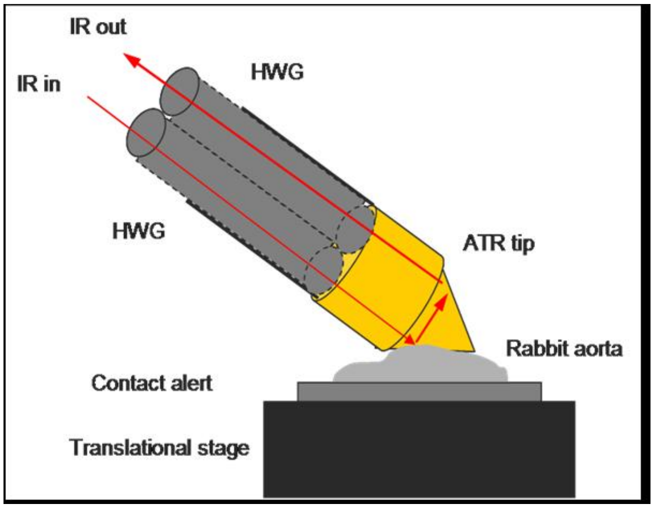

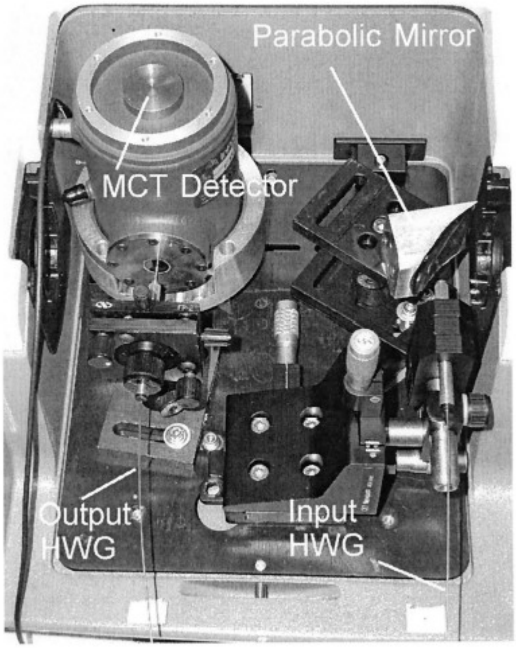

Figure 3.7: (top) Scheme of IR-ATR catheter measurements at rabbit aorta biopsies. The interface between the HWGs and the conical ATR tip was secured by a stainless steel sleeve; (bottom) optical assembly for guiding IR light into HWG and detecting light out from IR-ATR catheter[2].

the attenuation losses being inversely proportional to the bending radius.[85] Since the spectroscopic analysis in this study utilizes ratios of peak intensities rather than absolute peak values, changes in the overall signal intensity will not affect quantitative signal analysis if the HGWs are statically bent. In turn, the considerable flexibility of HGWs benefits the movement of catheter during insertion, which is essential for future *in vivo* applications. Radiation from a FT-IR spectrometer (Thermo Nicolet, Nexus 470, Thermo Electron Corp., Somerset/NJ) was focused into one IR HWG and directed onto the interface between the ATR crystal and the tissue. The illuminated tissue area was approx. 1.57 mm^2. Radiation reflected back into the distal HWG was directed onto a liquid nitrogen cooled mercury cadmium telluride (MCT) detector.

Hydrated and dehydrated tissue samples were prepared and separately investigated. Hydrated biopsies were kept in 0.9% NaCl solution during measurements. Dehydrated biopsies were prepared by rinsing with deionized water, drying with lens paper, and exposure to air for approx. 10min. The biopsy samples were then positioned on a glass slide centered on a 2-D adjustable sample stage. The ATR sensor head of the catheter was fixed above the sample stage at an angle of 45º. In order to provide reproducible contact between the ATR tip and the tissue samples while preventing puncture of the tissue samples, an experimentally optimized constant pressure (0.5mA) was applied between the optical ATR tip of the catheter, and the tissue samples. Thereby, it was ensured that the obtained signal exclusively results from the intima of the aorta sample. Constant pressure was achieved by slowly adjusting the height of the sample stage while monitoring the pressure with a contact alert system (Contact Alert, Spectra Tech). Constant pressure was maintained during each data acquisition period, ensuring that spectral differences caused by pressure variation were avoided. In previous studies, Katzir *et al.* characterized and differentiated tissues with unclad silver halide fibers, flattened silver halide waveguides, or silver halide fibers connected to a diamond ATR element utilizing similar measurement procedures, but, without active contact pressure control.[86,87] Hence, while fiberoptic sensing techniques proved successful in characterizing or differentiating tissues, such IR data is not suitable for multivariate data analysis due to potential spectral variations introduced by the change of contact pressure. An image of the setup for IR-ATR measurements with contact alert is shown in **Figure 3.8**. Prior to the measurements at each sample, the ATR tip was rinsed with deionized

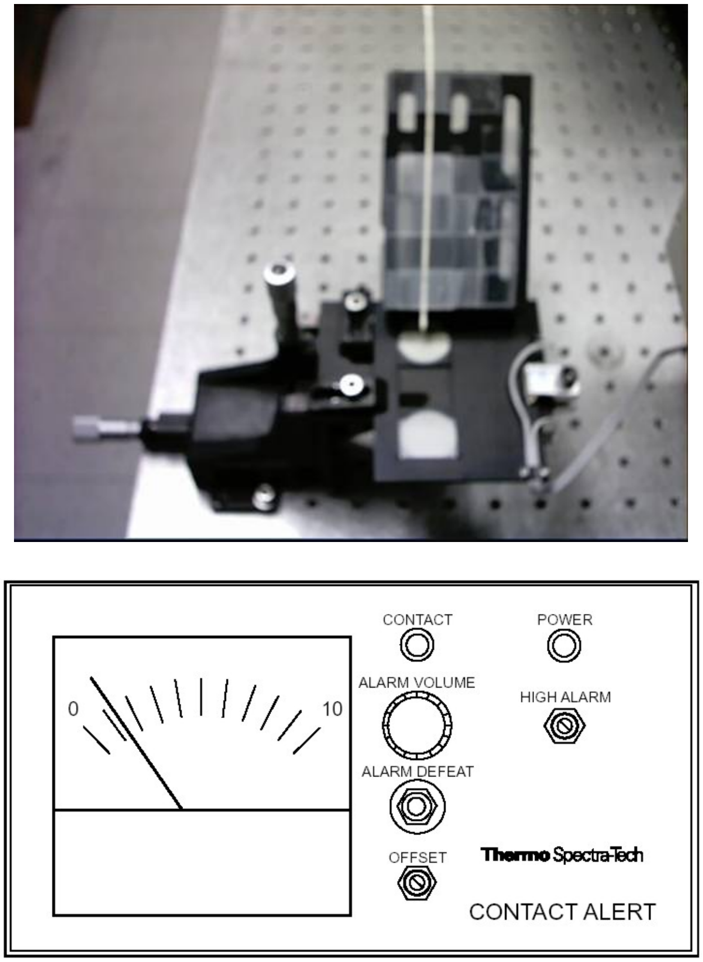

Figure 3.8: System setup for IR-ATR catheter measurement with contact alert.

water followed by acetone, and a new reference (background) spectrum was collected prior to each sample data acquisition eliminating spectral artifacts. A total of 128 scans was averaged at a spectral resolution of 4cm^{-1} during each measurement. Spectra were collected in a spectral range of 5000-400cm^{-1}.

For both hydrated and dehydrated tissue studies, aorta samples from one normal and one cholesterol diet rabbit were used. Visual inspection revealed no detectable lesions at the intima of normal diet rabbit aorta samples, while the intima of cholesterol diet rabbit aorta was entirely covered with visible lesions. Biopsy samples from normal diet rabbits were considered representative non-lesion samples, while samples from cholesterol diet rabbits were used as representative lesion samples. For hydrated tissue experiments, four biopsy samples for each kind of aorta were prepared, and five spectra from different locations were collected from each hydrated biopsy. For dehydrated tissue experiments, additional measurements at different locations on an individual biopsy sample were performed, resulting in a total of 21 lesion spectra and 32 non-lesion spectra.

3.4.2.2 Reflection Microspectroscopy

Reflectance spectra (single beam), which were collected with an FT-IR spectrometer (Thermo Nicolet, Nexus 470, Thermo Electron Corp., Somerset/New Jersey) coupled to an IR microscope with cassegrainian optics (**Figure 3.9** (left), Spectra-Tech IR Plan, Vermont Optechs Inc., Charlotte/Vermont), were used as training data to build multivariate models for classifying lesion and non-lesion aorta tissue. The biopsy sample (diam. 4mm) was placed on a glass slide, and the slide was positioned at the microscope stage. The distance between IR objective and sample was adjusted by focusing white light at the sample surface. The principle of reflection measurements is shown in **Figure 3.9** (right). Spectra were collected at $4cm^{-1}$ resolution from 650 to $4000cm^{-1}$ averaging 32 interferometer scans per measurement from a 100x100μm spot. All lesion aorta samples were obtained from one of three cholesterol diet rabbits; non-lesion aorta samples were prepared from the 13 months old normal diet rabbit. A total of 14 biopsies from each kind of sample (lesion and non-lesion) were collected. Two IR reflectance spectra were recorded for each biopsy. The two measurements at each biopsy are denominated *hydrated* and *dehydrated* in the remainder of this study. The hydrated sample spectrum of each hydrated and dehydrated set was measured three minutes after removal of the sample from the saline. The dehydrated sample spectra were measured 8min thereafter. By

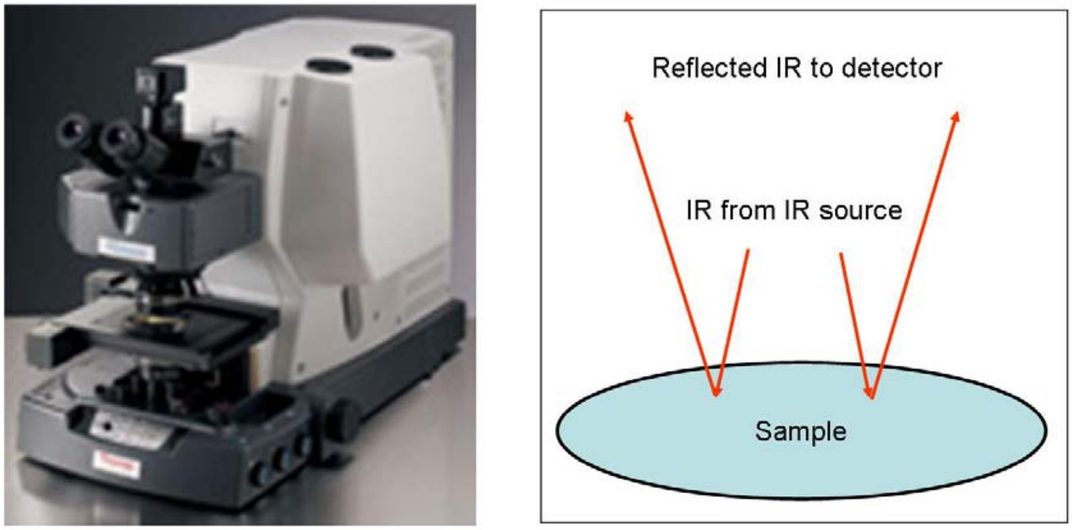

Figure 3.9: (left) IR microscope of Spectra-Tech IR Plan; (right) Scheme of light reflection from the sample surface. Radiation from the IR source interacts with the sample after passing through the IR objective. Reflected light from the sample is collected by the IR objective, and then guided to the IR detector by additional optical components.

standardizing the data collection in this way, the effects of loss of water to evaporation were presumed to be reproducible from sample to sample for each set of spectra of hydrated or dehydrated samples. Since the maximum penetration depth for MIR radiation into tissue is approximately 10μm (or less in the presence of water), it can also be assumed that the reflectance signals obtained were generated entirely or at least predominantly from the intima[6].

One set of test samples was independently investigated following the same procedure described above. These samples were collected from another two rabbits: one control and one cholesterol diet rabbit. The data obtained were then classified utilizing the multivariate classification models developed in the first phase of this study, namely PCA, PLS-DA, PCR, Mahalanobis distance.

3.4.2.3 Bench-top IR-ATR Spectroscopy

IR-ATR spectra were collected with a 45º single reflection diamond ATR accessory (**Figure 3.10**, Golden Gate, Specac Ltd., Orrington/UK) coupled to the same FT-IR spectrometer by placing it in the sample compartment. In total, 29 dehydrated biopsy samples with a diameter of 4mm were investigated comprising 10 lesion, and 19 non-lesion samples. Prior to the measurement, each biopsy sample was prepared by rinsing with DI water, drying with lens paper, and then exposure to air for approx. 10min. The dehydrated tissue samples were centered at the top of the circular diamond ATR element. To ensure sufficient contact between the tissue sample and the diamond, a constant pressure was applied via a built-in adjustable plunger and monitored by a torque wrench.

Spectra were collected at 4cm^{-1} resolution from 4000 to 400cm^{-1} averaging 16 spectra per measurement.

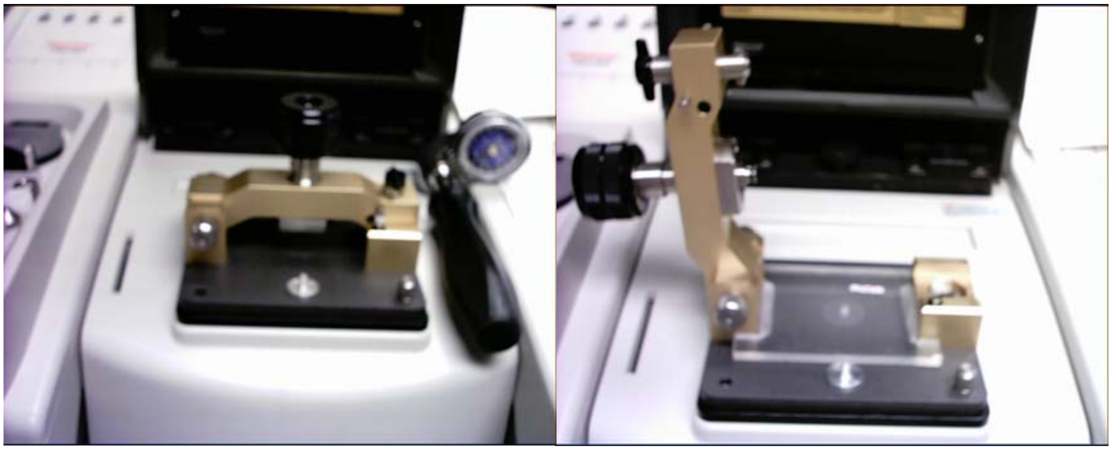

Figure 3.10: Golden gate single-bounce diamond ATR accessory for IR-ATR spectroscopy measurement.

3.4.3 Multivariate Data Analysis

PLS_Toolbox_3.5 (Eigenvector Inc., Wenatchee/Washington) was used to generate the classification models. PCA, PCR, PLS-DA, and Mahalanobis distance were adopted, and applied to hydrated and dehydrated tissue data sets obtained with the IR-ATR catheter and IR reflection microspectrometry methods. The spectra obtained for each particular set of experiments were always mean-centered prior to multivariate analysis. Cross-validation (leaving one sample out) was performed to determine the optimal number of principal components (PC) or latent variables (LV).

3.5 Results and Discussion

3.5.1 Custom-Built IR-ATR Catheter

3.5.1.1 Average IR Spectra of Classification Data

Figure 3.11 shows an example of the average spectra of dehydrated lesion and non-lesion tissue samples collected with the prototype IR-ATR catheter. The spectra are characterized by considerable noise levels, due to the reduced signal throughput of the IR-ATR catheter device. Spectral differences are evident between the average spectra, in particular at 2927, 2855, and 1753cm^{-1}, representing the spectroscopic features of lipid/lipid ester associated with cholesterol deposition. Absorbances are increased at these frequencies for lesion tissue compared to non-lesion tissue relative to other absorption bands in the spectrum. For comparison, **Figure 3.12** shows the average spectra of hydrated tissue samples, where it is evident that the differences are not as strong; consequently, it is impossible to directly distinguish whether the sample is a lesion or non-lesion case. Hence, implementing multivariate data analysis techniques is essential.

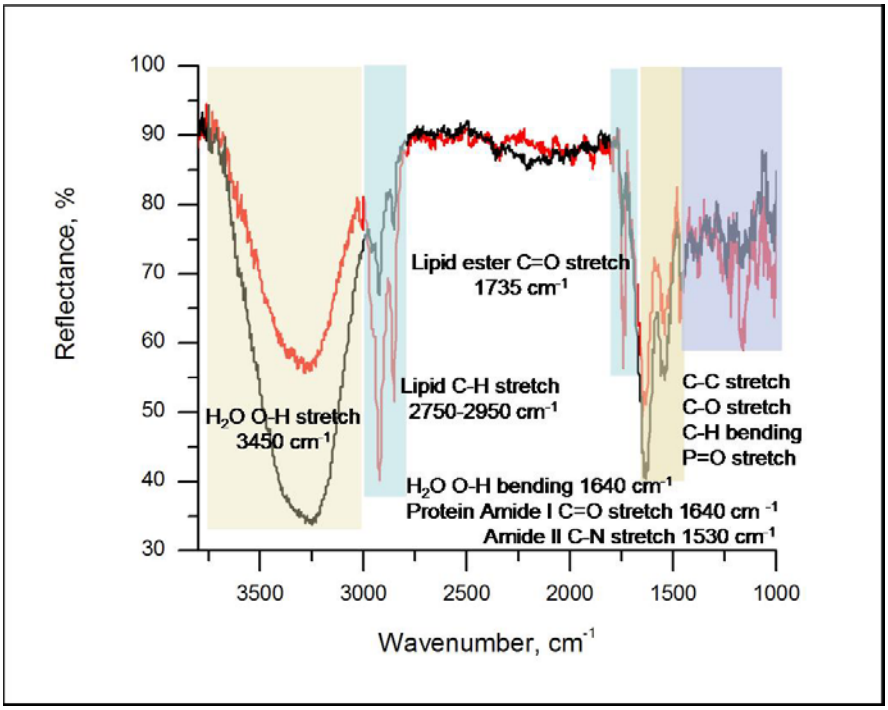

Figure 3.11: Red – average of dehydrated lesion sample spectra using the IR-ATR catheter; black – average spectrum of dehydrated non-lesion samples using the IR-ATR catheter.

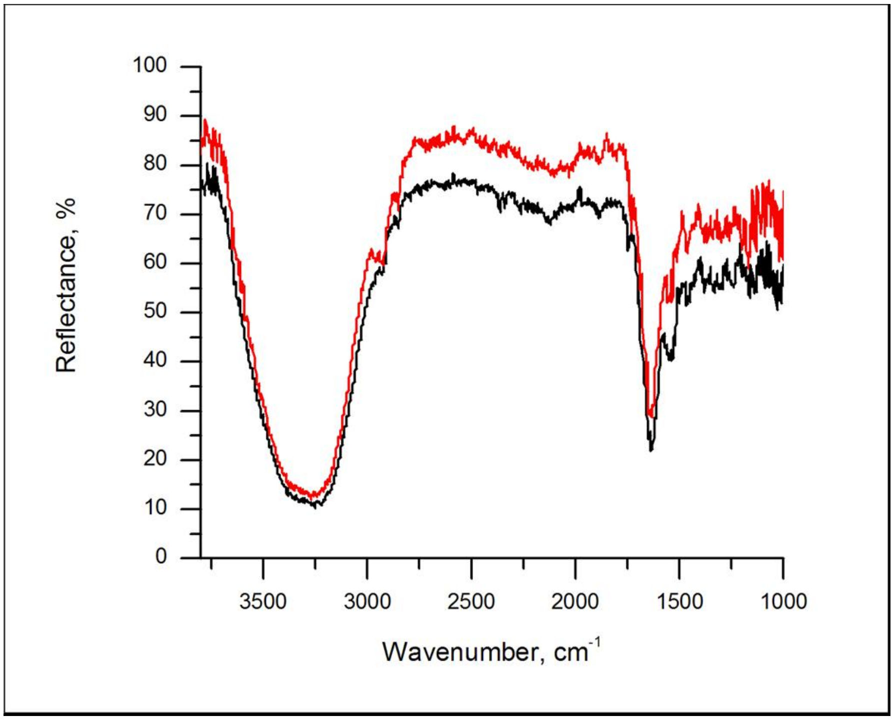

Figure 3.12: Red – average of hydrated lesion sample spectra using the IR-ATR catheter; black – average spectrum of hydrated non-lesion samples using the IR-ATR catheter.

The spectral region from 3800-1000cm^{-1} was selected for establishing multivariate classification models.

3.5.1.2 Multivariate Data Analysis

The estimation errors were evaluated by resubstitution and bootstrap resampling techniques, respectively.[88] For determining the resubstitution error estimate, all samples were used to build the classification models, and the class membership of the same set of samples was predicted. Since the resubstitution method frequently generates overly optimistic bias in the error estimation for small data sets, the bootstrap resampling technique was also applied to the prediction error rate study. For bootstrap resampling, a training data set (i.e., a ‘bootstrap’ sample) was formed by randomly selecting samples with replacement from the original data set, with the same sample size for both sets. The samples removed from the training data set provide a corresponding test data set. This generation of training and test data sets was repeated 25 times in this study followed by the model development and evaluation strategy mentioned above.

3.5.1.2.1 Resubstitution related multivariate data analysis and error estimation

All applied multivariate data analysis methods (PCA, PLS-DA, and Mahalanobis distance) provided consistent classification results at hydrated and dehydrated tissue data with a prediction probability of 1 for each sample in all models following Bayesian statistics, if the resubstitution method was applied. **Figure 3.13** - **Figure 3.18** are the corresponding multivariate data analysis results using the resubstitution method.

Two and three PCs were selected to build PCA models for both hydrated and dehydrated samples based on the root mean square error for cross validation (RMSECV). The corresponding results are shown in **Figure 3.13** and **Figure 3.14**. It is clearly evident that lesion and non-lesion samples were well separated into two categories.

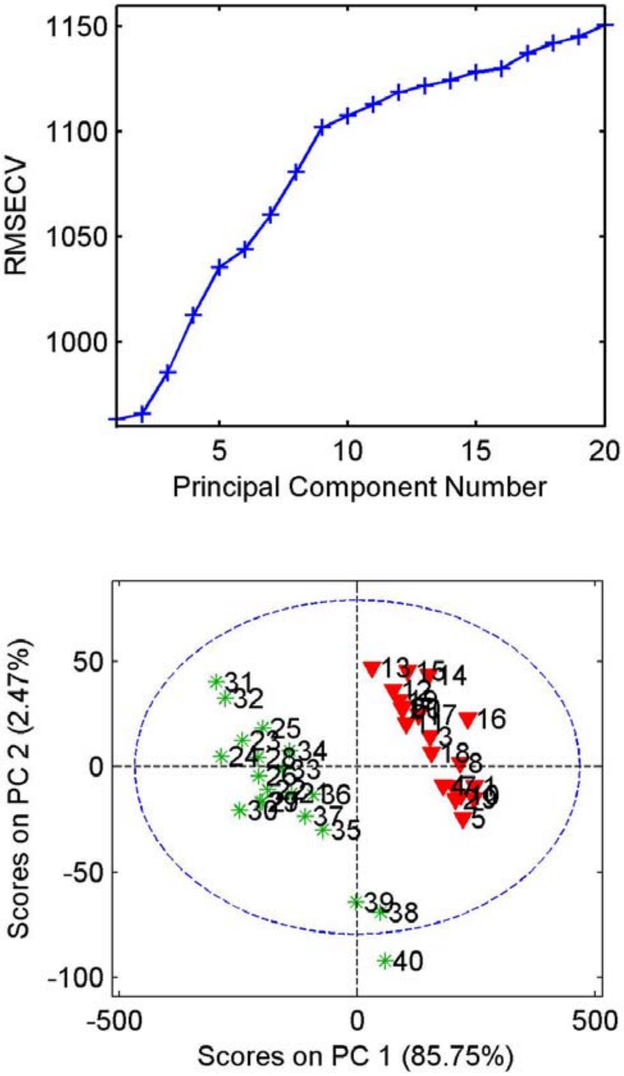

Figure 3.13: (top) RMSECV of PCA; (bottom) PCA classification results at hydrated samples for the IR-ATR catheter. Green stars – non-lesion training samples; red triangles – lesion training samples.

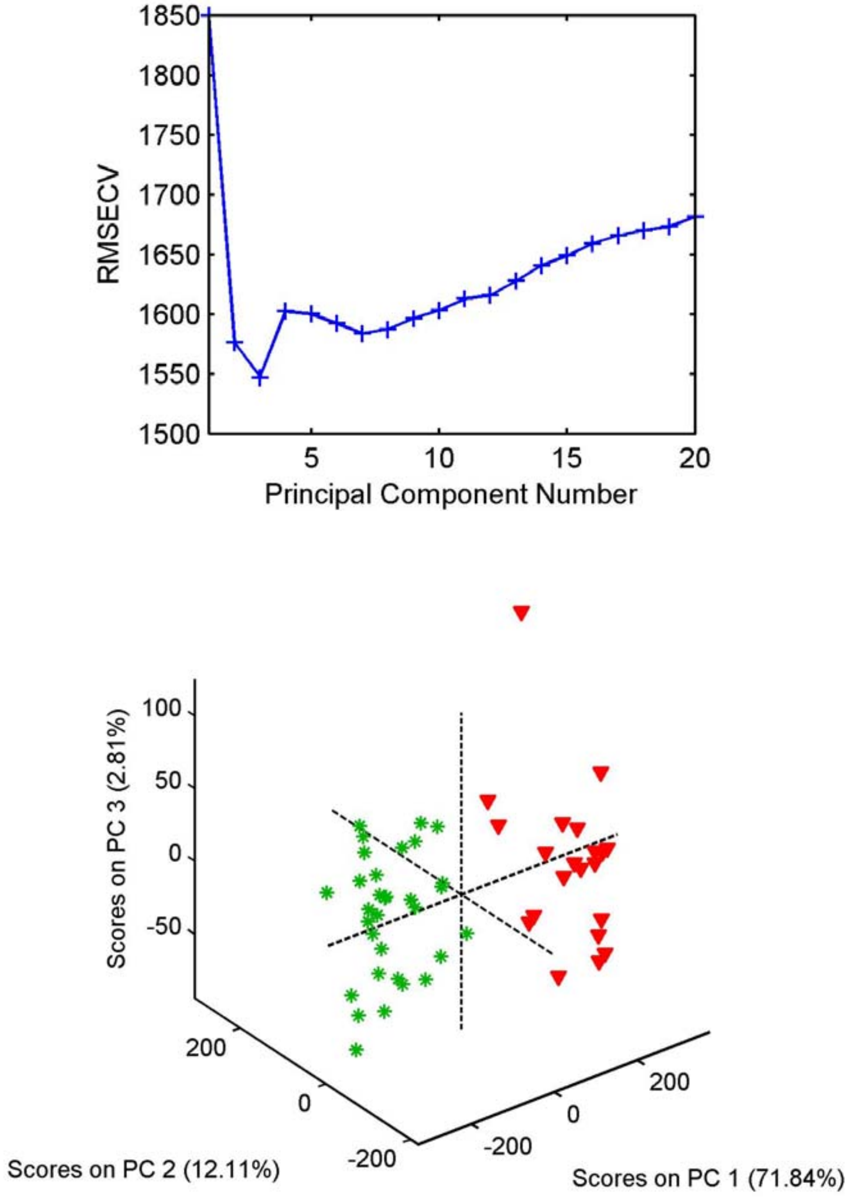

Figure 3.14: (top) RMSECV of PCA; (bottom) PCA classification results at dehydrated samples for the IR-ATR catheter. Green stars – non-lesion training samples; red triangles –lesion training samples.

Based on the RMSECV, three latent variables (LVs) were selected to build PLS-DA statistical models for both hydrated and dehydrated samples. The corresponding classification results are shown in **Figure 3.15** and **Figure 3.17**. Ideally, lesion samples have value of 0.5, and non-lesion samples have value of -0.5. However, the predicted values frequently deviate from the ideal values due to the spectral variation of the samples within the same class.

Threshold values were calculated using the observed distribution of the predicted values, and the Bayesian theorem for discriminating the two different classes. As shown in **Figure 3.16**, the blue bars represent a histogram of the predicted values for class 1 samples; the green bars provide a histogram of the predicted values for class 2 samples. The threshold is the cross point of two normally fitted histograms. Bayesian statistics also provide the probability whether a sample is a member of a certain class given the predicted value. The prediction probability results for the 3LV PLS-DA model based on all investigated samples are 1. Given a sample, its probability belonging to class 1 is calculated using **Eq. 3. 2**.

$$probability(class1) = \frac{P(y,1)}{[P(y,1) + P(y,2)]}$$

Eq. 3. 2

where y is the predicted value from the PLS-DA model for the sample in question, $P(y,1)$ is the probability of this sample to be a member of class 1 given the value of y, and $P(y,2)$ is the probability of this sample to be a member of class 2 given the value of y. Consequently, a sample with a predicted value at the threshold has a 50% probability belonging to either class.

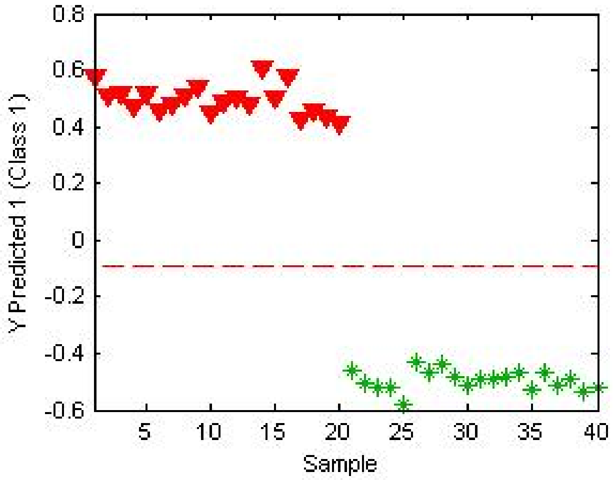

Figure 3.15: PLS-DA classification results at hydrated samples for the IR-ATR catheter. Green stars – non-lesion training samples; red triangles –lesion training samples.

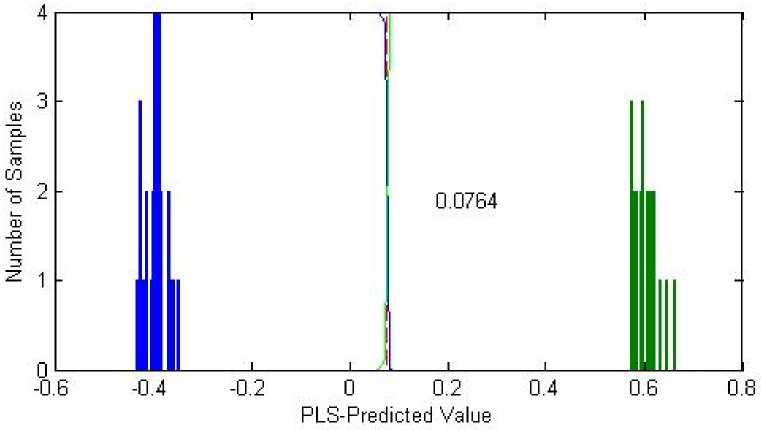

Figure 3.16: Histograms for PLS-DA model at hydrated samples for the IR-ATR catheter. Blue – distribution of non-lesion training samples; green – distribution of lesion training samples.

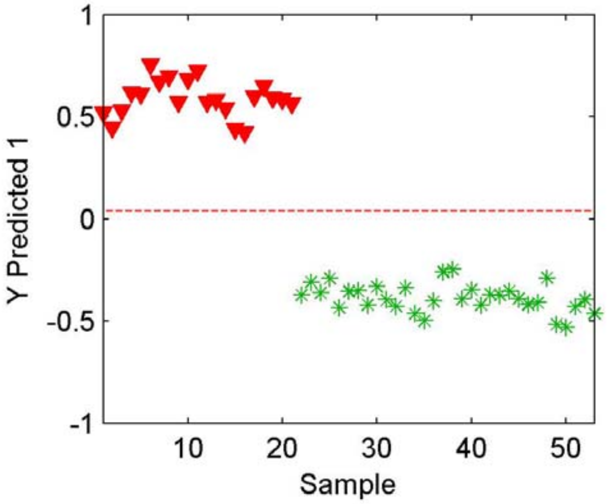

Figure 3.17: PLS-DA classification results at dehydrated samples for the IR-ATR catheter. Green stars – non-lesion training samples; red triangles –lesion training samples.

All lesion samples were also used to conduct a Mahalanobis distance analysis. The results obtained with the corresponding classification models are shown in **Figure 3.18**. Apparently, the Mahalanobis distance method has enabled 100% successful classification of all samples, similar to PCA and PLS-DA.

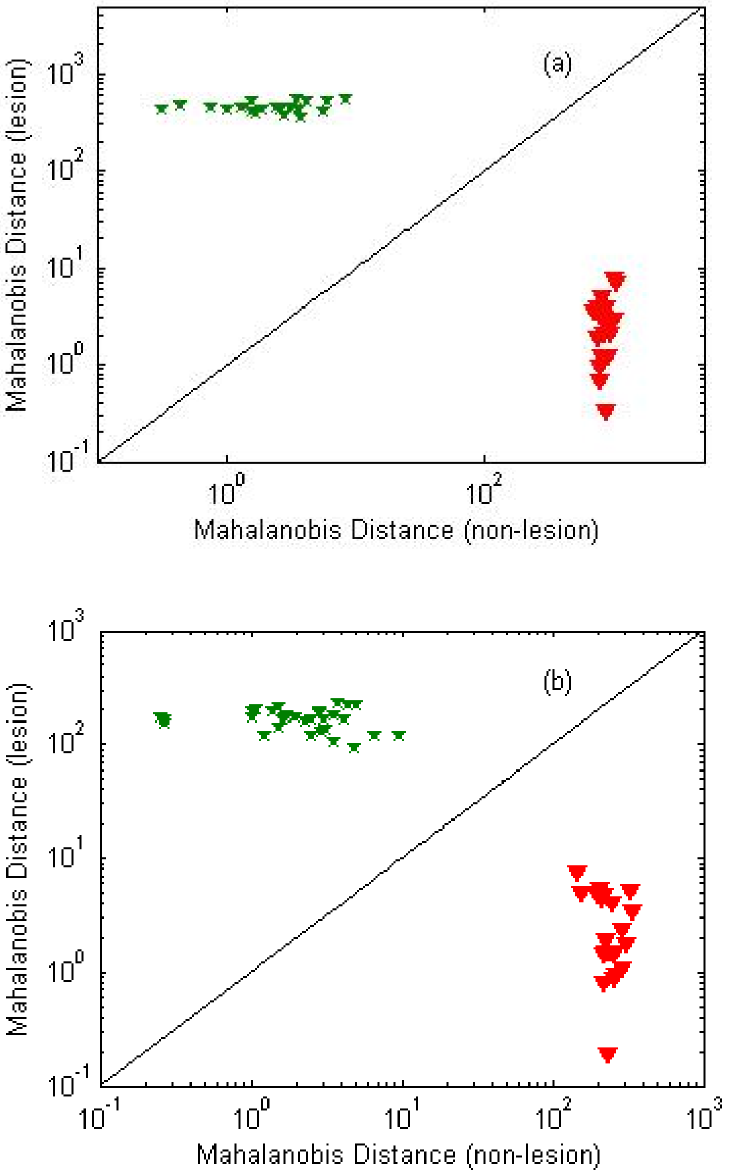

Figure 3.18: Mahalanobis distance classification results at (a) hydrated samples; (b) dehydrated samples for the IR-ATR catheter. Green stars – non-lesion training samples; red triangles –lesion training samples.

Finally, all lesion samples were assigned a value of one, and non-lesion samples were assigned a value of zero before establishing a classification model based on principle components regression (PCR).[89] The optimal numbers of principle components (PC) for establishing the classification model based on data obtained from hydrated and dehydrated tissue were 2 and 7, respectively, based on the root mean square error for cross-validation (RMSECV). The results obtained with the corresponding PCR classification models are shown in **Figure 3. 19**. Apparently, dehydrated tissue data

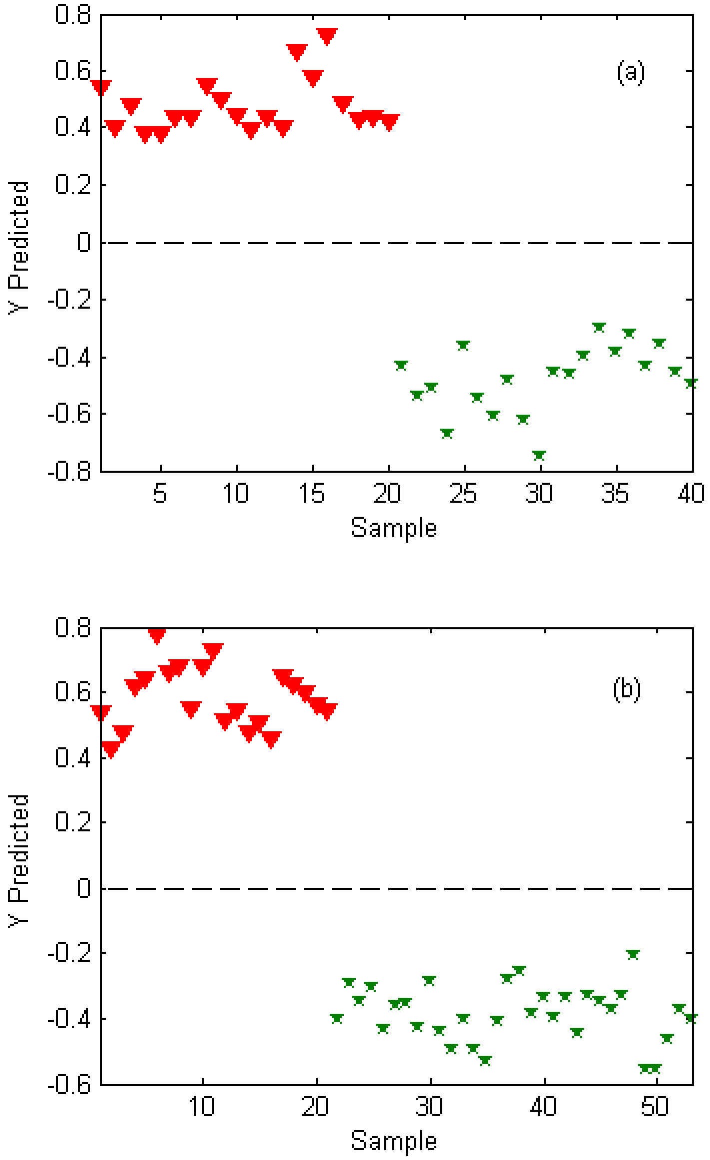

Figure 3. 19: Prediction results for PCR models using the the IR-ATR catheter. (top) hydrated samples; (bottom) dehydrated samples. Red triangle – lesion samples; green star – non-lesion samples.

require more PCs to establish robust well-classifying PCR models due to an increased within-sample variation introduced by the dehydration process.

It was anticipated that a minimum of 2-3 LVs or PCs are needed to build a classification model considering the spectral differences between the two types of tissues. This was confirmed by the data analysis results shown above. The major difference between PLS and PCR is that PLS considers not only the spectral difference, but also the class difference among the samples. This frequently results in fewer latent variables being needed in PLS in contrast to PCR, which is also clearly evident in the analysis results for the dehydrated tissue samples.

3.5.1.2.2 Bootstrap resampling related multivariate data analysis and error estimation

Twenty-five sets of pseudo training samples generated by bootstrap resampling were used to build PLS-DA and Mahalanobis distance classification sub-models, and then corresponding sets of pseudo test data were predicted. The error rate was calculated by averaging the prediction error of each test set with respect to the corresponding sub-model. For PLS-DA and Mahalanobis distance analysis of hydrated and dehydrated tissue sample spectra, the same prediction possibility of 1 was obtained for the bootstrap resampling related analysis, as for the analysis based on the resubstitution method. Box-whisker-plots are used to display the results for the test samples of each model. Since Mahalanobis distance classification obtained similar results as PLS-DA, only PLS-DA (**Figure 3.20**) results are shown here.

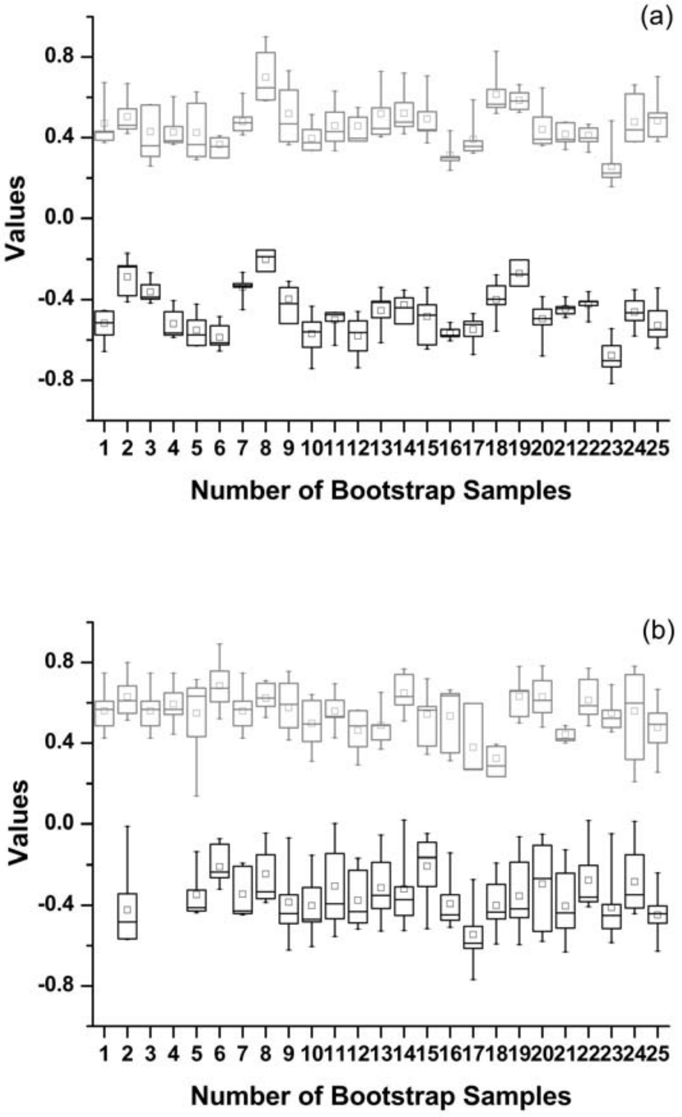

Figure 3.20: Boxplot of the PLS calculation results for the test samples using bootstrap sampling. (a) Hydrated samples; (b) dehydrated samples. Grey - lesion samples; black – non-lesion samples. The five-number summary of the boxes consists of the minimum, first quartile, median, third quartile, and maximum. The small square in the box represents the mean.

Both PLS-DA and Mahalanobis distance provided superior prediction results with error rates of zero.

It can be concluded that unsupervised PCA, supervised PLS-DA, and Mahalanobis distance classification provide sufficient performance for the discrimination of lesion vs. non-lesion tissue samples in this study. The dehydrated samples have comparatively broader distributions in all three models, which may be attributed to the introduction of within-group variation during the dehydration process.

While the IR-ATR catheter system combined with multivariate data analysis techniques revealed excellent potential for identifying lesion and non-lesion rabbit aorta tissues, collecting measurements for large data sets is not convenient for the preparation of extensive calibration models. Therefore, an effort was made by utilizing reflection microspectroscopy and bench-top IR-ATR spectroscopy to collect calibration data, and applying the data analysis strategies discussed before to these data to identify tissue types.

3.5.2 Reflection Microspectroscopy

3.5.2.1 Average IR Spectra of Classification Data

Average spectra of measurements of the training set (hydrated and dehydrated aorta samples) are shown in **Figure 3.21** and **Figure 3.22**. From these plots, it is clearly evident that the spectral differences between lesion and non-lesion tissue samples are very subtle. The experimental results obtained in this study convincingly demonstrate that sophisticated multivariate data analysis and classification techniques are essential to robust and reliable sample classification for diagnostic purposes.

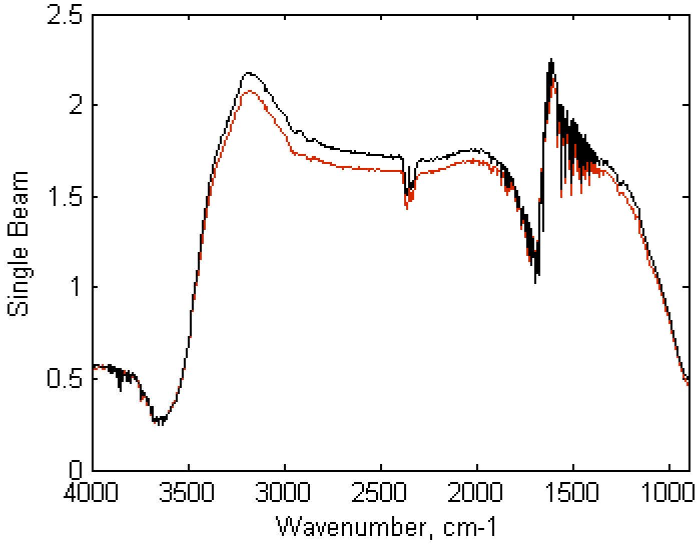

Figure 3.21: Red – average of hydrated lesion sample spectra; black – average spectrum of hydrated non-lesion samples using reflection microspectrometry.

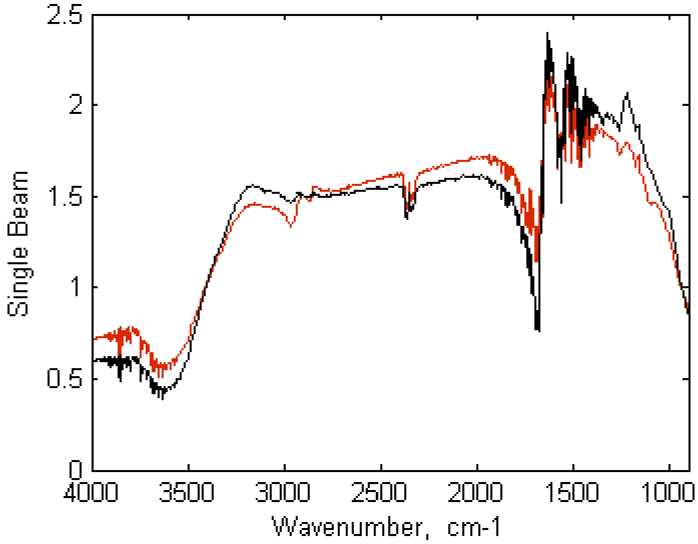

Figure 3.22: Red – average of dehydrated lesion sample spectra; black – average spectrum of dehydrated non-lesion samples using reflection microspectrometry.

3.5.2.2 Multivariate Data Analysis Using Spectra Range 4000-1000cm^{-1}

3.5.2.2.1 Multivariate classification results using hydrated sample data

In all plots shown below, points 1-14 represent lesion training samples (class 1); 15-28 non-lesion training samples (class 2); and 29-40 samples from a test set. The establishment of the model using the training samples (1-28) by L. Wang at Georgia Tech preceded the measurement of the unknown samples (by J. Chapman at Duke Univ.) by six months owing to tissue availability schedules. For the 12 samples from the test set, only the raw single beam IR spectra were provided for evaluation without any indication of the number of lesion *vs.* non-lesion cases among the 12 samples. The identity of the test samples was shared only after the classification had been made.

Two PCs were selected to build the calibration models based on the RMSECV (**Figure 3.23**). **Figure 3.24** and **Figure 3.25** show the classification models without and with certain training sample(s) excluded for optimizing the model quality. By excluding sample ‘7’, and sample ‘ 7 ‘and ‘25’ together, respectively, it appears that the model quality did not improve. With thus established calibration models, the test samples could not be predicted as expected (see **Figure 3.26** and **Figure 3.27**). For comparison, a 3 PC PCA model is shown in **Figure 3.28**. Obviously, it is not a functional model either.

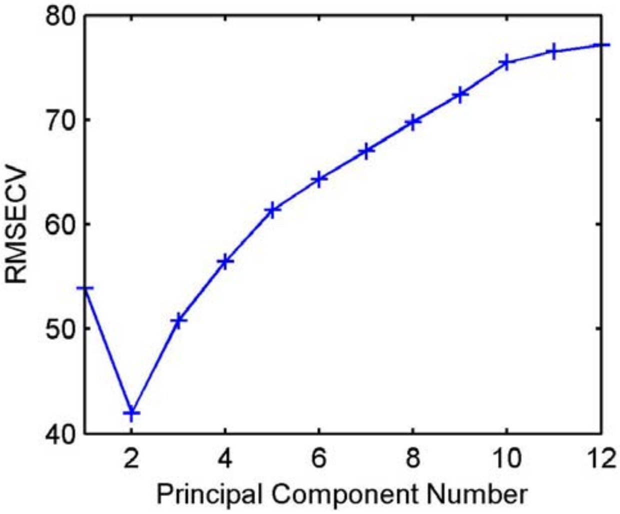

Figure 3.23: RMSECV of PCA at hydrated samples for reflection microscpectroscopy.

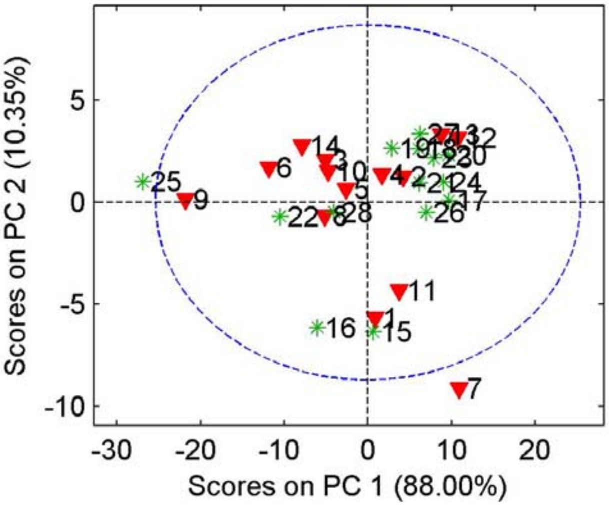

Figure 3.24: 2 PCs PCA classification results at hydrated samples for reflection microspectroscopy without any samples excluded. Green stars – non-lesion training samples; red triangles – lesion training samples.

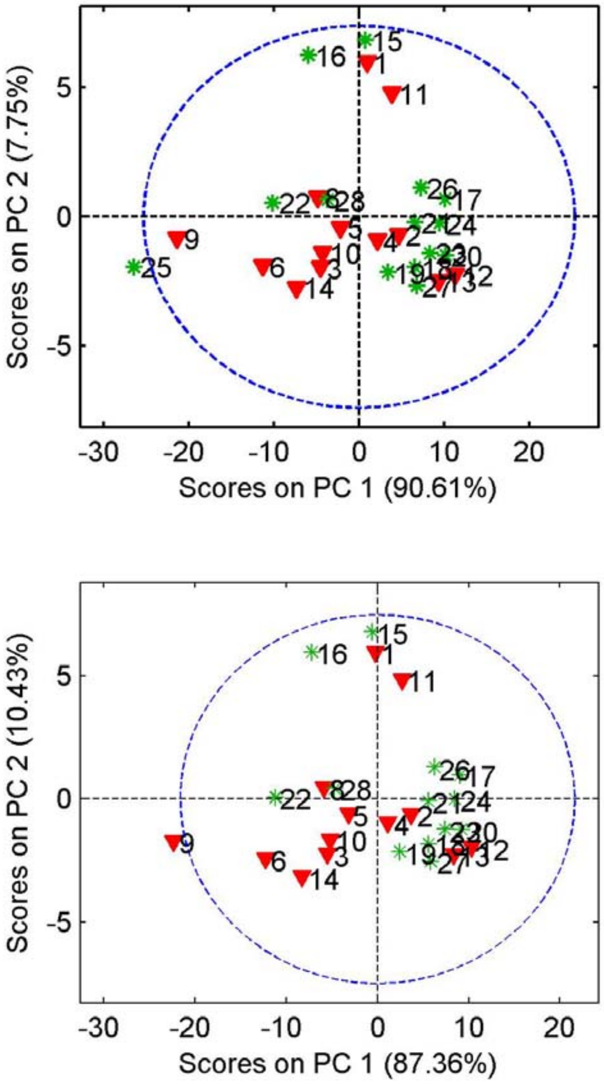

Figure 3.25: 2 PCs PCA classification results at hydrated samples for reflection microspectroscopy with samples excluded; (top) sample ‘7’ excluded; (bottom) ‘7’ and ‘25’excluded. Green stars – non-lesion training samples; red triangles – lesion training samples.

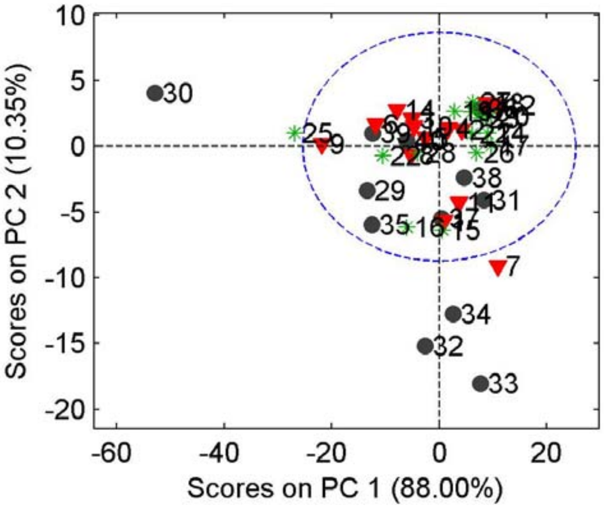

Figure 3.26: 2 PCs PCA classification and prediction results at hydrated samples for reflection microspectroscopy without sample excluded. Green stars – non-lesion training samples; red triangles – lesion training samples; black dot – test samples.

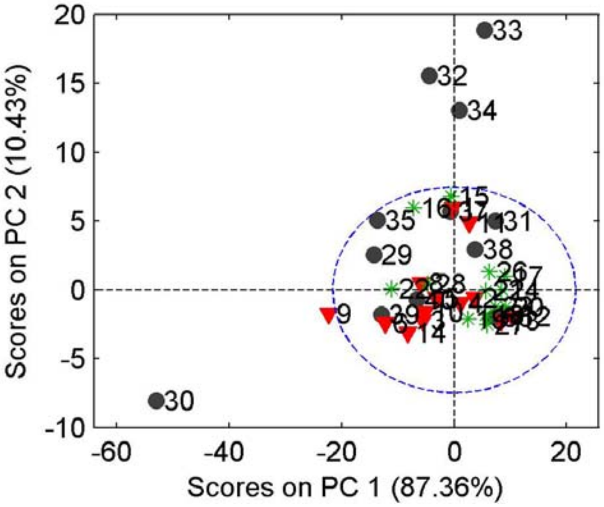

Figure 3.27: 2 PCs PCA classification and prediction results at hydrated samples for reflection microspectroscopy with sample ‘7’ and ‘25’excluded. Green stars – non-lesion training samples; red triangles – lesion training samples; black dot – test samples.

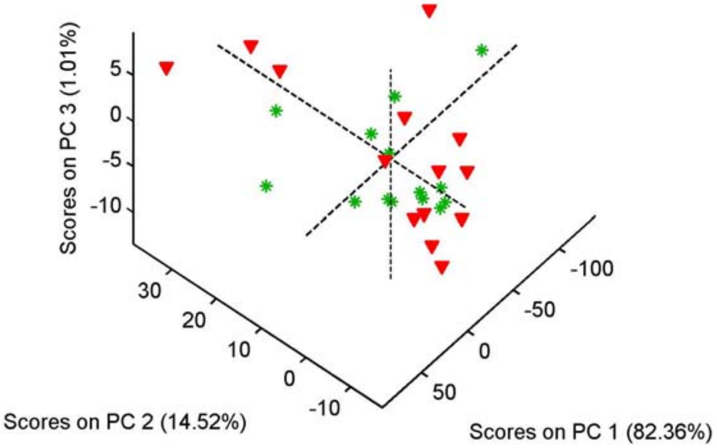

Figure 3.28: 3 PCs PCA classification results at hydrated samples for reflection microspectroscopy without sample excluded. Green stars – non-lesion training samples; red triangles – lesion training samples.

Based on RMSECV results for PLS-DA shown in **Figure 3.29** (top), 4 and 6 latent variables (LVs) were tested as optimal number to minimize the error during classification and prediction. The corresponding classification and prediction results are shown in **Figure 3.29** (bottom). In the model using four LVs, sample 10 cannot be unambiguously classified, but its probability of belonging to class 1 is > 50% (see **Table 3.1**). Using this model, only test sample '30' was incorrectly classified. If six LVs were applied to establish the model, all samples could be correctly classified or predicted.

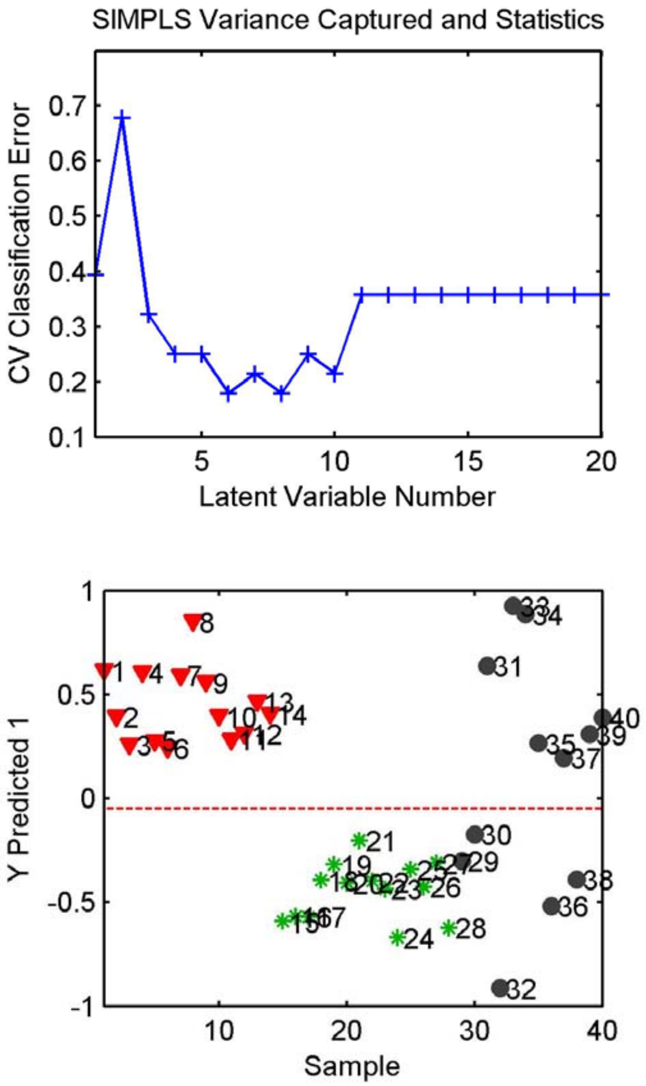

Figure 3.29: (top) RMSECV *vs*. LV number using data of hydrated training set samples. (bottom) Classification and prediction results for PLS-DA model 6LVs using hydrated sample data. Red triangles – lesion training samples; green stars – non-lesion training samples; black dots – test samples; Red line – threshold (-0.0507).

Table 3.1: Prediction probability results for PLS-DA models using hydrated data. 1-28: training sample set; 1-14: lesion sample set; 15-28: non-lesion sample set; 29-40: test samples.

Sample	Revealed class	Prediction probability			
		4 LVs		6 LVs	
		Class 1	Class 2	Class 1	Class 2
1	1	0.9848	0.0152	1	0
2	1	0.9921	0.0079	1	0
3	1	0.9274	0.0726	1	0
4	1	0.9995	0.0005	1	0
5	1	0.9489	0.0511	1	0
6	1	0.8146	0.1854	1	0
7	1	0.9959	0.0041	1	0
8	1	1	0	1	0
9	1	0.9989	0.0011	1	0
10	1	0.5937	0.4063	1	0
11	1	0.9682	0.0318	1	0
12	1	0.9267	0.0733	1	0
13	1	0.9967	0.0033	1	0
14	1	0.9778	0.0222	1	0
15	2	0.2024	0.7976	0	1
16	2	0.0017	0.9983	0	1
17	2	0.0001	0.9999	0	1
18	2	0.0413	0.9587	0	1
19	2	0.1192	0.8808	0.0001	0.9999
20	2	0.0146	0.9854	0	1
21	2	0.0001	0.9999	0.005	0.995
22	2	0.0185	0.9815	0	1
23	2	0.3082	0.6918	0	1
24	2	0.0011	0.9989	0	1
25	2	0.0218	0.9782	0.0001	0.9999
26	2	0.0069	0.9931	0	1
27	2	0.324	0.676	0.0002	0.9998
28	2	0.0241	0.9759	0	1
29	2	0.0991	0.9009	0.0002	0.9998
30	2	1	0	0.0126	0.9874
31	1	0.9999	0.0001	1	0
32	2	0.0001	0.9999	0	1
33	1	1	0	1	0
34	1	1	0	1	0
35	1	0.9767	0.0233	1	0
36	2	0.0044	0.9956	0	1
37	1	0.7582	0.2418	0.9999	0.0001
38	2	0.0006	0.9994	0	1
39	1	0.9957	0.0043	1	0
40	1	0.9992	0.0008	1	0

The Mahalanobis distance classification and prediction results based on 6 LVs of PLS-DA shown above are given in **Figure 3.30**. This method provided a 100% hit quality at training and test samples.

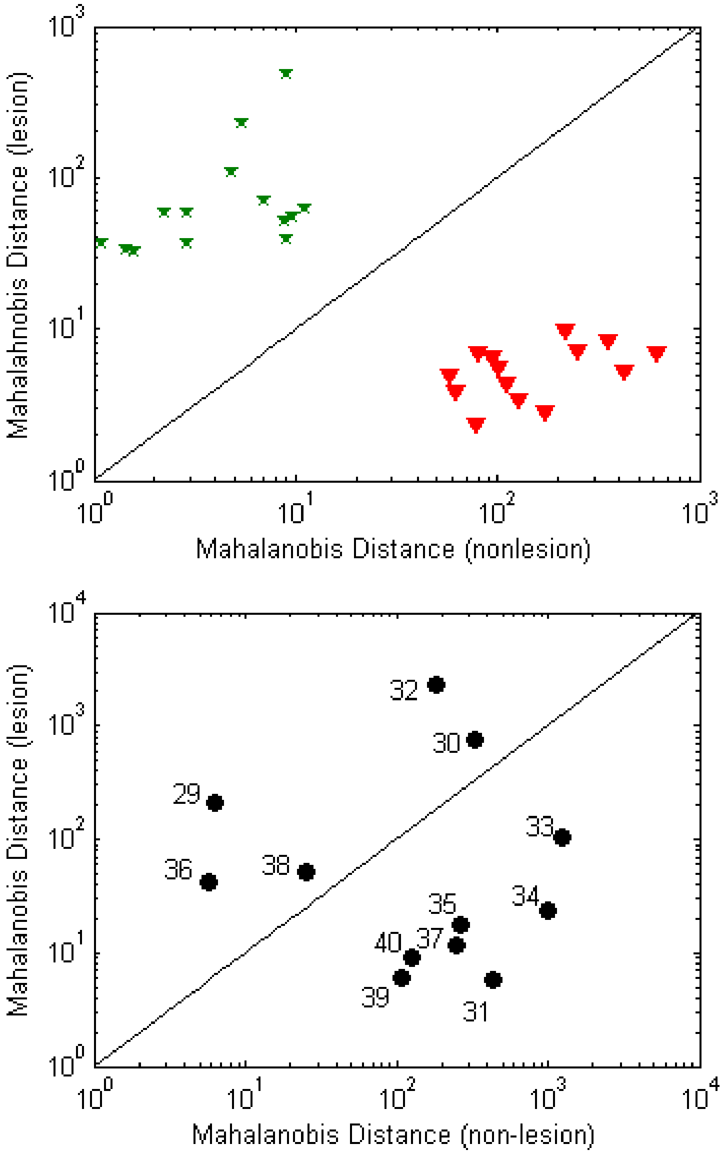

Figure 3.30: (top) Classification results of 28 training samples using the Mahalanobis distance method and hydrated data of training set samples. Green stars – non-lesion training samples; red triangles – lesion training samples; diagonal line – discriminant line. (bottom) Prediction results of 12 test samples using the Mahalanobis distance method and hydrated data of test samples. Diagonal line – discriminant line.

3.5.2.2.2 Multivariate classification results using dehydrated sample data

During further studies, PCA was applied on the obtained data. Based on the RMSECV results shown in **Figure 3.31**, three PC were selected as optimal number to minimize the error during classification and prediction. The corresponding classification and prediction results are shown in **Figure 3.32**. It is evident that lesion and non-lesion training samples are grouped well, although sample 24 and 26 locate relatively far from the group center area possibly due to the large within-group variance. Calculated from the established PCA model, the test samples were all correctly predicted, with only sample 40 close to the margin of two classification categories.

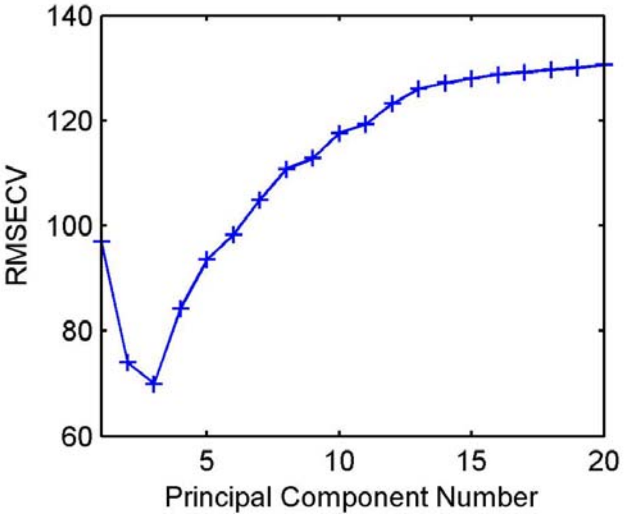

Figure 3.31: RMSQCV for dehydrated samples using reflection microspectroscopy.

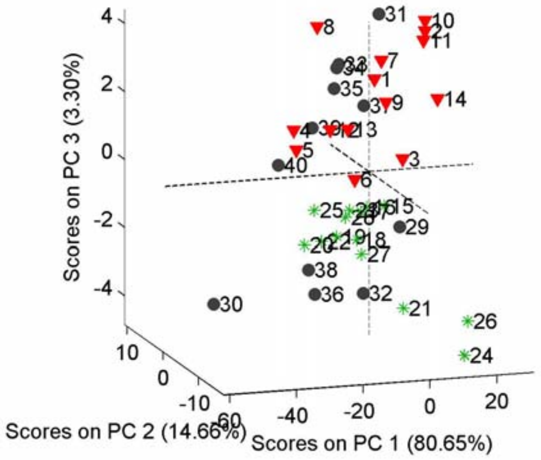

Figure 3.32: Classification and prediction results of PCA. Red triangles – lesion training samples; green stars – non-lesion training samples; black dots – test samples.

For PLS-DA analysis, 6 LVs were selected to build the statistical models. The corresponding classification and prediction results are shown in **Figure 3.33**. All training samples could be clearly classified with this method, and only test sample 40 could not be classified with sufficient certainty. Most probably, it would be incorrectly classified as a non-lesion sample.

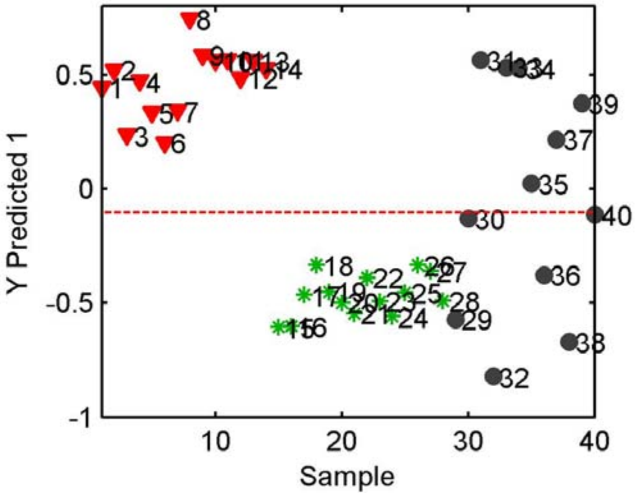

Figure 3.33: (top) Classification and prediction results for PLS-DA using dehydrated data. Red triangles – lesion training samples (class 1); green stars – non-lesion training samples (class 2); black dots – test samples; Red line – threshold (-0.1042).

The corresponding probability results for the PLS-DA model and dehydrated data are given in **Table 3.2**.

Table 3.2: Prediction probability results for PLS-DA models using dehydrated data. 1-28: training samples; 1-14: lesion samples; 15-28: non-lesion samples; 29-40: test samples.

Sample	Revealed class	Prediction probability 6 LVs	
		Class1	Class2
1	1	1	0
2	1	1	0
3	1	1	0
4	1	1	0
5	1	1	0
6	1	1	0
7	1	1	0
8	1	1	0
9	1	1	0
10	1	1	0
11	1	1	0
12	1	1	0
13	1	1	0
14	1	1	0
15	2	0	1
16	2	0	1
17	2	0	1
18	2	0	1
19	2	0	1
20	2	0	1
21	2	0	1
22	2	0	1
23	2	0	1
24	2	0	1
25	2	0	1
26	2	0	1
27	2	0	1
28	2	0	1
29	2	0	1
30	2	0.1634	0.8366
31	1	1	0
32	2	0	1
33	1	1	0
34	1	1	0
35	1	0.9999	0.0001
36	2	0	1
37	1	1	0
38	2	0	1
39	1	1	0
40	1	0.3682	0.6318

The Mahalanobis distance method was also applied to classify dehydrated data. The classification results are shown in **Figure 3.34**. Again, test sample 40 could not be correctly classified. Sample 30 could be classified more clearly using the Mahalanobis distance in contrast to using PLS-DA.

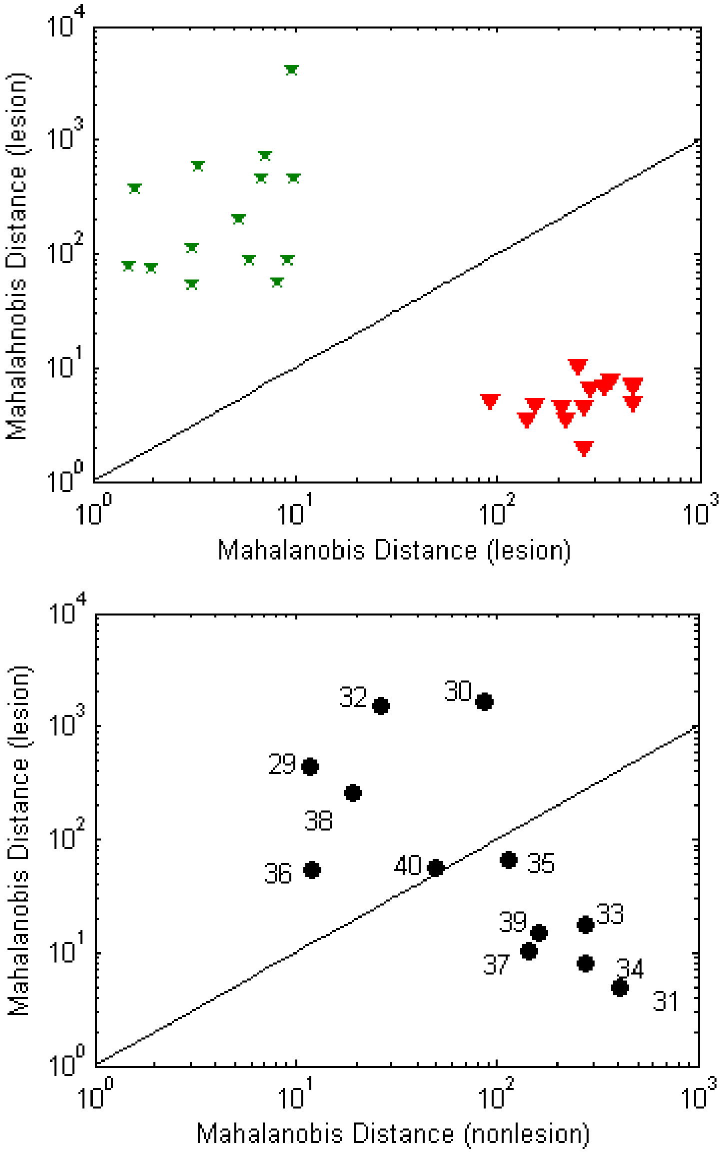

Figure 3.34: (top) Classification results of 28 training samples using the Mahalanobis Distance method and dehydrated data. Green stars – non-lesion training samples; red triangles – lesion training samples; Diagonal line – discriminant line. (bottom) Prediction results of 12 test samples based on the PLS-DA model for dehydrated data.

Alternatively, the application of principal components regression (PCR) techniques was investigated for hydrated and dehydrated data series of the test set to discriminate between lesion and non-lesion classes. '1' was the preset value for all lesion samples, and '0' for all non-lesion samples.[89] All spectra were again mean-centered prior to PCR. The predicted lesion value ideally centers at 0.5, and the non-lesion at -0.5. However, PCR based classification failed in accurately classifying hydrated data. **Figure 3.35** shows the PCR results using dehydrated data. A total of nine PCs were selected for the model, and all training samples could be accurately classified. Test sample 40 was incorrectly classified as non-lesion similar to PLS-DA and the Mahalanobis distance method. In addition, test sample 35 could not be clearly predicted with the horizontal zero line as discriminator, as the prediction value was only slightly above zero.

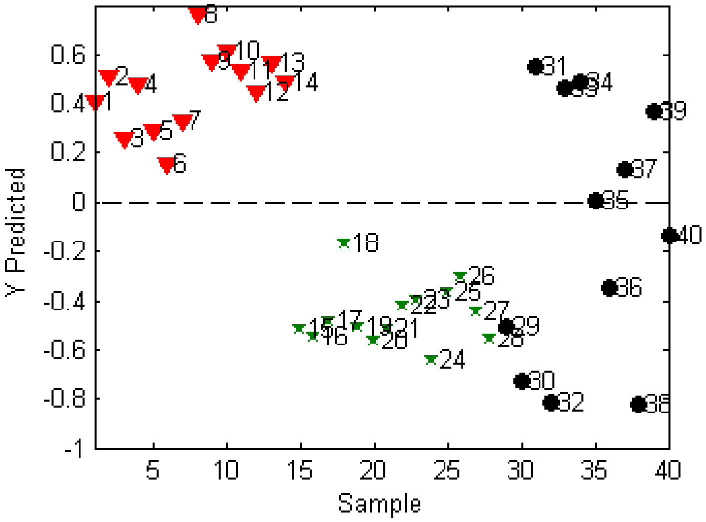

Figure 3.35: Classification and prediction results for PCR model with 9 PCs using dehydrated data. Red triangles – lesion training samples; green stars – non-lesion training samples; black dots – test samples.

In contrast to PCR, the PLS-DA method not only considers the changes in the spectra, but instantaneously also consider the changes in concentration of the various constituents (or class difference in our case). Due to uncertainties introduced by the sample preparation process and ambient effects during the measurements, the among-group difference is not always larger than the within-group difference. Hence, PCR appeared to be the least suitable method for providing satisfactory classification results.

The sensitivity and specificity of the PCA, PLS-DA, and Mahalanobis distance models for the training and test samples without *a prior* knowledge were calculated using the method introduced by Balchum *et al.*[89], and summarized in **Table 3.3**. The sensitivity measures the proportion of actual positives (diseased) which are correctly identified as such, and can be calculated by:

$$Sensitivity = \frac{TP}{TP + FN}$$

Eq. 3. 3

where *TP* represents the number of true positive identified, and *FN* the number of false negative identified.

The specificity measures the proportion of actual negatives (not diseased), which are correctly identified as such, and can be calculated by:

$$Selectivity = \frac{TN}{TN + FP}$$

Eq. 3. 4

where *TN* represents the number of true negative identified, and *FP* the number of false positive identified.

Table 3.3: Sensitivity and specificity of the investigated multivariate data analysis methods for training and test samples.

	Sensitivity, %				Specificity, %			
	6 LVs PLS-DA & M-distance		PCA		6 LVs PLS-DA & M-distance		PCA	
	Hy	Dehy	Hy	Dehy	Hy	Dehy	Hy	Dehy
Training samples	100	100	N/A	~100	100	100	N/A	~100
Test samples	100	85.7	N/A	~100	100	100	N/A	~100

*Hy – Hydrated samples; Dehy – Dehydrated samples.

That using hydrated data provides – marginally - more accurate and sensitive predictive results for PLS-DA and Mahalanobis distance in contrast to using dehydrated data, may result from the fact that the sample had significantly changed during ambient exposure, and during the experimental procedure; it has to be considered that the dehydrated data set was recorded after 11min of an entire measurement series. Hence, due to water evaporation the sample was significantly drier at the end compared to the beginning of the measurement series. In turn, this indicates that classification at hydrated conditions, which more closely resemble the *in vivo* environment, is more accurate by applying PLS-DA and Mahalanobis distance. However, PCA provided the opposite results with better discrimination at dehydrated vs. hydrated samples. PCA has failed to build appropriate classification models for hydrated samples. However, for test samples, it generated similar prediction results, as the other two multivariate data analysis strategies. In contrast to PCA, the PLS-DA method not only considers the changes in the spectra, but also instantaneously considers the changes in concentration of the various constituents (or class difference in our case). Due to the serious influence of water, the among-group difference with regards to the IR data vs. the contribution of all other biocomponents was relatively small for hydrated samples. The among-group difference was not always larger than the within-group difference. Hence, PCA appeared incapable of providing satisfactory classification results for hydrated samples. Only once aorta samples are dried, the among-group differences appear enhanced enabling PCA to correctly classify and predict aorta samples.

3.5.2.3 Multivariate Data Analysis Using Selected Spectral Ranges

In a final study, it was tested whether PCA and PLS-DA prediction accuracy improves by manually selecting specific spectral region(s), and by developing corresponding classification models. As described in the previous sections, C-H stretching of lipid locate in the region of ~3000-2800cm^{-1}, C=O stretching of lipid ester features at ~1800-1700cm^{-1}, and Amide I and II vibrations resulting from proteins located in the region ~1700-1600cm^{-1} are suitable spectral ranges. These regions are supposed to closely correlate to the chemical component change with the development of atherosclerotic plaque. PCA and PLS-DA calculations were performed separately at hydrated and dehydrated sample data using the combination of these three regions of the obtained spectra. The corresponding results for discriminating lesion and non-lesion samples are displayed in **Figure 3.36** and **Figure 3.37**. The accuracy, sensitivity, and specificity of the results obtained by the different multivariate data analysis methods for training and test samples were calculated and summarized in **Table 3.4**. From these results, it is evident that PCA

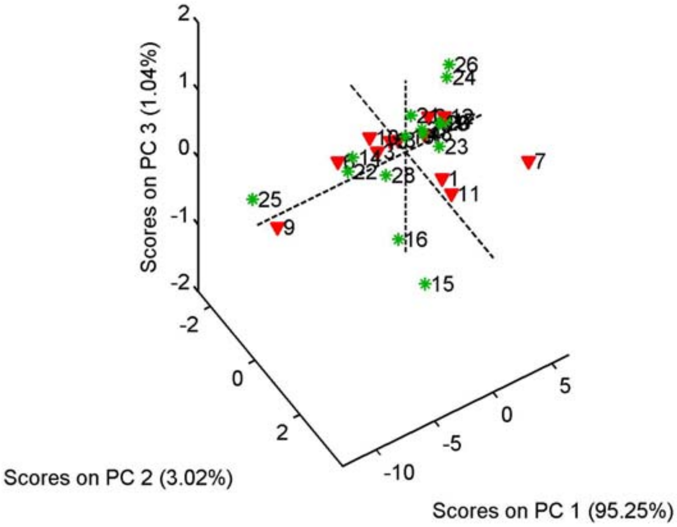

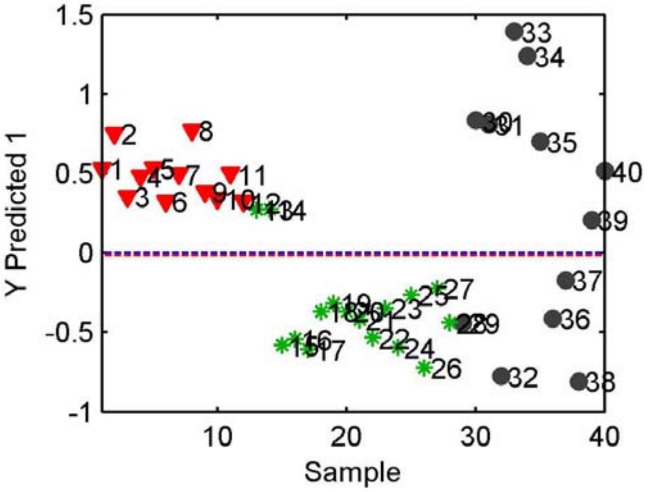

Figure 3.36: (top) PCA and (bottom) PLS-DA results for hydrated samples using the combined regions 3000-2700cm^{-1} and 1800-1600cm^{-1}. Green stars – non-lesion training samples; red triangles – lesion training samples; black dots – test samples; red line – threshold (-0.002).

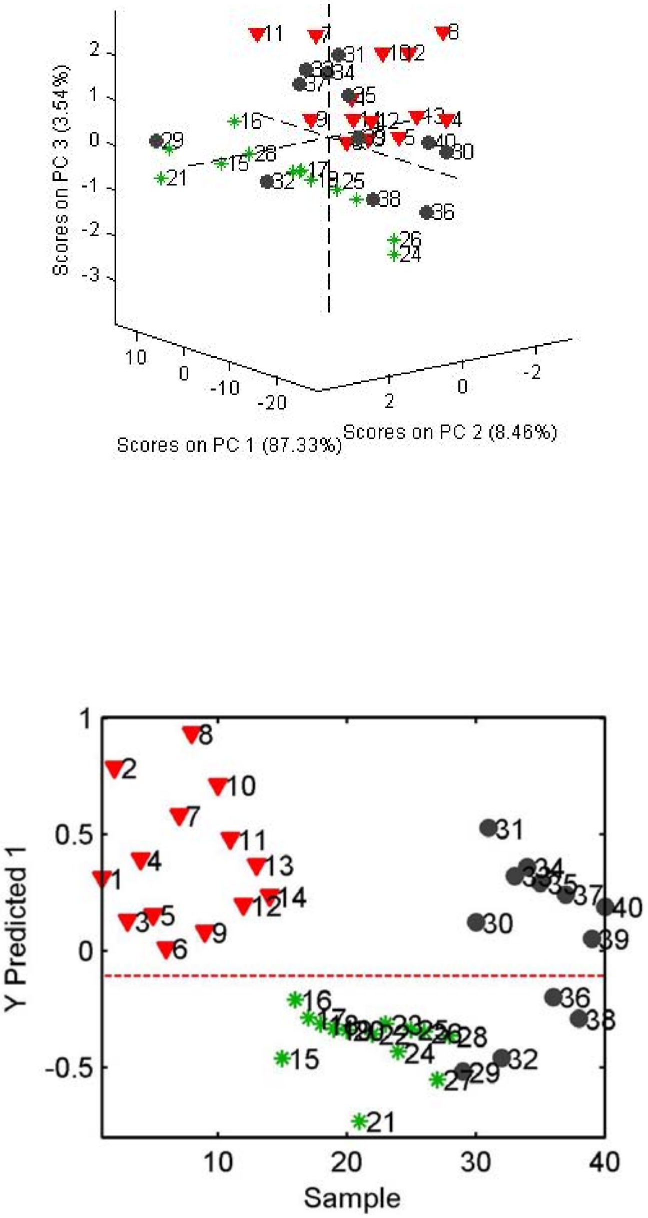

Figure 3.37: (top) PCA and (bottom) PLS-DA results for dehydrated samples using the combination of regions 3000-2700cm^{-1} and 1800-1600cm^{-1}. Green stars – non-lesion training samples; red triangles – lesion training samples; black dots – test samples; red line – threshold (-0.12).

Table 3.4: Accuracy, sensitivity, and specificity of the investigated multivariate data analysis methods for training and test samples using the spectral regions 3000-2700cm^{-1} and 1800-1600cm^{-1}.

	Accuracy, %				Sensitivity, %				Specificity, %			
	PLS-DA		PCA		PLS-DA		PCA		PLS-DA		PCA	
	Hy	Dehy	Hy	Dehy	Hy	Dehy	Hy	Dehy	Hy	Dehy	Hy	Dehy
Training samples	100	100	NA	100	100	100	NA	100	100	100	NA	100
Test samples	83.3	83.3	NA	91.7	80	80	NA	80	85.7	85.7	NA	100

*Hy – Hydrated sample; Dehy – dehydrated sample

still could not establish a viable calibration model for hydrated samples; using PLS-DA, a viable model was built but with reduced figures of merit. This may result from the fact that the selected spectral regions do not cover as much variance as the entire spectrum, thereby leading to reduced predictive capabilities.

PLS-DA calculations were also performed within the data region 3800-2700cm^{-1} (O-H stretching of water is dominant at ~3800-3000cm^{-1}) and 2100-1000cm^{-1}, respectively. The results in **Figure 3.38** and **Figure 3.39** show that the predictive capabilities were overall reduced compared to the results obtained using the entire spectral range (3800-1000cm-^{1}). In summary, it can be noted that for this specific case spectral region selection has not led to an improvement of the predictive capabilities of the established multivariate models.

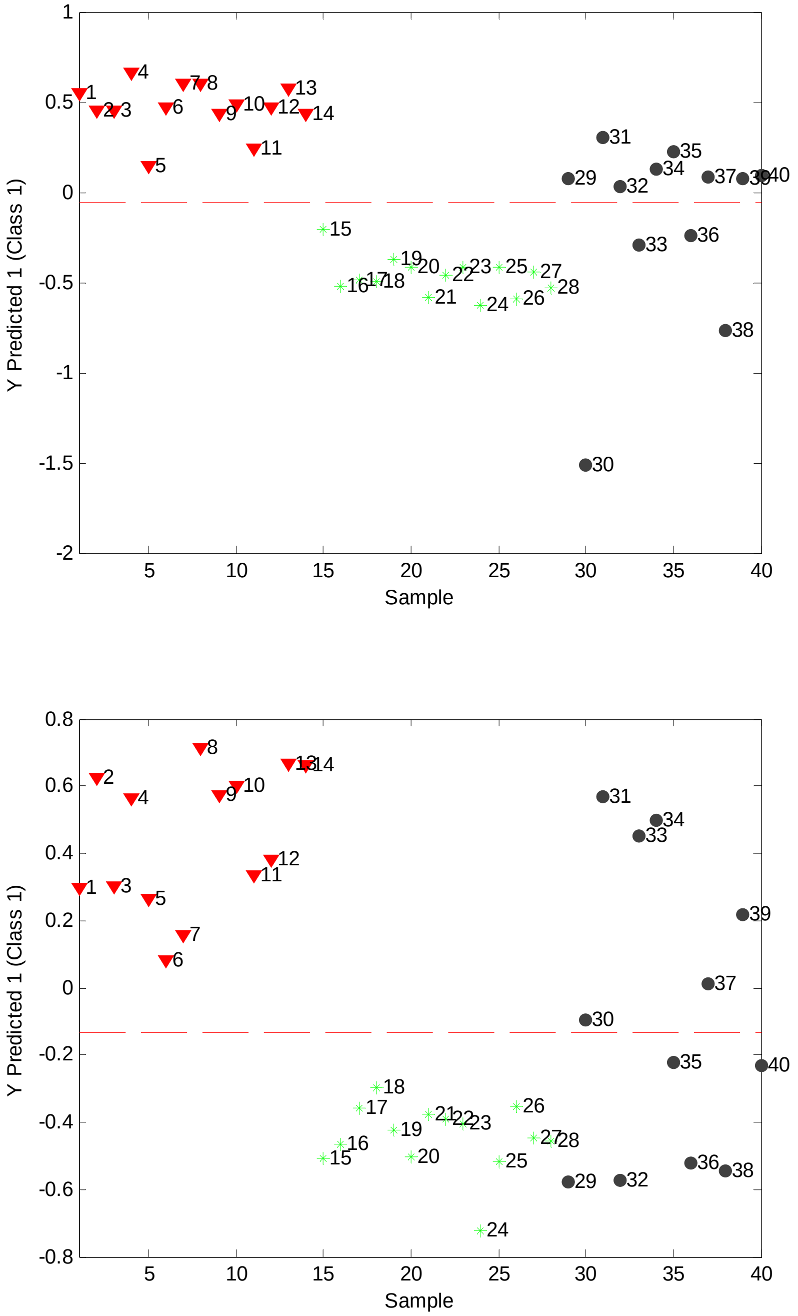

Figure 3.38: PLS-DA results for (top) hydrated and (bottom) dehydrated samples using the spectral region 3800-2700cm^{-1}.

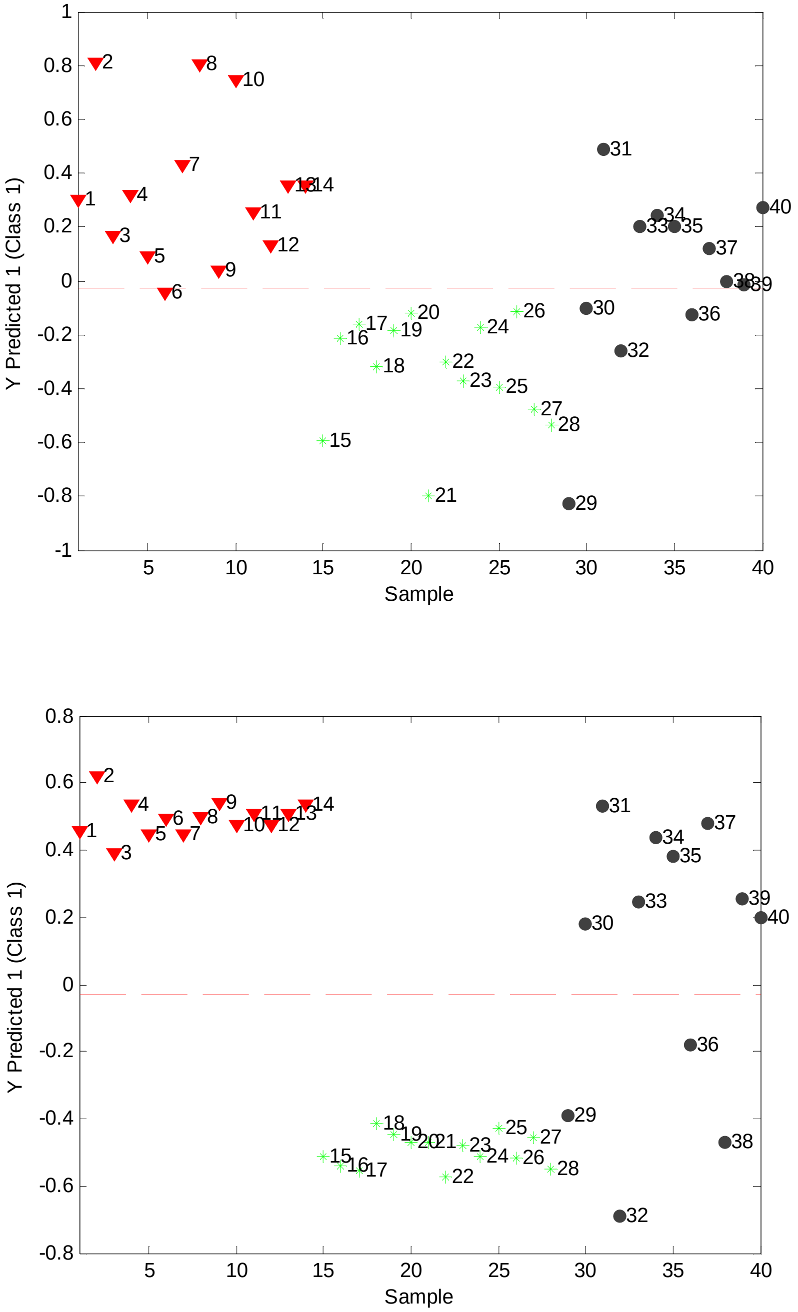

Figure 3.39: PLS-DA results for (top) hydrated and (bottom) dehydrated samples using the spectral region 2100-1000cm^{-1}.

3.5.3 *Bench-top IR-ATR Spectroscopy*

The average spectra for lesion samples and for non-lesion samples using single reflection ATR spectroscopy are shown in **Figure 3.40**. Spectral differences are most evident in the region 2700-3000cm^{-1}. However, spectra collected from individual dehydrated non-lesion samples also show relatively strong absorptions in the spectral region of 2700-3000cm^{-1}, and at approx. 1650cm^{-1}. These characteristics appear smoothed out in the average spectra, which may render the classification of these samples difficult, if these spectral features are used as the only identifiers. Therefore, multivariate data analysis appears again essential for obtaining reliable tissue classification models.

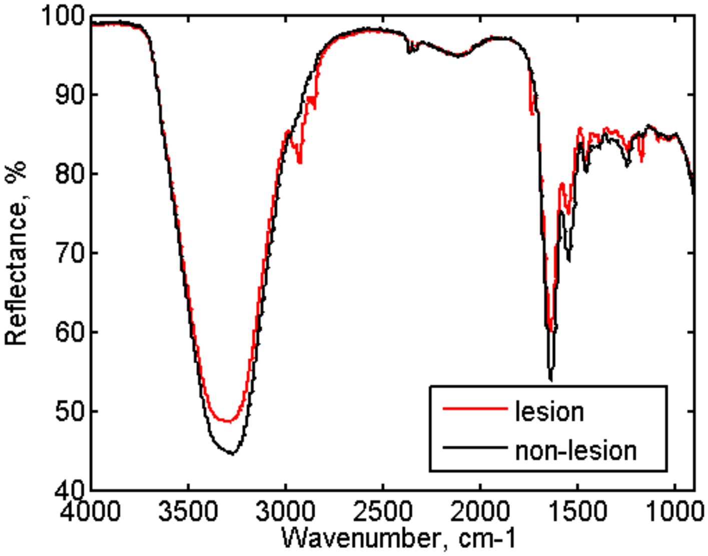

Figure 3.40: Red – average of dehydrated lesion sample spectra using IR-ATR; black – average spectrum of dehydrated non-lesion samples using IR-ATR.

PLS-DA was applied to IR-ATR data after preprocessing of the spectra by mean-centering. The corresponding classification results are shown in **Figure 3.41** (top). The prediction probability calculated using the Bayesian theorem is 1 for all tissue samples.

Alternatively, Mahalanobis distance was applied at the dehydrated tissue data collected using bench-top IR-ATR. The classification results based upon the latent variables derived from the PLS-DA are shown in **Figure 3.41** (bottom).

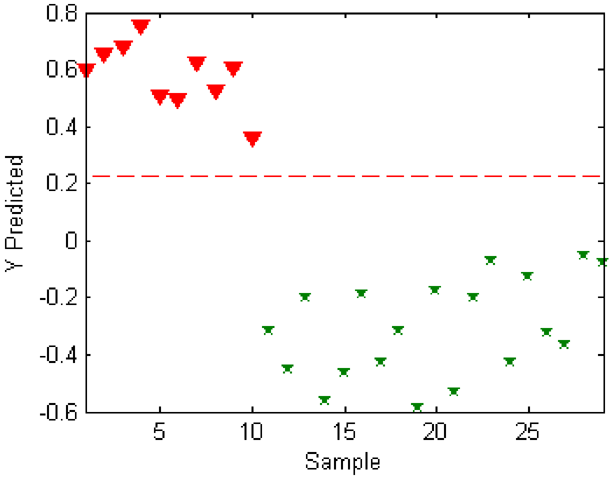

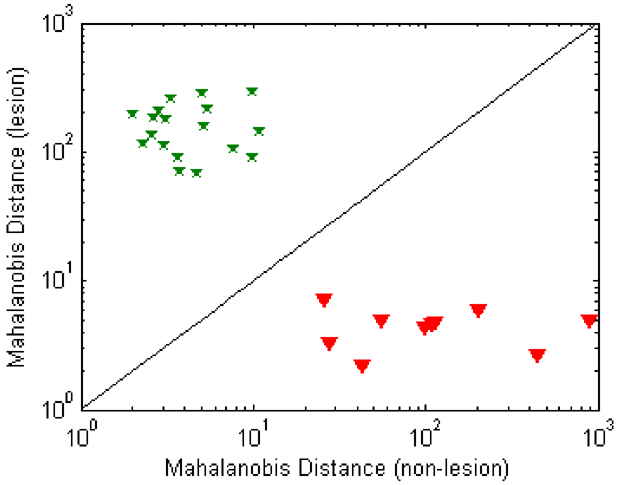

Figure 3.41: (top) Classification results for PLS-DA model applied to dehydrated data from bench-top IR-ATR. Red triangles – lesion samples; green stars – non-lesion samples; red line – threshold (0.2234). (bottom) Classification results of 29 dehydrated training samples measured using IR-ATR based on the Mahalanobis distance method. Green stars – non-lesion samples; red triangles – lesion samples; diagonal line – discriminant line.

Alternatively to building a model using all samples in the data set as training samples, the data were separated into a training set and a validation set. The validation set was used to test the robustness of the model established with the training set. This operation was performed 5 times, each time with a different set of 5 or 6 samples selected as validation data (2 lesion, and 3 or 4 non-lesion samples). The remaining 23 or 24 samples were used as training data. Eventually, each sample was selected into the validation data set once, and tested once. Five LVs were applied for all five calibration models, similar to the model using all data. All five models turned out to be sufficiently robust for predicting the corresponding validation samples with 100% hit quality.

3.6 Conclusions

Supervised multivariate data analysis methods based on PLS-DA and Mahalanobis distance were applied to mid-infrared micro-specular reflectance data, mid-infrared ATR data, and IR-ATR catheter prototype data obtained from lesion and non-lesion biopsy samples of rabbit aorta. Both methods achieved 100% hit quality with outstanding sensitivity and specificity during tests on small sets of double blinded samples, in particular for hydrated biopsy samples. Consequently, the results reveal a promising prospect for successful classification of lesion vs. non-lesion tissue samples based on IR spectra, in particular for IR-ATR catheter techniques in combination with multivariate data analysis and classification methods.

3.7 Outlook

3.7.1 Data Collection Using a Focal Plane Array (FPA) Imaging Microscope

Focal plane array (FPA) detectors usually consist of a two-dimensional matrix of individual detector elements located at the focal plane of a microscope imaging system. During future studies, a MIR FPA could be implemented to collect spectra of lesion and non-lesion rabbit aorta tissue spectra. By using a FPA, it is anticipated to significantly reduce the data collection time for the trainings data set, and to collect a wealth of data during a single measurement, thereby sufficiently capturing spatial variances of lesion and non-lesion tissue at the available samples in contrast to conventional one-element detection techniques.

3.7.2 Development of More Robust Multivariate Classification Models

The developed supervised and unsupervised multivariate data analysis methods need to be significantly expanded using more aorta samples from additional rabbits. Thus, more robust models can be built for further improving the prediction for unknown samples, even capturing the variance across multiple species. Furthermore, it should be investigated whether calibration models derived from FPA imaging microscopy in the ATR mode may be applied to the classification of samples analyzed using a two-waveguide or three-waveguide IR-ATR catheter. Thereby, rapid establishment of multivariate models would be enabled, while transferability of the established classification to data obtained from a catheter device will be used to collect the real-world samples.

3.7.3 Integration of a Three-Waveguide Catheter

According to the scheme shown in Figure 10, a three-waveguide catheter can be envisaged using e.g., a photonic band gap (PBG) hollow waveguide for simultaneously delivering FEL or CO_2 laser radiation to the interface between the ATR element and the tissue surface for tissue ablation, while two additional conventional HWGs could serve as delivery and collection waveguides for broadband IR radiation coupled from a FT-IR spectrometer for simultaneous spectroscopic tissue characterization. With three waveguides connected to a cylindrical ZnSe ATR tip direct spectroscopic control during laser surgery would be enabled.

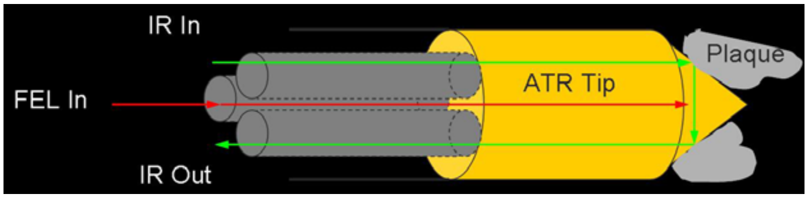

Figure 3.42: Schematic construction of a three-HWG IR-ATR catheter for simultaneous IR detection and surgical laser ablation.

Ideally, normal and atherosclerotic lesion rabbit aorta samples would be examined with the developed three-waveguide IR-ATR catheter, and evaluated/classified via an adapted multivariate calibration model derived from FPA imaging ATR microscopy. The classification results would be used for on-line guiding of laser ablation at tissues with immediate feedback to determine successful ablation (i.e., reaching the blood vessel wall after successful removal of the entire plaque), which could lead to automatic switch-off for the surgical laser. Upon success, it may be anticipated that this measurement concept would be transferred from *in vitro* trials to *in vivo* trials with appropriate animal models.

3.8 References

(1) Hooper, B. A.; LaVerde, G. C.; von Ramm, O. T. *Design and construction of an evanescent optical wave device for the recanalization of vessels*, Nucl. Instru. Meth. Phys. Res. **2001**, *A475*.

(2) Hooper, B. A.; Maheshwari, A.; Curry, A. C.; Alter, T. M. *Catheter for diagnosis and therapy with infrared evanescent waves*, Appl. Opt. **2003**, *42*, 3205-3214.

(3) Wang, L.; Mizaikoff, B. *Application of multivariate data-analysis techniques to biomedical diagnostics based on mid-infrared spectroscopy*, Anal. Bioanal. Chem. **2008**, *391*, 1641-1654.

(4) Afanasyeva, N. I.; Bruch, R. F.; Katzir, A. *Infrared fiber optic evanescent wave spectroscopy: applications in biology and medicine*, Proc. SPIE-Int. Soc. Opt. Eng. **1999**, *3596*, 152-164.

(5) Baraga, J. J.; Feld Michael, S.; Rava, R. P. *Detection of atherosclerosis in human artery by mid-infrared attenuated total reflectance*, Appl. Opt. **1991**, *45*, 709-711.

(6) Bindig, U.; Gersonde, I.; Meinke, M.; Becker, Y.; Mueller, G. *Fibre-optic IR-spectroscopy for biomedical diagnostics*, Spectroscopy **2003**, *17*, 323-344.

(7) Eytan, O.; Sela, B.-A.; Katzir, A. *Fiber-optic evanescent-wave spectroscopy and neural networks: Application to chemical blood analysis*, Appl. Opt. **2000**, *39*, 3357-3360.

(8) Fabian, H.; Lasch, P.; Naumann, D. *Analysis of biofluids in aqueous environment based on mid-infrared spectroscopy*, J. Biomed. Opt. **2005**, *10*, 031103/031101-031103/031110.

(9) Gotshal, Y.; Adam, I.; Katzir, A. *Glucose measurements in solutions using fiberoptic evanescent wave spectroscopy and tunable CO2 laser*, Proc. SPIE-Int. Soc. Opt. Eng. **1998**, *3262*, 192-196.

(10) Heise, H. M.; Bittner, A.; Kupper, L.; Butvina, L. N. *Comparison of evanescent wave spectroscopy based on silver halide fibers with conventional ATR-IR spectroscopy*, J. Mol. Struct. **1997**, *410-411*, 521-525.

(11) Heise, H. M.; Kupper, L.; Butvina, L. N. *Attenuated total reflection mid-infrared spectroscopy for clinical chemistry applications using silver halide fibers*, Sens. Actuators **1998**, *B51*, 84-91.

(12) Heise, H. M.; Kupper, L.; Butvina, L. N. *Bio-analytical applications of mid-infrared spectroscopy using silver halide fiber-optic probes*, Spectrochim. Acta **2002**, *57B*, 1649-1663.

(13) Heise, H. M.; Marbach, R.; Janatsch, G.; Kruse-Jarres, J. D. *Multivariate determination of glucose in whole blood by attenuated total reflection infrared spectroscopy*, Anal. Chem. **1989**, *61*, 2009-2015.

(14) Heise, H. M.; Voigt, G.; Lampen, P.; Kupper, L.; Rudloff, S.; Werner, G. *Multivariate calibration for the determination of analytes in urine using mid-infrared attenuated total reflection spectroscopy*, Appl. Spectrosc. **2001**, *55*, 434-443.

(15) Janatsch, G.; Kruse-Jarres, J. D.; Marbach, R.; Heise, H. M. *Multivariate calibration for assays in clinical chemistry using attenuated total reflection infrared spectra of human blood plasma*, Anal. Chem. **1989**, *61*, 2016-2023.

(16) Lambrecht, A.; Beyer, T.; Hebestreit, K.; Mischler, R.; Petrich, W. *Continuous glucose monitoring by means of fiber-based, mid-infrared laser spectroscopy*, Appl. Spectrosc. **2006**, *60*, 729-736.

(17) Mordechai, S.; Sahu, R. K.; Hammody, Z.; Mark, S.; Kantarovich, K.; Guterman, H.; Podshyvalov, A.; Goldstein, J.; Argov, S. *Possible common biomarkers from FTIR microspectroscopy of cervical cancer and melanoma*, J. Microsc. **2004**, *215*, 86-91.

(18) Sahu, R. K.; Argov, S.; Salman, A.; Huleihel, M.; Grossman, N.; Hammody, Z.; Kapelushnik, J.; Mordechai, S. *Characteristic absorbance of nucleic acids in the mid-IR region as possible common biomarkers for diagnosis of malignancy*, Technol. Cancer Res. Treat. **2003**, *3*, 629-638.

(19) Wang, J.; Sowa, M.; Mantsch, H. H.; Bittner, A.; Heise, H. M. *Comparison of different infrared measurement techniques in the clinical analysis of biofluids*, TrAC, Trends Anal. Chem. **1996**, *15*, 286-296.

(20) Li, C.; Ebenstein, D.; Xu, C.; Chapman, J.; Saloner, D.; Rapp, J.; Pruitt, L. *Biochemical characterization of atherosclerotic plaque constituents using FTIR spectroscopy and histology*, J. Biomed. Mater. Res. **2003**, *64A*, 197-206.

(21) Baraga, J. J.; Feld, M. S.; Rava, R. P. *Detection of atherosclerosis in human artery by mid-infrared attenuated total reflectance*, Appl. Spectrosc. FIELD Full Journal Title:Applied Spectroscopy **1991**, *45*, 709-711.

(22) Colley, C. S.; Kazarian, S. G.; Weinberg, P. D.; Lever, M. J. *Spectroscopic imaging of arteries and atherosclerotic plaques*, Biopolymers **2004**, *74*, 328-335.

(23) Manoharan, R.; Baraga, J. J.; Rava, R. P.; Dasari Ramachandra, R.; Fitzmaurice, M.; Feld Michael, S. *Biochemical analysis and mapping of atherosclerotic human artery using FT-IR microspectroscopy*, Atherosclerosis **1993**, *103*, 181-193.

(24) Wang, L.; Chapman, J.; Palmer, R. A.; Alter, T. M.; Hooper, B. A.; van Ramm, O.; Mizaikoff, B. *Classification of atherosclerotic rabbit aorta samples with an infrared attenuated total reflection catheter and multivariate data analysis*, Appl. Spectrosc. **2006**, *60*, 1121-1126.

(25) Wang, L.; Chapman, J.; Palmer Richard, A.; van Ramm, O.; Mizaikoff, B. *Classification of atherosclerotic rabbit aorta samples by mid-infrared spectroscopy using multivariate data analysis*, J. Biomed. Opt. **2007**, *12*, 024006.

(26) Alam, M.; Timlin, J.; Martin, L.; Williams, D.; Lyons, C.; Garrison, K.; Hjelle, B. *Spectroscopic evaluation of living murine macrophage cells before and after activation using attenuated total reflectance infrared spectroscopy*, Vib. Spectrosc. **2004**, *34*, 3-11.

(27) Gazi, E.; Dwyer, J.; Gardner, P.; Ghanbari-Siahkali, A.; Wade, A.; Miyan, J.; Lockyer, N.; Vickerman, J.; Clarke, N.; Shanks, J.; Scott, L.; Hart, C.; Brown, M. *Applications of Fourier transform infrared microspectroscopy in studies of benign prostate and prostate cancer. A pilot study*, J. Pathol. **2003**, *201*, 99-108.

(28) Kim, S.; Reuhs, B.; Mauer, L. *Use of fourier transform infrared spectra of crude bacterial lipopolysaccharides and chemometrics for differentiation of Salmonella enterica serotypes*, J. Appl. Microbiol. **2005**, *99*, 411-417.

(29) Krafft, C.; Sobottka, S.; Schackert, G.; Salzer, R. *Analysis of human brain tissue, brain tumors and tumor cells by infrared spectroscopic mapping*, Analyst **2004**, *129*, 921-925.

(30) Lasch, P.; Haensch, W.; Lewis, E.; Kidder, L.; Naumann, D. *Characterization of colorectal adenocarcinoma sections by spatially resolved FT-IR microspectroscopy*, Appl. Spectrosc. **2002**, *56*, 1-9.

(31) McIntosh, C. L.; Jackson, M.; Mantsch, H.; Stranc, M.; Pilavdzic, D.; Crowson, A. *Infrared spectra of basal cell carcinomas are distinct from non-tumor-bearing skin components*, J Invest. Dermatol. **1999**, *112*, 951-956.

(32) Mossoba, M.; Khambaty, F.; Fry, F. *Novel application of a disposable optical film to the analysis of bacterial strains: a chemometric classification of mid-infrared spectra*, Appl. Spectrosc. **2002**, *56*, 732-736.

(33) Mourant, J.; Short, K.; Carpenter, S.; Kunapareddy, N.; Cobum, L.; Powers, T.; Tamara, M.; Freyer, J. *Biochemical differences in tumorigenic and nontumorigenic cells measured by Raman and infrared spectroscopy*, J. Biomed. Opt. **2005**, *10*, 031106/031101-031106/031115.

(34) Nilson, M.; Heinrich, D.; Olajos, J.; Andersson-Engels, S. *Near infrared diffuse reflection and laser-induced fluorescence spectroscopy for myocardial tissue characterization*, Spectrochim. Acta **1997**, *51A*, 1901-1912.

(35) Schultz, C.; Mantsch, H. *Biochemical imaging and 2D classification of keratin pearl structures in oral squamous cell carcinoma*, Cell. Mol. Biol. Lett. **1998**, *44*, 203-210.

(36) Stehfest, K.; Toepel, J.; Wihelm, C. *The application of micro-FTIR spectroscopy to analyze nutrient stress-related changes in biomass composition of phytoplankton algae*, Plant Physiol. Biol. **2005**, *43*, 717-726.

(37) Steiner, G.; Shaw, A.; Choo-Smith, L. P.; Abuid, M.; Schackert, G.; Sobottka, S.; Steller, W.; Sazlzer, R.; Mantsch, H. *Distinguishing and grading human gliomas by IR spectroscopy*, Biopolymers **2003**, *72*, 464-471.

(38) Buschman, H. P.; Motz, J. T.; Deinum, G.; Romer, T. J.; Fitzmaurice, M.; Kramer, J. R.; van der Laarse, A.; Bruschke, A. V.; Feld, M. S. *Diagnosis of*

human coronary atherosclerosis by morphology-based Raman spectroscopy, Cardiovasc. pathol. **2001**, *10*, 59-68.

(39) Anastassopoulou, N.; Arapoglou, B.; Demakakos, P.; Makropoulou, M.; Paphiti, A.; Serafetinides, A. *Spectroscopic characterisation of carotid atherosclerotic plaque by laser induced fluorescence*, Lasers Surg. Med. **2002**, *28*, 67-73.

(40) Andersson-Engels, S.; Johannson, J.; Svanberg, S. *The use of time-resolved fluorescence for diagnosis of atherosclerotic plaque and malignant tumors*, Spectroch. Acta **1990**, *46A*, 1203-1210.

(41) Andersson-Engels, S.; Johansson, J.; Stenram, U.; Svanberg, K.; Svanberg, S. *Time-resolved laser-induced fluorescence spectroscopy for enhanced demarcation of human atherosclerotic plaques*, Photochem. Photobiol. B **1990**, *4*, 363-369.

(42) Baraga, J. J.; Rava, R. P.; Taroni, P.; Kittrell, C.; Fitzmaurice, M.; Feld, M. S. *Laser induced fluorescence spectroscopy of normal and atherosclerotic human aorta using 306-310 nm excitation*, Lasers Surg. Med. **1990**, *10*, 245-261.

(43) Clarke, R. H.; Isner, J. M.; Gauthier, T.; Nakagawa, K.; Cerio, F.; Hanion, E.; Gaffney, E. J.; Rouse, E.; Dejesus, S. *Spectroscopic characterization of cardiovascular tissue*, Lasers Surg.Med. **1988**, *8*, 45-59.

(44) Deckelbaum, L. I.; Lam, J. K.; Cabin, H. S.; Clubb, K. S.; Long, M. B. *Discrimination of normal and atherosclerotic aorta by laser-induced fluorescence*, Lasers Surg. Med. **1987**, *7*, 330-335.

(45) Deckelbaum, L. I.; Stetz, M. L.; O'Brien, K. M.; Cutruzzola, F. W.; Gmitro, A. F.; Laifer, L. I.; Gindi, G. R. *Fluorescence spectroscopy guidance of laser ablation of atherosclerotic plague*, Lasers Surg. Med. **1989**, *9*, 205-214.

(46) Fang, Q.; Papaioannou, T.; Jo, J. A.; Vaitha, R.; Shastry, K.; Marcu, L. *Time-domain laser-induced fluorescence spectroscopy apparatus for clinical diagnostics*, Rev. Sci. Instru. **2004**, *75*, 151-162.

(47) Laifer, L. I.; O'Brien, K. M.; Stetz, M. L.; Gindi, G. R.; Garrand, T. J.; Deckelbaum, L. I. *Biochemical basis for the difference between normal and atherosclerotic arterial fluorescence*, Circulation **1989**, *80*, 1893-1901.

(48) Leon, M. B.; Lu, D. Y.; Prevosti, L. G.; Macy, W. W., Jr.; Smith, P. D.; Granovsky, M.; Bonner, R. F.; Balaban, R. S. *Human arterial surface fluorescence: atherosclerotic plaque identification and effects of laser atheroma ablation*, J. Am. Coll. Cardiol. **1988**, *12*, 94-102.

(49) Marcu, L.; Fishbein, M. C.; Maarek, J.-M. I.; Grundfest, W. S. *Discrimination of Human Coronary Artery Atherosclerotic Lipid-Rich Lesions by Time-Resolved Laser-Induced Fluorescence Spectroscopy*, Arteriosclerosis, thrombosis, and vascular biology **2001**, *21*, 1244-1250.

(50) Murphy-Chutorian, D.; Kosek, J.; Mok, W.; Quay, S.; Huestis, W.; Mehigan, J.; Profitt, D.; Ginsburg, R. *Selective absorption of ultraviolet laser energy by human atherosclerotic plaque treated with tetracycline*, Am. J. Cardiol. **1985**, *55*, 1293-1297.

(51) Papazoglou, T. G. *Malignancies and atherosclerotic plaque diagnosis-is laser induced fluorescence spectroscopy the ultimate solution?*, J. Photochem. Photobiol., B **1995**, *28*, 3-11.

(52) Zhu, B.; Jaffer, F. A.; Ntziachristos, V.; Weissleder, R. *Development of a near infrared fluorescence catheter: Operating characteristics and feasibility for atherosclerotic plaque detection*, J. Phys. D **2005**, *38*, 2701-2707.

(53) Marcu, L.; Fang, Q.; Jo, J. A.; Papaioannou, T.; Dorafshar, A.; Reil, T.; Qiao, J.-H.; Baker, J. D.; Freischlag, J. A.; Fishbein, M. C. *In vivo detection of macrophages in a rabbit atherosclerotic model by time-resolved laser-induced fluorescence spectroscopy*, Atherosclerosis **2005**, *181*, 295-303.

(54) Christov, A.; Dai, E.; Drangova, M.; Liu, L.; Abela, G. S.; Nash, P.; McFadden, G.; Lucas, A. *Optical detection of triggered atherosclerotic plaque disruption by fluorescence emission analysis*, Photochem. Photobiol. **2000**, *72*, 242-252.

(55) Christov, A.; Korol, R. M.; Dai, E.; Liu, L.; Guan, H.; Bernards, M. A.; Cavers, P. B.; Susko, D.; Lucas, A. *In Vivo Optical analysis of Quantitative changes in collagen and elastin during arterial remodeling*, Photochem. Photobiol. **2005**, *81*, 457-466.

(56) Baraga, J. J.; Feld Michael, S.; Rava, R. P. *Rapid near-infrared Raman spectroscopy of human tissue with a spectrograph and CCD detector*, Appl. Spectrosc. Rev. **1992**, *46*, 187-190.

(57) Baraga, J. J.; Feld, M. S.; Rava, R. P. *In situ optical histochemistry of human artery using near infrared Fourier transform Raman spectroscopy*, Proc. Nat. Aca. Sci. USA **1992**, *89*, 3473-3477.

(58) Brennan, J. F.; Römer, T. J.; Lees, R. S.; Tercvak, A. M.; Kramer, J. R.; Feld Michael, S. *Determination of human coronary artery composition by Raman spectroscopy*, Circulation **1997**, *96*, 99-105.

(59) Buschman, H. P.; Marple, E. T.; Wach, M. L.; Bennett, B.; Bakker Schut, T. C.; Bruining, H. A.; Bruschke, A. V.; van der Laarse, A.; Puppels, G. J. *In Vivo Determination of the Molecular Composition of Artery Wall by Intravascular Raman Spectroscopy*, Anal. Chem. **2000**, *72*, 3771-3775.

(60) Cacheux, P. L.; Ménard, G.; Quaang, H. N.; Dao, N. Q.; Roach, A. G. *Quantitative determination fof free and esterified cholesterol concentrations in cholesterol-fed rabbit aorta using near-infrared Fourier transform-Raman spectroscopy*, Spetrochim. Acta **1996**, *52A*, 1619-1627.

(61) Denium, G.; Rodriguez, D.; Römer, T. J.; Fizmaurice, M.; Kramer John, R.; Feld Michael, S. *Histological classification of Raman spectra of human coromary artery atherosclerosis using principal component analysis*, Appl. Spectrosc. **1998**, *53*, 938-942.

(62) Manoharan, R.; Baraga, J. J.; Feld Michael, S.; Rava, R. P. *Quantitative histochemical analysis of human artery using Raman spectroscopy*, J. Photochem. Photobiol. B **1992**, *16*, 211-233.

(63) Rava, R. P.; Baraga, J. J.; Feld Michael, S. *near infrared Fourier transform Raman spectroscopy of human artery*, Spectrochim. Acta **1991**, *47A*, 509-512.

(64) Van de Poll, S. W. E.; Kastelijn, K.; Schut, T. C. B.; Strijder, C.; Pasterkamp, G.; Puppels, G. J.; Van der Laarse, A. *On-line detection of cholesterol and calcification by catheter based Raman spectroscopy in human atherosclerotic plaque ex vivo*, Heart **2003**, *89*, 1078-1082.

(65) Weinmann, P.; Jouan, M.; Nguyen, Q. D.; Lacroix, B.; Groiselle, C.; Bonte, J. P.; Luc, G. *Quantitative analysis of cholesterol and cholesteryl esters in human atherosclerotic plaques using near-infrared Raman spectroscopy*, Atherosclerosis **1998**, *140*, 81-88.

(66) Motz Jason, T.; Fitzmaurice, M.; Miller, A.; Gandhi Saumil, J.; Haka Abigail, S.; Galindo Luis, H.; Dasari Ramachandra, R.; Kramer John, R.; Feld Michael, S. *In vivo Raman spectral pathology of human atherosclerosis and vulnerable plaque*, J. Biomed. Opt. **2006**, *11*, 021003.

(67) Jaross, W.; Neumeister, V.; Lattke, P.; Schuh, D. *Determination of cholesterol in atherosclerotic plaques using near infrared diffuse reflection spectroscopy*, Atherosclerosis **1999**, *147*, 327-337.

(68) Lodder, R. A.; Cassis, L. A.; Ciurczak, E. W. *Artery analysis with a novel near-IR fiber-optic probe*, Spectroscopy **1990**, *5*, 12-17.

(69) Wang, J.; Geng, Y.; Guo, B.; Klim, T.; Lal, B. N.; Willerson, J. T.; Casscells, W. *Near-infrared spectroscopic characterization of human advanced atherosclerotic plaques*, J. Am. Coll. Cardiol **2002**, *39*, 1305-1313.

(70) Arai, T.; Mlzuno, K.; Fujikawa, A.; Makagawa, M.; Kikuchl, M. *Infrared absorption spectra ranging from 2.5 to 10 μm at various layers of human normal abdominal aorta and Fibrofatty atheroma in vitro*, Lasers Surg. Med. **1990**, *10*, 3561.

(71) Sartori, M.; Weilbaecher, D.; Valderrama, G. L.; Kubodera, S.; Chin, R. C.; Berry, M. J.; Tittel, F. K.; Sauerbrey, R.; Henry, P. D. *Laser-induced autofluorescence of human arteries*, Circ. Res. **1988**, *63*, 1053-1059.

(72) van de Poll Sweder, W. E.; Romer Tjeerd, J.; Puppels Gerwin, J.; van der Laarse, A. *Imaging of atherosclerosis. Raman spectroscopy of atherosclerosis*, J. Cardiovascul. Risk **2002**, *9*, 255-261.

(73) Cassis, L. A.; Lodder, R. A. *Near-IR imaging of atheromas in living artery tissue*, Anal. Chem. **1993**, *65*, 1247-1256.

(74) Alo, F.; Bruni, P.; Cavalleri, A.; Conti, C.; Giorgini, E.; Rubini, C.; Tosi, G. *Infrared microscopy characterization of carotid plaques and thyroid tissue biopsies*, J. Mol. Struct. **2003**, *651-653*, 419-426.

(75) Runge, M. S.; Patterson, C.; Willerson, J. T. *Principles of Molecular Cardiology*, 2005.

(76) Miller, J. C.; Miller, J. N. *Statistics and Chemometrics for Analytical Chemistry, 4th Edition*, 2000.

(77) Otto, M. *Chemometrics: Statistics and Computer Application in Analytical Chemistry*, 1998.

(78) Beebe, K. R.; Pell, R. J.; Seasholtz, M. B. *Chemometrics: A Practical Guide*, 1998.

(79) Kramer, R. *Basic Chemometrics: A Practical Introduction to Quantitative Analysis*, 1995.

(80) Haaland, D. M.; Jones, H. D. T.; Thomas, E. V. *Multivariate classification of the infrared spectra of cell and tissue samples*, Applied Spectroscopy **1997**, *51*, 340-345.

(81) Barker, M.; Rayens, W. *Partial least squares for discrimination*, Journal of Chemometrics **1993**, *17*, 166-173.

(82) Mark, H. L. *Normalized distance for qualitative near-infrared reflectance analysis*, Anal. Chem. **1986**, *58*, 379-384.

(83) Mark, H. L.; Tunnell, D. *Qualitative near-infrared reflectance analysis using mahalanobis distance*, Anal. Chem. **1985**, *57*, 1449-1456.

(84) Dabahoglu, I. *A quantitative study of the aorta of the New Zealand Rabbit (Oryctolagus cuniculus L.)*, Anatomia, histologia, embryologia **2000**, *29*, 145-147.

(85) Miyagi, M.; Harada, K.; Aizawa, Y.; Kawakami, S. *Transmission properties of circular dielectric-coated metallic waveguides for infrared transmission*, Proc. SPIE-Int. Soc. Opt. Eng. **1984**, *484*, 117-123.

(86) Bindig, U.; Meinke, M.; Gersonde, I. H.; Kravchik, S.; Citron, S.; Katzir, A.; Mueller, G. J. *Detection of malignant tissues by using infrared microscopy and fiber optic spectroscopy*, Proc. SPIE-Int. Soc. Opt. Eng. **2001**, *4253*, 108-117.

(87) Bindig, U.; Meinke, M.; Gersonde, I.; Spector, O.; Vasserman, I.; Katzir, A.; Muller, G. *IR-biosensor: flat silver halide fiber for bio-medical sensing?*, Sens. Actuators, B **2001**, *B74*, 37-46.

(88) Beleites, C.; Baumgartner, R.; Bowman, C.; Somorjai, R.; Steiner, G.; Salzer, R.; Sowa, M. G. *Variance reduction in estimating classification error using sparse datasets*, Chemom. Intell. Lab. Syst. **2005**, *79*, 91-100.

(89) Haaland, D. M.; Jones, H. D. T.; Thomas, E. V. *Multivariate classification of the infrared spectra of cell and tissue samples*, Appl. Spectrosc. **1997**, *51*, 340-345.

CHAPTER 4

COMBINATION OF SCANNING ELECTROCHEMICAL MICROSCOPY WITH INFRARED ATTENUATED TOTAL REFLECTION SPECTROSCOPY FOR *IN SITU* INVESTIGATION OF ELECTROCHEMICALLY INDUCED PROCESSES

In this chapter, the first reported combination of scanning electrochemical microscopy with infrared attenuated total reflection spectroscopy (SECM-IR-ATR) is presented. The analytical capabilities of the combined microelectrochemical-FT-IR setup were demonstrated by simultaneously *in situ* investigation of a micro-structured polymer (poly (2,5-di-(2-thienyl)-pyrrole) deposition *via* evanescent field absorption, which was induced via feedback mode SECM using a 25 µm Pt disk ultramicroelectrode (UME). In addition, spectral ray tracing simulation on the optical part of the combined SECM-IR-ATR instrument was performed for evaluating the IR sensitive area on the ATR crystal surface. Furthermore, line-scans were performed for experimentally investigating the sensitive area of the ATR crystal surface by monitoring the IR absorption change resulting from the UME sheath material when moving the UME tip within the evanescent field along cross-sections of the ATR crystal.

4.1 Motivation

Recent research of our group has demonstrated that IR-ATR combined with atomic force microcopy (AFM) can simultaneously monitor spectroscopic and topographic changes at the ATR crystal surface in liquid environments.[1] There is an opportunity to further extend this dual combination *via* coupling to SECM by using AFM-SECM scanning probe tips.[2, 3] The potential triple combination AFM-SECM-IR-ATR will enable obtaining simultaneous *in situ* topographic (AFM), spectroscopic (IR-ATR), and electrochemical (SECM) information, which is of particular interest when studying frequently changing dynamic systems and matrices such as biological samples. However, there is still a question that needs to be answered prior to achieving the triple combination: **is it possible to combine SECM with IR-ATR**?

4.2 Introduction

The systematic analysis of processes at the solid/liquid interface requires experimental tools and analytical methods to qualitatively and quantitatively determine and image interfacial events with molecular selectivity, sensitivity, and preferably temporal/spatial resolution. Many conventional analytical techniques are frequently limited to averaged measurements or *ex situ* analysis. Hence the combination of complementary *in situ* analytical techniques with scanning probe microscopic (SPM) techniques might bridge the gap to elucidate fundamental processes at the solid/liquid interface.

Among the scanning probe techniques, SECM has matured into a versatile *in situ* method providing information on homogeneous and heterogeneous electron transfer mechanisms at various solid/liquid, liquid/liquid, and air/liquid interfaces.[4, 5] In addition, SECM has successfully been used for microstructured surface modifications using electrochemically assisted deposition or etching processes.[6] Either direct mode SECM experiments using the UME as auxiliary electrode and the biased sample as working electrode, or feedback mode SECM experiments at conductive and insulating surfaces have been described in literatures.[7-29] First approaches using direct mode SECM were based on applying a bias between an electrochemical scanning tunneling microscopy (STM) tip and a conductive surface, which was covered with a thin polymer film such as Nafion[7-9] The localized current flow between tip and sample was instrumental in reducing or oxidizing metal ions or organic ions incorporated in film-forming metal lines or polymer lines. Direct mode deposition of 2- and 3-dimensional polymer structures using pulsed deposition profiles has also been achieved using disk-shaped microelectrodes as auxiliary electrodes.[11-13] Structured self-assembled layers and fluorescent patterns could be generated in direct mode SECM.[24, 30] The close distance between tip and sample surface, as well as the tip size and tip geometry govern the dimensions of the obtained microstructures by defining the electrical field distribution between tip and conductive sample. Alternatively, modifications can be achieved in feedback mode SECM generating an electroactive species at the UME, which is diffusing to the sample surface, and then driving the surface modification reaction. For example, pH shifts induced at the UME were used to deposit polymer and metal structures.[26, 31] Heinze and co-workers described the structured polymerization of 2,5-di-(2-methylpyrrol-2-yl)-thiophene, which is not soluble in the mediator solution, and was adsorbed at the substrate surface prior to feedback mode induced polymerization.[32] So far, surface modification using SECM feedback mode has been achieved by etching of metals and semiconductors,[7, 10, 14, 15, 18, 29] or by the deposition of metals,[8, 16, 17, 33] metal oxides,[22, 34] polymers,[9, 12, 13, 31, 35] and organic molecules or biomolecules[19-21, 23-25, 27, 28, 30, 36, 37].

In recent years, SECM has been combined with a variety of analytical techniques ranging from mass sensitive and optical methods to complementary scanning probe techniques providing structural and time-resolved information on interface processes. Combined electrochemical SPM techniques are based on integrating an electroactive area into a SPM tip. Dependent on the physical near field interaction, combinations with electrochemical scanning tunneling microscopy (ESTM-SECM),[38, 39] photoelectrochemical microscopy (PEM)-SECM[40, 41], and AFM-SECM[42-48] have been realized. Complementary bulk information on mass changes can be obtained by SECM combined with an electrochemical quartz crystal microbalance (EQCM) simultaneously detecting the generated species by SECM, and the mass change by QCM.[49-54] SECM has also been combined with optical microscopy,[55, 56] with near-field scanning optical microscopy (NSOM),[40, 41] with fluorescence spectroscopy ,[57] with chemiluminescence techniques[58-61], and with surface plasmon resonance (SPR) devices[62]. For example, Szunerits *et al.* have developed a combined SECM-SPR set-up, and have demonstrated simultaneous SPR imaging of micropatterened conducting poly(pyrrole) deposited during a SECM experiment[62]. To the best of our knowledge, the combination of SECM with spectroscopic techniques in the mid-infrared wavelength regime of the electromagnetic spectrum has not been described to date. Recently, our research group has developed a combined AFM-IR-ATR device, which enabled obtaining simultaneous spectroscopic and topographic information of dissolution processes.[63]

Mid-infrared spectroscopy is based on the excitation of fundamental vibrational modes of molecules, and is among the most powerful techniques for identifying molecular structures. In particular, the fingerprint region (10-20μm) of the IR spectrum provides sensitive and molecularly distinct absorption patterns for almost any organic molecule. Water absorption is usually a significant problem in conventional IR spectroscopy due to the strong absorption bands of water at 1640 and 3400cm^{-1}. To minimize this interference problem, infrared attenuated total reflection spectroscopy (IR-ATR) has matured into an attractive IR technique due to its exquisite surface sensitivity.[64] IR radiation coupled into an internal reflection element at angles exceeding the critical angle travels inside this optical waveguide due to total internal reflection. Given a refractive index n_1 of the waveguide and n_2 of the surrounding medium with $n_1 > n_2$, radiation penetrates a very short distance into the adjacent optically rarer medium at the condition of total reflection (for details, please refer to Chapter 2 of this thesis). This "leaky" mode is called an evanescent wave/field with a field intensity exponentially decaying with increasing distance from the interface. The penetration depth of the evanescent field is typically in the range of a few micrometers (µm), and depends on the wavelength of the radiation, the refractive indices of the waveguide and the ambient medium, and on the angle of incidence. IR absorbing molecules present close to the ATR crystal surface and within this evenascent field can therefore be detected by evanescent field absorption spectroscopy.[64] Strong IR absorbers, such as water, have only minimal adverse effects on the IR-ATR measurements compared to conventional transmission and reflection IR spectroscopy due to the limited probed analytical volume defined by the evanescent field. As examples, plasma deposited polymers interacting with analytes in aqueous solution, and electrode processes at semiconducting reflection elements in contact with electrolyte solutions have recently been studied by IR-ATR.[65]

The studies in this chapter describe the first combined SECM-IR-ATR platform enabling *in situ* IR-ATR monitoring of surface processes induced by SECM. The capabilities of this hyphenated technique were demonstrated in a model system: the deposition of microstructured polymer spots generated in feedback mode SECM with a 25µm (diam.) Pt UME simultaneously spectroscopically monitored *via* IR-ATR. In this experimental series, surface adsorbed 2,5-di-(2-thienyl)-pyrrole (**Figure 4.1**), which is insoluble in the mediator solution, was polymerized *via* tip-generated $Ru(bpy)_3^{3+}$, as previously described by Heinze and coworkers (**Figure 4.2**)[35].

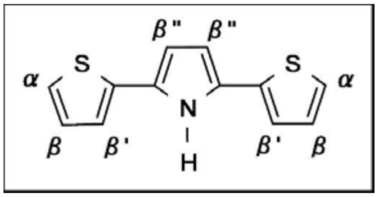

Figure 4.1: 2,5-di-(2-thienyl)-pyrrol (SNS) structure and designation of the hydrogens.

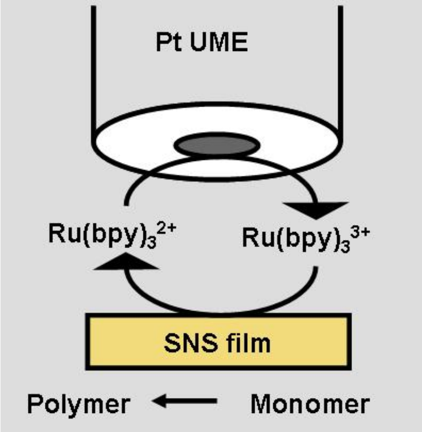

Figure 4.2: SNS polymerization *via* feedback mode SECM using $Ru(bpy)_3^{2+}$ as mediator.

All *in situ* electrochemical experiments were conducted in deuterated water, as it provides an IR transparent window in the region of 700–1000cm^{-1}, which is the region of interest for characteristic IR absorption features during the polymerization of SNS.

In addition, line-scan experiments were performed by moving the UME along cross-sections of the ATR crystal surface for experimentally mapping out the sensitive area of the ATR crystal. The insulating sheath of the UME is made from borosilicate glass (BSG), which has strong IR absorptions in the region 700-1600cm^{-1} [66, 67]. When UME is placed in the evanescent field on the ATR surface, IR features of BSG could be detected and therefore facilitates these experiments. Furthermore, spectral ray tracing simulations on the optical part of the combined SECM-IR-ATR instrument were performed for confirming the experimentally derived IR sensing area at the ATR crystal surface, and for verifying micropatterning results obtained at the ATR crystal surface.

4.3 Background

4.3.1 Background on SECM

SECM is an *in situ* technique obtaining information on the surface topography and electrochemical properties at the sub-micrometer scale, and was introduced by Bard[68] and Engström[69] at the same time. Usually, an UME is used for SECM experiments, and the current at the UME is recorded in close vicinity (several electrode radii) of a substrate (solid, or liquid) surface. Thus, the substrate surface properties may affect the steady-state Faradaic current recorded at the UME, if a redox mediator is converted at the UME, *vs*. the current obtained during the same experiment in bulk solution. Therefore, surface-sensitive (electro)chemical information is provided equivalent to other scanning near-field microscopic techniques. The UME position or movement can be precisely controlled by a three-dimensional positioning system facilitating electrochemical imaging experiments.

4.3.2 Principles of Feedback Mode SECM

Feedback mode is the most common operation mode of SECM involving a quasi reversible redox-active species (mediator; e.g., $\boldsymbol{R}$ – reduced state of the mediator in **Figure 4.3**) in the electrolyte solution. If the UME is present in bulk solution (far from the substrate), the steady state current may be described by:

$$\boldsymbol{i}_{\boldsymbol{T},\infty} = 4\boldsymbol{nFcDa}$$

Eq. 4. 1

where $\boldsymbol{n}$ is the number of transferred electrons, $\boldsymbol{F}$ is the Faraday constant, $\boldsymbol{c}$ the concentration of the redox species $\boldsymbol{R}$, $\boldsymbol{D}$ the diffusion coefficient of species $\boldsymbol{R}$, and $\boldsymbol{a}$ the radius of the microelectrode. If the UME is positioned in colse vicinity of the substrate, the steady state current will be perturbed by the electrical properties of the substrate. These current variations are schematically shown in **Figure 4.3**. If the substrate is an insulating material, hemispherical diffusion to the UME is blocked, and the resulting Faradaic current is smaller than the bulk current. This effect is called *negative feedback*. In contrast, if the substrate is conductive or an electroactive sample, the reduction of $\boldsymbol{O}$ (oxidized state of the mediator) back to $\boldsymbol{R}$ occurs at the substrate surface, which increases the concentration of $\boldsymbol{R}$ at the surface of the UME by recycling. Thereby, the current monitored by the UME is larger than the bulk current, and leads to *positive feedback*.

Exemplary approach curves for a conductive substrate (Au), and a semi-conductive substrate (Si) are shown in **Figure 4.4**.

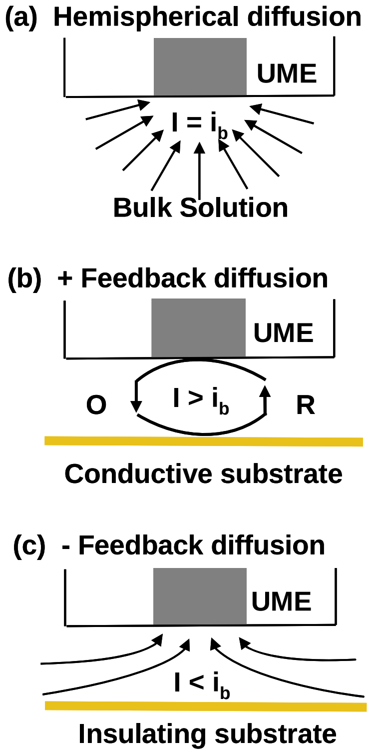

Figure 4.3: Schematic of the principles of feedback mode SECM.

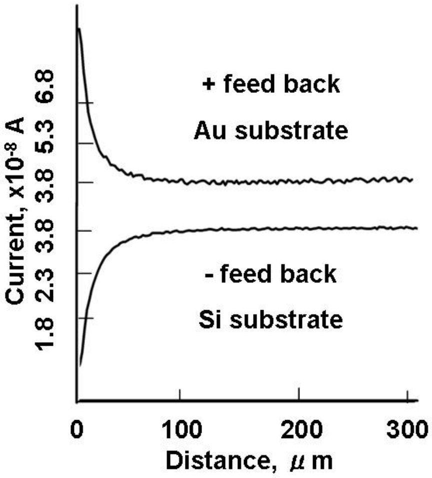

Figure 4.4: Approach curves recorded in feedback mode SECM experiments using a 25μm diam. Pt UME in 20mM $Ru(bpy)_3^{2+}$ / 100mM KCl/H_2O electrolyte solution.

4.3.3 Poly (2,5-di-(2-thienyl)-pyrrole) Deposition via Feedback Mode SECM

As shown in **Figure 4.2**, upon applying a positive potential at the UME, the mediator $Ru(bpy)_3^{2+}$ is oxidized to $Ru(bpy)_3^{3+}$ at the UME, and the oxidized species diffuses to the substrate where the SNS monomer is adsorbed. Subsequently, $Ru(bpy)_3^{3+}$ oxidizes SNS monomer to the radical cation $SNS^{\cdot+}$ (**Figure 4.5**). Generation of $SNS^{\cdot+}$ is followed by the dimer formation. Meanwhile, the reduced species $Ru(bpy)_3^{2+}$ is recovered at the sample surface during formation of the dimer. Following the dimmer formation, the induced chain reaction leads to the formation of oligomers, and finally to the formation of poly(SNS).[70]

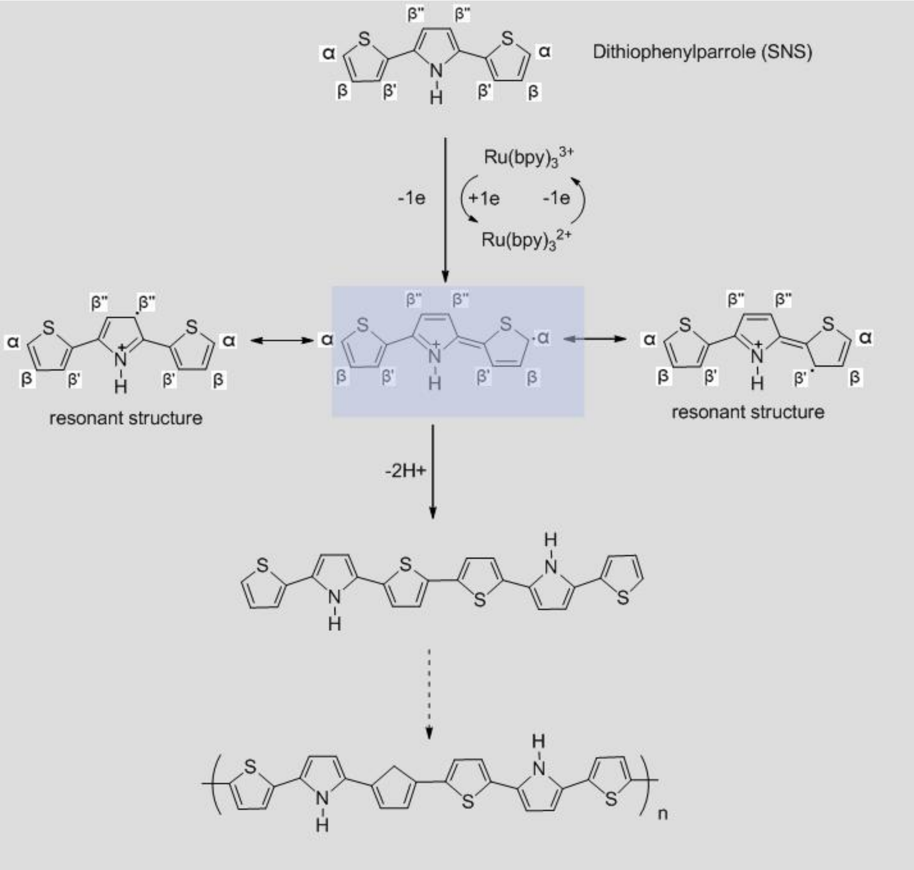

Figure 4.5: Scheme for the radical cation polymer chain reaction of 2,5-di-(2-thienyl)-pyrrole. The designation of the hydrogens in SNS is shown in the top graphs.

As evident in **Figure 4.5**, there are three resonant structures for $SNS^{\cdot+}$, and the radical could be located at the α, β', and β''–carbon, respectively. However, due to steric effects the polymerization preferentially occurs at the α position.[70]

4.3.4 Infrared Attenuated Total Reflection

For details of IR-ATR, please consult **section *2.2.1*** of this thesis, including fundamental considerations and principles.

4.4 Experimental

4.4.1 Combined SECM-IR-ATR Platform

A schematic of the developed dual-purpose instrument is shown in **Figure 4.6**.

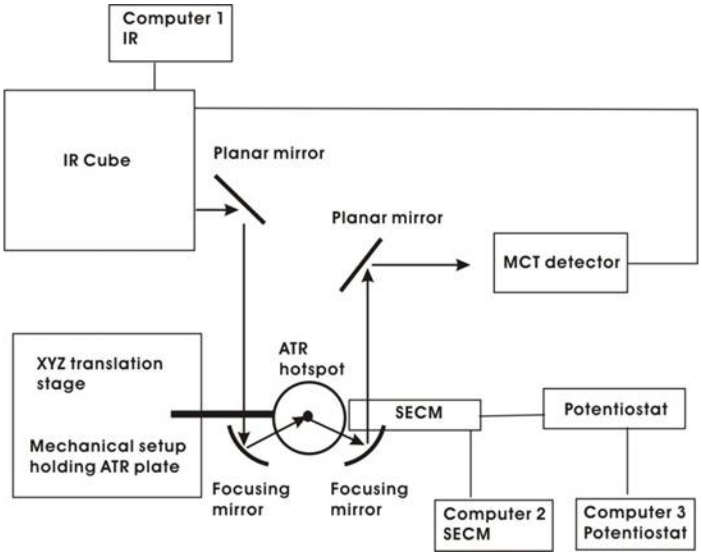

Figure 4.6: Schematic of the developed dual-purpose SECM-IR-ATR instrument.

For IR-ATR spectroscopy, broad-band IR radiation emitted by a SiC filament from a FT-IR spectrometer (IRCube-M, Bruker Optics Inc., Billerica, MA) was collimated and focused by an off-axis parabolic mirror (OAPM) onto the curvature of a single-bounce hemispherical ZnSe ATR crystal (3mm in diameter, Harrick Scientific, Pleasantville, NY). Due to the hemispherical shape of the ATR crystal, IR radiation is focused onto a smaller spot area at the flat top surface of the ATR crystal resulting in an increased sensitivity of obtained spectroscopic information within an area with a diameter of approx. 500µm. The internally reflected radiation from the top flat surface of the ATR crystal is then collimated by a second OAPM, and focused by a third OAPM onto a liquid-nitrogen cooled mercury-cadmium-telluride (MCT) detector. Processing of the spectral data recorded at the MCT is accomplished by the same FT-IR spectrometer. For combined SECM-IR-ATR studies, the ATR crystal has been custom-built into an electrochemical cell established at the central part of a base plate (**Figure 4.7**).

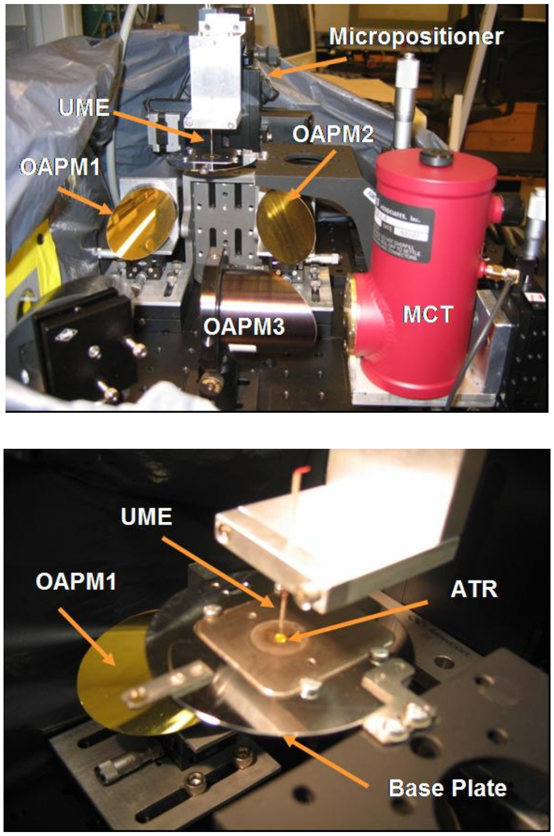

Figure 4.7: Images of the developed SECM-IR-ATR platform. (top) overview; (bottom) relative position of the ATR crystal and the UME for performing *in situ* simultaneous SECM and IR-ATR experiments.

The micropositioning system moving the microelectrode above the fixed ATR crystal is part of a custom-built SECM system driven by stepper motors (Scientific Precision Instruments GmbH®, Oppenheim, Germany) with a precision of 0.02µm. A detailed description of the SECM set-up was published elsewhere[71]. All electrochemical experiments are conducted using a CHI 842A bipotentiostat (CH Instruments, Inc., Austin, TX), and are correlated with the position of the UME using an A/D-D/A board (DAS 1602-16, Plug-In-Electronic, Eichenau, FRG). The entire combined SECM-IR-ATR system was finally sealed in a dark flexible plastic housing and purged with nitrogen to avoid possible photopolymerization reactions of SNS, and to maintain a constant atmospheric composition for the IR measurements.

IR-ATR was used to simultaneously spectroscopically monitor the progress of the electropolymerization by identifying IR changes appearing at selected frequency regions of the IR spectrum, especially at around 690cm^{-1}.[72] All IR spectra obtained by the SECM-IR-ATR platform were collected at a resolution of 4cm^{-1}, and by averaging 100 scans; the data were analyzed with OPUS (OPUYS Software, Bruker Optics Inc., Billerica, MA).

4.4.2 UME Preparation

Disk–shaped microelectrodes were fabricated as previously described[6] by sealing a 25µm (diam.) Pt wire under vacuum into a borosilicate glass capillary. Successive grinding and polishing with diamond paste (6µm and 3µm) and with alumina paste (1µm and 0.05µm), respectively, exposes a disk-shaped microelectrode. Characterization of the UME was performed by cyclic voltammetry, and by optical microscopy.

4.4.3 Chemicals

Deuterated water (D_2O), $Ru(bpy)_3Cl_2{\cdot}6H_2O$, KCl (reagent grade), and acetone (ACS spectrophotometric grade) were obtained from Sigma Aldrich (St. Louis, MO). Deionized water (Milli-Q water system, Millipore Corp., Billerica, MA) was used, if not stated otherwise. A 0.02M $Ru(bpy)_3Cl_2{\cdot}6H_2O$ / 0.1M KCl electrolyte solution was prepared in D_2O. All solutions were deoxygenated by purging with UHP argon (Airgas, Hapeville, GA) prior to electrochemical experiments.

2,5-di-(2-thienyl)-pyrrol (SNS) monomer was synthesized and purified based on the method described by Wynberg *et al*.[73]. The precursor (1,4-bis(2-thienyl)butanedione) of SNS was prepared following the procedure by Stetter *et al*.[74]. The resulting 1,4-diketone was allowed to react with ammonium acetate, which resulted in the target SNS with a yield of 75%.[73] SNS monomer was purified and stored under argon. 0.1M SNS was dissolved in acetone, and then drop-casted onto the ATR crystal surface.

4.4.4 Ex Situ FT-IR Studies on SNS Monomer and Electrogenerated Poly(SNS)

A three-electrode configuration with a Pt sheet ($1cm^2$) as working electrode, a Pt mesh (effective area $10cm^2$) as auxiliary electrode, and an Ag/AgCl quasi reference electrode was used for macroscopic poly(SNS) deposition.

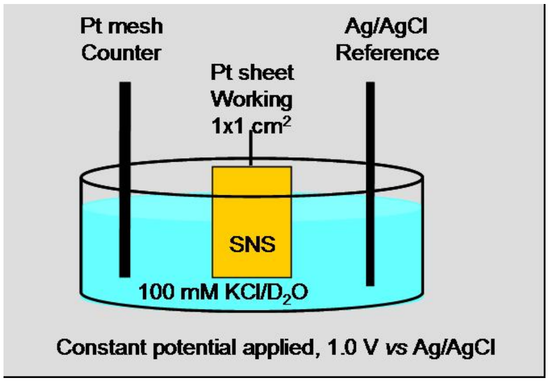

Figure 4.8: Three-electrode configuration for *ex situ* electrogenerated polymerization of SNS.

Both Pt sheet and mesh were flame-burned before usage. The Pt sheet was coated with SNS monomer, and then immersed in 0.1M KCl aqueous solution. Prior to initiating the deposition, cyclic voltammetry was performed in a range of 0-1.2V (*vs*. Ag/AgCl) at a scan rate of 0.1V/s to determine the oxidation rate of the monomer. A constant potential of 1.0V *vs*. Ag/AgCl was applied to the Pt sheet for 2, 5, or 10min in a series of amperometry experiments for SNS polymerization. A poly(SNS) film with a thickness of approx. 2μm was deposited during all time intervals mentioned above in controlled amperometric polymerization experiments. IR absorption spectra of the adsorbed SNS monomer film prior to polymerization, and of the poly(SNS) films generated at different polymerization times were collected using a nitrogen purged Equinox 55 FT-IR spectrometer (Bruker Optics Inc., Billerica, MA). All IR spectra were collected at a resolution of 4cm^{-1}, and by averaging 100 scans. Analysis of the spectra was performed using the OPUS software package.

4.4.5 SECM Feedback Mode Polymerization of SNS

A 0.1M SNS monomer solution was coated onto the surface of a ZnSe crystal (covered area ~1cm^2) by drop-casting, and the SNS-modified ZnSe was fixed in the conventional SECM cell as sample substrate. A three-electrode assembly using a 25μm Pt disk UME as working electrode, a Pt wire auxiliary electrode, and an Ag/AgCl wire reference electrode was used during all SECM experiments. The cell was filled with 0.02M $Ru(bpy)_3Cl_2$ / 0.1M KCl/D_2O. SECM approach curves at a potential of 1.0V *vs*. Ag/AgCl were recorded, and the approach of the UME towards the SNS-coated ZnSe crystal was stopped once the steady state current had increased by 20% compared to the steady state current at the UME in bulk solution. Poly(SNS) spots were formed at different locations of the ZnSe crystal by applying a constant potential of 1.0V *vs*. Ag/AgCl. At this potential, the mediator $Ru(bpy)_3^{2+}$ is oxidized to $Ru(bpy)_3^{3+}$ at the UME, and diffuses to the ZnSe crystal when the UME is in close proximity to the sample surface. $Ru(bpy)_3^{3+}$ oxidizes the adsorbed SNS monomer, thereby forming the radical cation SNS^+. followed by the condensation reaction of SNS^+ to the dimer. Chain propagation finally leads to oligomers, and to poly(SNS), as shown in **Figure 4.2**.[70]

4.4.6 Simultaneous IR-ATR Studies on Microstructured Poly(SNS) Formation by SECM

The SNS monomer film was deposited on the hemispheric ZnSe ATR crystal by drop-casting from 0.1M SNS acetone solution. Electropolymerization was obtained by feedback mode SECM in 0.02M $Ru(bpy)_3Cl_2$ / 0.1M KCl/D_2O solution, as described above in **section 4.4.5**. The aaproach of UME tip to the sample surface was conducted by monitoring the feedback current, and stopped once the current at the tip increased by 20%

compared to the current in bulk solution. *In situ* evanescent field IR absorption spectra were collected during the progress of feedback mode SECM polymerization reactions at different time intervals (5, 10, 20, and 30min). In addition, the micropatterning of multiple polymer spots *via* electropolymerization at the hemispherical ZnSe ATR crystal surface via SECM was also simultaneously monitored by *in situ* evanescent field FT-IR absorption measurements. The UME was positioned close to the center of the SNS-coated hemispheric ZnSe crystal following the method mentioned above (feedback current increased by 20% compared to the bulk current), and was then moved in constant height to five discrete locations at the crystal surface. At each location, the UME was held stationary for 20min to locally polymerize adsorbed SNS. An IR spectrum was collected at the end of each individual polymerization step. Prior to coating the SNS monomer film onto the ATR crystal surface, a background spectrum of the bare crystal was recorded in nitrogen atmosphere. In addition, prior to combined SECM-IR-ATR experiments *in situ* monitoring *via* IR spectra was tested using a macroscopic Pt electrode (1mm) for electropolymerization. The macroscopic electrode was positioned at a distance of approx. 100µm from the SNS/ATR crystal substrate surface by first carefully touching the sample surface, and slightly retracting the electrode prior to initiating the electropolymerization. The electrode was maintained at that position until no further IR signal change was evident during the observed electropolymerization process.

4.4.7 Line-Scans at the ATR Crystal Surface

A conical shaped UME with a diameter of 300 µm was positioned in close proximity to the ATR surface. Then, the UME was moved along cross-sections of the ATR crystal, while collecting IR spectra at intervals of 30μm resulting in 30 IR measurements along each line-scan. Each spectrum averaged 64 scans with a spectral resolution of 4cm^{-1}. The UME first moved from left edge to right edge of ATR crystal surface or vise verse. The center of ATR crystal surface was estimated as one of the positions of UME movements where the strongest IR absorption of BSG was generated. Then, UME moved to the upper edge of ATR crystal, and started the other line-scan passing through the estimated center from the upper edge to bottom edge of AR crystal surface.

4.4.8 Optical Ray Tracing Simulations of Hemispherical ATR Crystals

The IR sensing area of the ATR crystal was theoretically calculated using the spectral simulation package SPRAY (W. Theiss, Aachen, Germany). A simple five-component model was derived by simulating the experimental setup in real dimensions. In the simulation, IR radiation was emitted by a circular light source with a diameter of 2.54cm, reflected by 90° by a flat mirror with a diameter of 5.08cm, and then focused onto the curvature of a hemispherical ZnSe ATR crystal by a 90° OAPM with a diameter of 5.08cm. The incident angle of the IR radiation to the sensing surface of the ATR crystal was assumed to be 45°. This approximation resulted in sufficiently accurate results, despite neglecting the real experimental optical conditions, where the angle of incidence is composed of an angular range resulting from focusing effects of the OAPM and the hemispherical ZnSe ATR crystal (refractive index 2.4). Furthermore, a rectangular virtual screen with a dimension of 3x3cm was defined for visualizing the radiation distribution at the flat surface of the ATR crystal. Simulations were performed for the spectral region of 600-1000cm^{-1}, where the IR absorption changes of SNS during the polymerization were studied for monitoring the polymerization process. 100 data points spanning a spectral region of 400cm^{-1} defined a resolution of 4cm^{-1} in the simulation, with the light source emitting 200 rays per spectral point (with a randomly selected distribution of frequencies within the spectral window of interest defined above), once executing the ray tracing simulation.

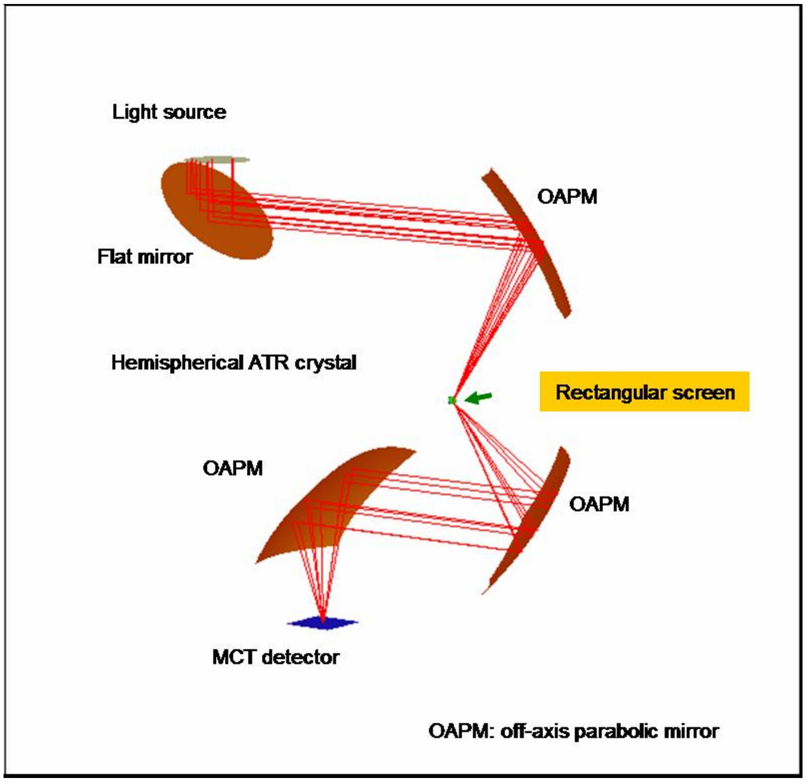

Figure 4.9: Schematic of the model and spectral ray tracing procedure for the combined SECM-IR-ATR optical set-up.

This configuration was used for determining the influence of different radiation cone angles (0.1°, 0.5°, 1°, 2°, and 3°) on the dimension of the IR sensitive area at the ATR crystal surface, and for estimating the percentage of radiation reaching the MCT detector. To do so, three more components were added into the simulation model based on their positions and real dimensions in the experiment set-up - two more 90° OAPMs with a diameter of 5.08cm for focusing the radiation coming from the ATR crystal onto a virtual detector element with a dimension of 2 x 2 mm.

4.5 Results and Discussion

4.5.1 FT-IR Studies of SNS Monomer and Electrogenerated Poly(SNS)

A number of papers have been published studying the electrochemical properties of SNS in organic[75-78] or water/organic[79] solvents with appropriate supporting electrolytes. Cyclic voltammetry was applied to study the electrochemical properties of SNS in aqueous solution. Hence, five cycles were recorded at the Pt electrode, with the second and the last voltammogram shown in **Figure 4.10**.

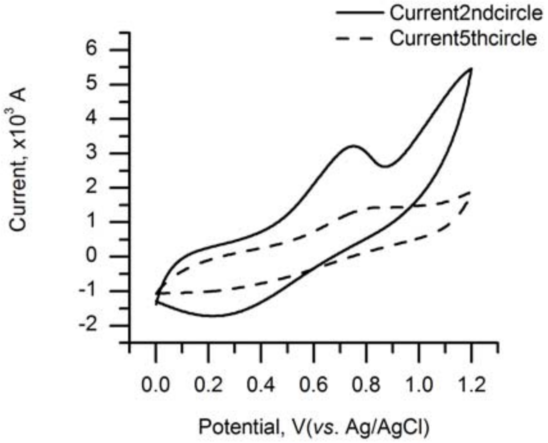

Figure 4.10: Cyclic voltammograms of SNS at 1cm^2 Pt sheet electrode. Scan rate: 0.1Vs^{-1}.

As evident from the CV of the second cycle, the anodic peak is much stronger than the catholic peak; the last cycle shows that both the anodic and catholic peaks become flattened. This indicates that the oxidation of SNS is not fully revisable. SNS monomer was coated onto the Pt sheet, and immersed in 0.1M KCl aqueous solution. The obtained results are consistent with literature data on the electrogenerated polymerization of 2,5-bis(1-methylpyrrol-2-yl)thiophene[32], which has similar chemical properties as SNS. *Ex situ* FT-IR studies after polymerization have been performed to identify the primary polymerization position(s), and the time-dependence of the polymerization grade of SNS. **Figure 4.11** shows the spectral changes of the IR absorption spectra with polymerization time.

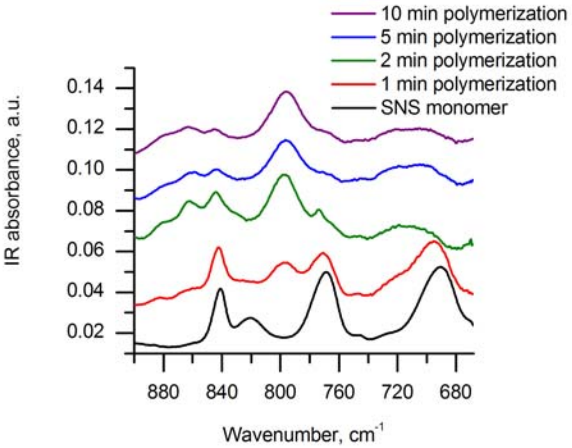

Figure 4.11: *Ex situ* IR characterization of poly(SNS) formed at a Pt sheet electrode using different electropolymerization times.

The out-of-plane C-H bending vibrations in the region of 600-1600cm^{-1} were analyzed for characterizating the extent of SNS polymerization. Regarding the IR absorption from the different types of hydrogens of the SNS monomer, α-H has a characteristic peak around 690cm^{-1}, β-H and β'-H around 842cm^{-1}, and β''-H around 770cm^{-1}.[72, 78] During the polymerization process, the relative peak intensity for the α-H dramatically decreases; a peak around 800cm^{-1} attributed to β''-H emerges, and its intensity increases with progressing polymerization due to the flanking of the middle pyrrole ring of SNS in the poly(SNS). In addition, weaker absorption peaks appear in the higher fingerprint frequency region (850-900cm^{-1}) related to the β-H and β'-H at the end of the polymer chain. Based on the polymerization time dependent spectra, it can be concluded that the SNS polymerization in aqueous solution primarily occurs at the α-position, and hence, the intensity change of the α-H peak is an indicator for monitoring the polymerization level.

4.5.2 SECM Feedback Mode Polymerization of SNS

After a layer of SNS was coated onto the ATR crystal surface, the electrode tip was brought to the surface by monitoring the feedback current until an increase by 20% compared to the current in bulk was observed. The tip-generated $Ru(bpy)_3^{3+}$ subsequently oxidizes SNS monomer at the surface to an intermediate radical cation SNS^+, which is followed by dimer formation, oligomerization, and poly(SNS) formation[70] (**Figure 4.2** & **Figure 4.3**). After feedback mode induced polymerization, the SNS/ZnSe was rinsed with DI H_2O. Since neither SNS nor poly(SNS) is soluble in water, black poly(SNS) spots remained embedded within the SNS monomer matrix. SNS monomer was removed from the substrate by rinsing with acetone leaving well-defined poly(SNS) spots behind. An optical image of poly(SNS) spots generated during a feedback mode experiment are shown in **Figure 4.12**.

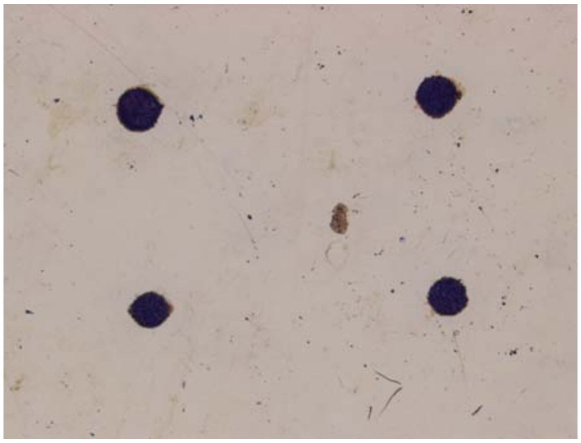

Figure 4.12: Optical image of poly(SNS) spots formed at the ZnSe crystal surface at different electropolymerization time intervals: upper left – 20min; upper right – 15min; bottom left – 5min, bottom right – 10min.

Figure 4.12 also reveals that the poly(SNS) spot size increases with increasing electropolymerization time. The generated polymer spots ranged from 180 to 210μm in diameter with respect to polymerization times ranging from 5 to 20min, respectively. **Table 4.1** summarizes these feedback mode polymerization results.

Table 4.1: Changes of the poly(SNS) spot size with polymerization time.

Time, min	5	10	15	20
Spot size diam., μm	180	190	200	205

The dimension of the obtained spots are within the range of the entire UME diameter (active electrode and glass insulation), which is related to the diffusion of the redox mediator $Ru(bpy)_3^{3+}$ and the SNS radical cations, the distance between UME and the SNS/ZnSe surface, the kinetics of involved surface reaction, and the electrochemical reaction time.[6]

4.5.3 In Situ IR-ATR Studies on Surface Modifications Induced by Feedback Mode SECM

Prior to the polymerization reaction, the thickness of the adsorbed SNS film at the hemispherical ZnSe ATR crystal surface was determined by AFM height measurements (**Figure 4.13**).

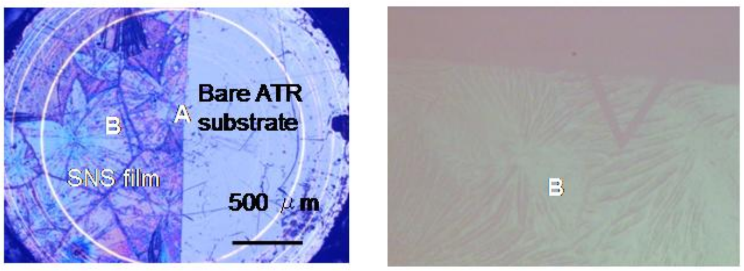
(a) Optic micrographs of SNS film on ATR

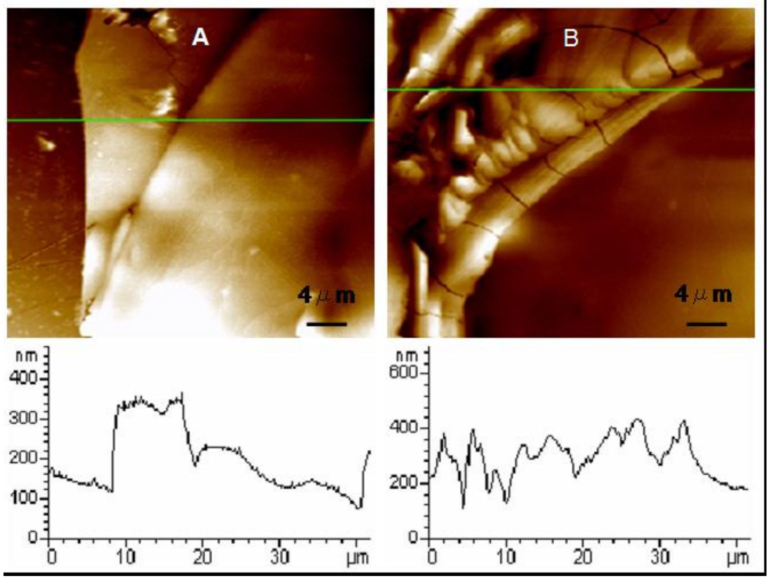
(b) AFM measurement on SNS film

Figure 4.13: (a) Optical microscopy, and (b) AFM topography measurements at SNS thin film coated onto the ZnSe crystal surface. Region A – edge of SNS film; region B – SNS film

The average thicknesses ranged from 200-400nm. The stability of the SNS film coated onto the hemispherical ZnSe ATR crystal was monitored *via* IR-ATR during eight hours after coating the crystal in the combined SECM-IR-ATR set-up, which was purged with inert nitrogen. No change of the IR signal was observed for that period of time.

All *in situ* electrochemical experiments were conducted in deuterated water, as it provides an IR transparent window in the region of 700–1000cm^{-1}, which is the region of interest for characteristic IR absorption features during the polymerization of SNS.

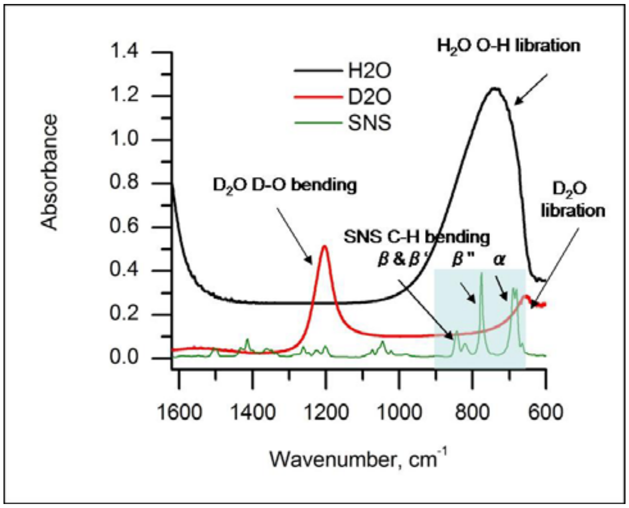

Figure 4.14: IR absorption spectra of H_2O, D_2O, and SNS.

Prior to the microstructured deposition using SECM, a 1mm Pt electrode was positioned at a close distance of approx. 100µm to a SNS-modified ZnSe crystal surface. By applying a potential of 1V *vs.* Ag/AgCl in 0.02M Ru(bpy)$_3$Cl$_2$ / 0.1M KCl/D_2O, the current rapidly increased and then dropped to the bulk current after approx. 2min. **Figure 4.15** presents the IR spectra of the SNS film before and after 2min of electropolymerization. There was no further IR change evident when continuing the electropolymerization for two more minutes.

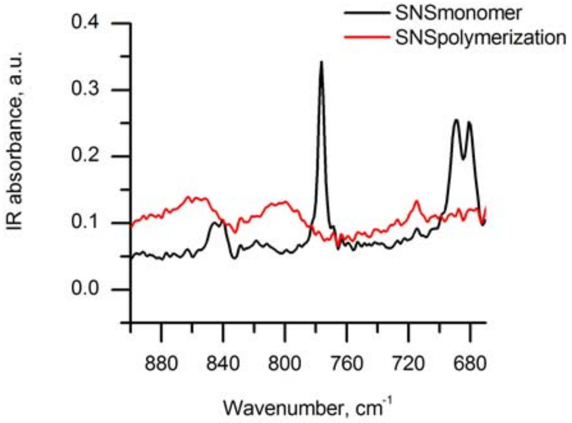

Figure 4.15: *In situ* simultaneous IR-ATR characterization of SNS polymerization using a 1mm Pt disk electrode.

After rinsing with DI H_2O and acetone, a black poly(SNS) spot of approximately 1.8mm diameter was visible at the surface of the hemispherical ATR crystal. The IR data obtained from this experiment is in excellent agreement with the data presented in **Figure 4.11** on *ex situ* FT-IR studies of SNS monomer and electrogenerated poly(SNS).

Three consecutive *in situ* time-dependant polymerization experiments using the combined SECM-IR-ATR platform were performed. One representative data set of the IR measurements for a polymerization sequence over 20min in the region of 670-710cm^{-1} presenting the out-of-the plane α-H bending vibration is shown in **Figure 4.16**.

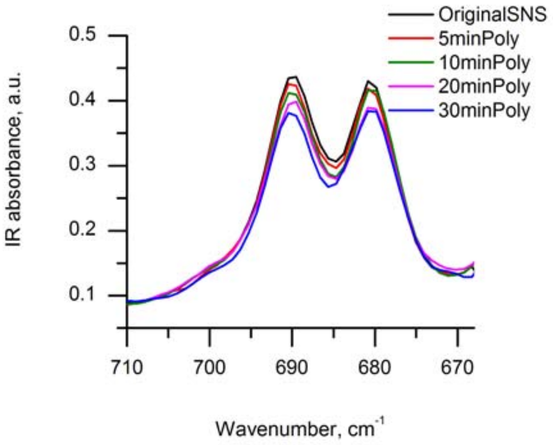

Figure 4.16: *In situ* simultaneous IR-ATR characterization of time-dependant SNS polymerization during feedback mode SECM using a 25µm Pt UME.

The α-H peak areas were integrated from 670-710cm^{-1}, and the polymerization levels for different reaction times were calculated by determining the ratio of the integrated α-H peak area of polymerized SNS at the different polymerization times, and the integrated α-H area of SNS monomer. Calculated polymerization levels for three sets of experiments are presented in **Table 4.2**.

Table 4.2: Changes of the polymerization level with respect to polymerization time for three sets of time-dependant *in situ* electropolymerizations of SNS. Unit: %

Time, min	Exp. 1	Exp.2	Exp.3
5	2.78	3.19	5.72
10	8.64	9.31	13.4
20	15.7	17.1	21.2
30	19.1	23.4	26.5

AFM and optical microscopy images in **Figure 4.13** reveal that the monomer film thickness is not homogeneous. The film thickness ranges from 200-400nm with ridges and relatively flat regions formed during film adsorption. Hence, the resulting poly(SNS) films may have different thickness and different levels of polymerization with respect to the same length of reaction time during the IR measurements. Although the distance between UME and the SNS/ZnSe surface was controlled by monitoring the feedback current, the bulk and the on-position current were not exactly the same for each experiment given the time scale for the three different polymerizations. Furthermore, the sensitivity of combined IR-ATR may vary at different locations of the ZnSe crystal due to the rather localized evanescent field at single bounce crystals.[80] All factors mentioned above may cause that the same amount or percentage of polymerization of SNS does not generate exactly the same IR signal change.

Figure 4.17 shows *in situ* IR-ATR monitoring of the formation of six poly(SNS) spots induced by feedback mode SECM. The inserted scheme shows the relative positions of these spots at the crystal surface.

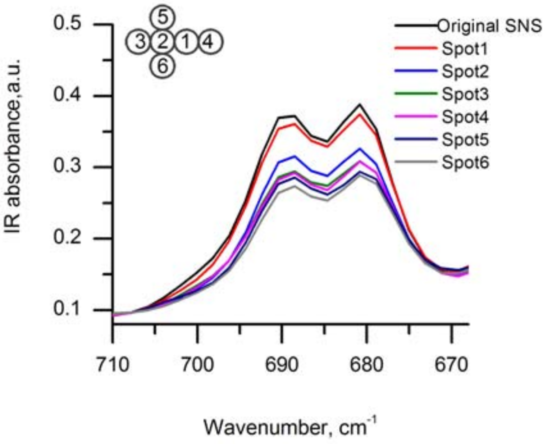

Figure 4.17: *In situ* simultaneous IR-ATR characterization of poly(SNS) micropatterning using feedback SECM at a 25μm Pt UME.

The α-H peak areas were integrated in the range of 670-710cm^{-1}, and the overall polymerization levels after each polymer spot deposition were calculated by determining the ratio of the integrated α-H area of poly(SNS), and the integrated α-H area of SNS monomer. The calculated polymerization level results are summarized in **Table 4.3**. The differences of polymerization level between two adjacent polymer spot depositions are also listed in **Table 4.3**.

Table 4.3: Changes of overall polymerization level with respect to polymerization micropatterning location, and differences of polymerization levels between two adjacent polymerization spots. Unit: %

	Spot1	Spot2	Spot3	Spot4	Spot5	Spot6
Overall polymization level	6.35	23.8	30.2	30.6	36.1	39.3
$\Delta(\text{Poly}_i - \text{Poly}_{i-1})$	6.35	17.5	6.4	0.5	5.5	3.2

It is observed that the spot deposition at location 2, which gave a change of 17.5%, is much higher than at all other spots; the spot deposition at location 4, which gave a change of 0.5%, is much lower than at all other spots. These variations could relate to the difference in sensitivity at the ATR crystal surface at different locations, and/or to the non-homogeneity of the SNS monomer film.

4.5.4 Ray Tracing Simulation of the Sensing Area at the Surface of Hemispherical ZnSe ATR Crystals

With the increase of divergent angle of the circular light source, the possible active sensing spot area increases, along with a decrease of radiation intensity per unit sensing area. **Figure 4.18** shows the corresponding simulation results. The percentage of rays counted at the ATR crystal surface was calculated by dividing the number of rays counted at the ATR crystal surface (via the rectangular virtual screen) by the number of total rays emitted by the simulated light source. The average ray density at the ATR crystal surface was calculated by dividing the number of rays at the ATR crystal surface by the area of the ATR crystal (3mm in diam.).

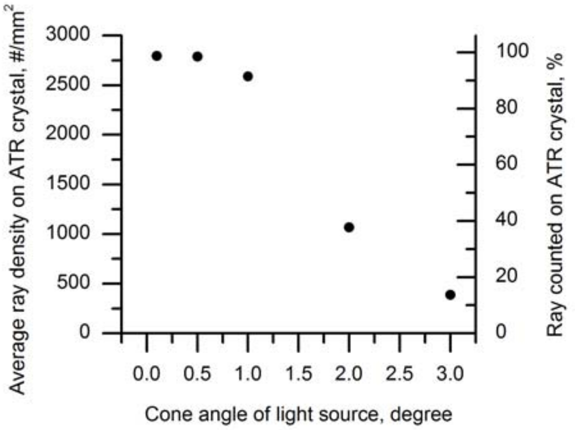

Figure 4.18: Change of average light distribution at the ATR crystal surface with increasing divergent emission angles of the light source.

The percentage of radiation at the detector dramatically decreases with an increase of angular divergence of the radiation cone emitted by the light source. **Figure 4.19** shows a summary of these simulation results, which imply that the sensitivity at the IR crystal surface can be significantly improved, if a highly collimated light source is applied.

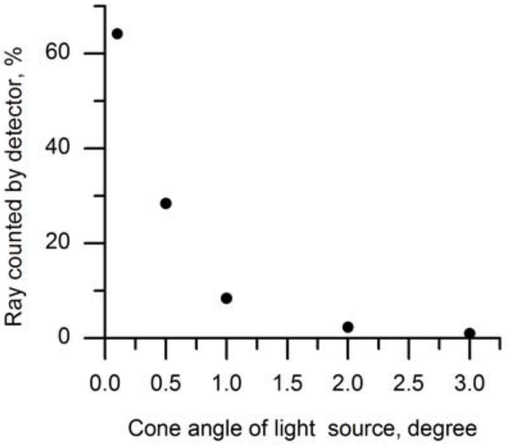

Figure 4.19: Change of average sensitivity with increasing divergent emission angles of the light source.

The divergent angle not only broadens the distribution of IR radiation at the active ATR crystal sensing surface, but also changes the direction of radiation propagation, and induces stray light, which cannot be focused onto the ATR crystal and/or cannot be detected by the detector element. **Figure 4.20** shows the 3-D light distribution for a three-degree divergent angle (technical data on the emission characteristics of the light source provided by the manufacture) of the light source at a 3x3mm virtual screen, which was placed in the simulation at the ATR sensing surface.

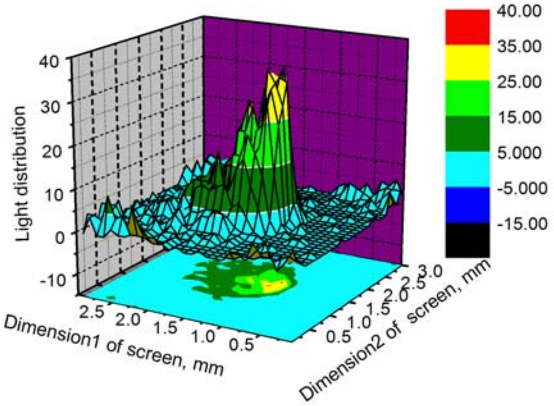

Figure 4.20: Simulation of 3-D light distribution at the IR sensing surface of a hemispherical ATR crystal, as used in the combined SECM-IR-ATR system.

2x10^4 rays were emitted by the light source, however, only 13.7% of these rays are evident at the virtual screen located at the ATR crystal surface. Since, by definition, the screen is of a rectangular not a circular as ATR crystal surface is of, the counted percentage of ray at the ATR crystal should be less than 13.7%. **Figure 4.21** shows the light distribution along the cross-sections of the virtual screen.

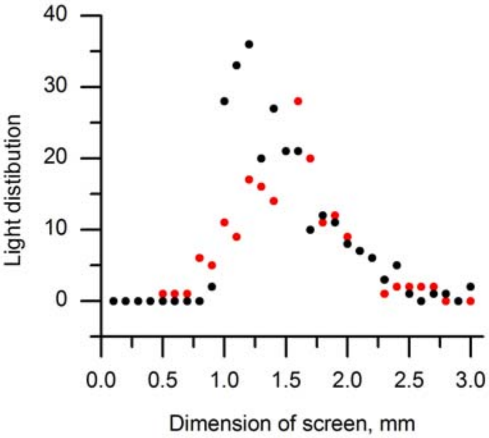

Figure 4.21: Simulation of the radiation distribution along cross-sections of the IR sensing surface at a hemispherical ATR crystal.

The asymmetry of the radiation distribution in **Figure 4.20** & **Figure 4.21** is attributed to multiple internal reflections. The simulation results presented in **Figure 4.20** & **Figure 4.21** reveal that the active sensing area of the 3mm ATR crystal is approximately 1.5mm in diameter. Consequently, the simulated radiation distribution theoretically elucidates the non-homogeneous sensitivity at the ATR crystal surface, which may partially explain the variation of spectroscopically determined polymerization levels at different locations of the IR waveguide.

4.5.5 Line-scans of UME for Experimentally Investigating the Sensitive Area at the ATR Crystal Surface

Complementary to the theoretical studies discussed above, line-scans with the UME across the ATR crystal surface and within the evanescent field should experimentally map out the approximate dimensions of the active sensing region at the ATR crystal surface. **Figure 4.22** gives the IR absorption spectrum of an UME (i.e., the IR signature of the insulating glass sheath) with an assignment of the absorption features.

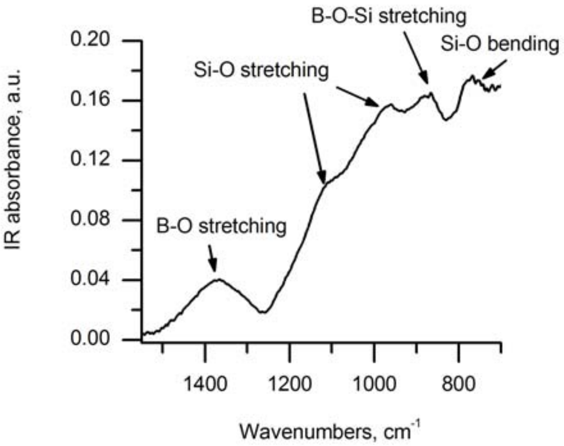

Figure 4.22: IR absorption spectrum of borosilicate glass (BSG) with peak assignments.

Representative IR absorption spectra for a line-scan across a distance of 300µm from the center toward the edge of the ATR crystal are displayed in Figure 4.23. It is clearly evident that, as expected, the IR absorption intensities gradually decrease with UME movement, and flatten out after 270µm movement.

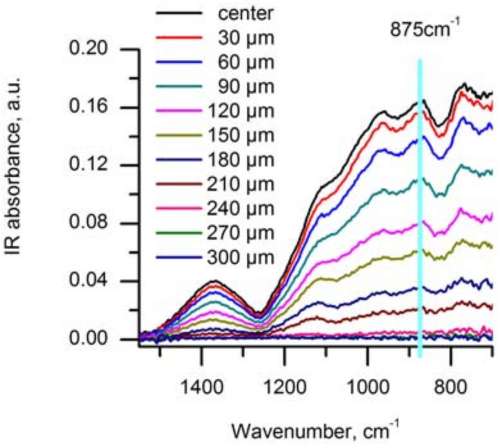

Figure 4.23: Representative IR absorption spectra for a 300 µm distance line-scan from the center toward the edge of the ATR crystal. IR absorption intensities decrease gradually with UME movement.

The absolute peak height intensities at 875cm^{-1} are shown in **Figure 4.24** for a set of full line-scans of 900µm along cross-sections of the ATR crystal surface. **Figure 4.24** shows that the sensitive area of ATR crystal is approx. 540µm in diameter.

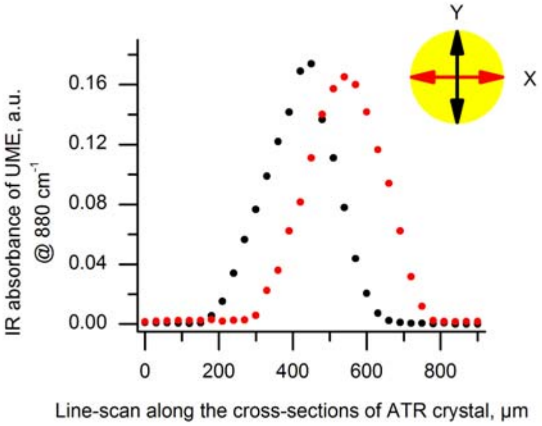

Figure 4.24: Line-scan results along the cross-sections of ATR crystal surface by evaluating the evanescent field absorption signature of the UME. Red dots – Line-scan along X; black dots – Line-scan along Y.

These experimental line-scans combined with the polymer spot size results shown in **Table 4.1** can answer, why the polymerization at location 4 did not generate observable IR signal changes – location 4 was clearly positioned beyond the nominally sensitive area of the ATR crystal. The line-scan results also experimentally confirm the non-homogeneous sensitivity distribution at the ATR crystal surface. Both line-scan and simulation results are consistent with the experimental result obtained by using the 1mm Pt electrode, which indicated that the sensitive area of ZnSe ATR crystal is ≤1.8 mm in diameter.

4.6 Conclusions

This chapter presents the first combination of *in situ* scanning electrochemical microscopy with attenuated total reflection infrared spectroscopy using a single bounce ATR unit as SECM sample substrate. The capabilities of this combination were demonstrated by simultaneous spectroscopic (IR-ATR) monitoring of the microstructured electropolymerization of 2,5-di-(2-thienyl)-pyrrole induced by feedback mode SECM. The level of polymerization could be monitored by simultaneously recording IR spectra during the polymerization process. IR spectra in the fingerprint region revealed the polymerization level and the mechanism, and the obtained results are in good agreement with *ex situ* data published in the literature. The investigation results on *in situ* polymerization processes comply well with the spectral ray tracing and UME line-scan results at the ATR crystal surface.

4.7 Outlook

4.7.1 Instrumental Improvements on SECM-IR-ATR

With the implementation of the recently reported combination of single-mode MIR waveguides and frequency-matched quantum cascade lasers[81, 82], the achievable sensitivity during IR evanescent field absorption measurements will be significantly improved due to the enhanced intensity of the evanescent field. This technology will further facilitate the integration of IR methods with SECM imaging techniques and shall provide sensitivities suitable for studying biological samples.

4.7.2 Triple Combination AFM-SECM-IR-ATR

Recent research in our group has demonstrated that IR-ATR may be combined with atomic force microcopy (AFM), which allows simultaneously monitoring IR spectra and topographical changes at the ATR crystal surface in liquid environments.[63] Future research is targeted towards combining AFM-SECM with IR-ATR by using integrated AFM-SECM scanning probes.[45, 83]

4.7.3 Investigating Organic and Biological Samples via AFM-SECM-IR-ATR

The potential triple combination AFM-SECM-IR-ATR will enable simultaneous *in situ* topographic (AFM) and spectroscopic (IR-ATR) monitoring along with electrochemical imaging (SECM) or electrochemically induced processes such as e.g., the laterally resolved deposition of conducting polymers. Furthermore, with improved sensitivity a combined AFM-SECM-IR-ATR may be applicable for multiparametric monitoring of a wide range of relevant chemical and biological processes that involve e.g., topographical and correlated spectroscopic observation of changes at a sample induced by SECM or simultaneously imaged by SECM such as e.g., characterization of enzyme patterns and activities at diamond-like carbon modified ZnSe substrates, DNA hybridization, and cellular signaling processes. [68, 84-87]

4.8 References

(1) Brucherseifer, M.; Kranz, C.; Mizaikoff, B., *Combined in Situ Atomic Force Microscopy- Infrared-Attenuated Total Reflection Spectroscopy*, Anal. Chem. **2007**, *79*, 8803-8806.

(2) Kranz, C.; Friedbacher, G.; Mizaikoff, B.; Lugstein, A.; Smoliner, J.; Bertagnolli, E., *Integrating an Ultramicroelectrode in an AFM Cantilever: Combined Technology for Enhanced Information*, Anal. Chem. **2001**, *73*, 2491-2500.

(3) Shin, H.; Hesketh, P. J.; Mizaikoff, B.; Kranz, C., *Batch Fabrication of Atomic Force Microscopy Probes with Recessed Integrated Ring Microelectrodes at a Wafer Level*, Anal. Chem. **2007**, *79*, 4769-4777.

(4) Wittstock, G.; Burchardt, M.; Pust, S. E.; Shen, Y.; Zhao, C., *Scanning electrochemical microscopy for direct imaging of reaction rates*, Angew. Chem., Int. Ed. **2007**, *46*, 1584-1617.

(5) Sun, P.; Laforge, F. O.; Mirkin, M. V., *Scanning electrochemical microscopy in the 21st century*, Phys. Chem. Chem. Phys. **2007**, *9*, 802-823.

(6) Bard, A. J.; Mirkin, M. V. *Scanning Electrochemical Microscopy*; Marcel Dekker: New York, 2001.

(7) Lin, C. W.; Fan, F. R. F.; Bard, A. J., *High resolution photoelectrochemical etching of n-gallium arsenide with the scanning electrochemical and tunneling microscope*, J. Electrochem. Soc. **1987**, *134*, 1038-1039.

(8) Craston, D. H.; Lin, C. W.; Bard, A. J., *High resolution deposition of silver in Nafion films with the scanning tunneling microscope*, J. Electrochem. Soc. **1988**, *135*, 785-786.

(9) Wuu, Y. M.; Fan, F. R. F.; Bard, A. J., *High resolution deposition of polyaniline on platinum with the scanning electrochemical microscope*, J. Electrochem. Soc. **1989**, *136*, 885-886.

(10) Husser, O. E.; Craston, D. H.; Bard, A. J., *Scanning electrochemical microscopy. High-resolution deposition and etching of metals*, J. Electrochem. Soc. **1989**, *136*, 3222-3229.

(11) Kranz, C.; Gaub, H. E.; Schuhmann, W., *Polypyrrole towers grown with the scanning electrochemical microscope*, Adv. Mater. **1996**, *8*, 634-637.

(12) Kranz, C.; Ludwig, M.; Gaub, H. E.; Schuhmann, W., *Lateral deposition of polypyrrole lines by the scanning electrochemical microscope*, Adv. Mater. **1995**, *7*, 38-40.

(13) Kranz, C.; Ludwig, M.; Gaub, H. E.; Schuhmann, W., *Lateral deposition of polypyrrole lines over insulating gaps. Towards the development of polymer-based electronic devices*, Adv. Mater. **1995**, *7*, 568-571.

(14) Mandler, D.; Bard, A. J., *Scanning electrochemical microscopy: the application of the feedback mode for high resolution copper etching*, J. Electrochem. Soc. **1989**, *136*, 3143-3144.

(15) Mandler, D.; Bard, A. J., *High resolution etching of semiconductors by the feedback mode of the scanning electrochemical microscope*, J. Electrochem. Soc. **1990**, *137*, 2468-2472.

(16) Mandler, D.; Bard, A. J., *A new approach to the high resolution electrodeposition of metals via the feedback mode of the scanning electrochemical microscope*, J. Electrochem. Soc. **1990**, *137*, 1079-1086.

(17) Meltzer, S.; Mandler, D., *Microwriting of gold patterns with the scanning electrochemical microscope*, J. Electrochem. Soc. **1995**, *142*, L82-L84.

(18) Meltzer, S.; Mandler, D., *Study of silicon etching in HBr solutions using a scanning electrochemical microscope*, J. Chem. Soc., Faraday Trans. **1995**, *91*, 1019-1024.

(19) Nowall, W. B.; Wipf, D. O.; Kuhr, W. G., *Localized Avidin/Biotin Derivatization of Glassy Carbon Electrodes Using SECM*, Anal. Chem. **1998**, *70*, 2601-2606.

(20) Shiku, H.; Takeda, T.; Yamada, H.; Matsue, T.; Uchida, I., *Microfabrication and Characterization of Diaphorase-Patterned Surfaces by Scanning Electrochemical Microscopy*, Anal. Chem. **1995**, *67*, 312-317.

(21) Shiku, H.; Uchida, I.; Matsue, T., *Microfabrication of Alkylsilanized Glass Substrate by Electrogenerated Hydroxyl Radical Using Scanning Electrochemical Microscopy*, Langmuir **1997**, *13*, 7239-7244.

(22) Shohat, I.; Mandler, D., *Deposition of nickel hydroxide structures using the scanning electrochemical microscope*, J. Electrochem. Soc. **1994**, *141*, 995-999.

(23) Widrig, C. A.; Chung, C.; Porter, M. D., *The electrochemical desorption of n-alkanethiol monolayers from polycrystalline gold and silver electrodes*, J. Electroanal. Chem. Interfacial Electrochem. **1991**, *310*, 335-359.

(24) Wittstock, G.; Hesse, R.; Schuhmann, W., *Patterned self-assembled alkanethiolate monolayers on gold. Patterning and imaging by means of scanning electrochemical microscopy*, Electroanalysis **1997**, *9*, 746-750.

(25) Wittstock, G.; Schuhmann, W., *Formation and Imaging of Microscopic Enzymically Active Spots on an Alkanethiolate-Covered Gold Electrode by Scanning Electrochemical Microscopy*, Anal. Chem. **1997**, *69*, 5059-5066.

(26) Ammann, E.; Mandler, D., *Local deposition of gold on silicon by the scanning electrochemical microscope*, J. Electrochem. Soc. **2001**, *148*, C533-C539.

(27) Kirchner, C. N.; Szunerits, S.; Wittstock, G., *Scanning electrochemical microscopy (SECM) based detection of oligonucleotide hybridization and simultaneous determination of the surface concentration of immobilized oligonucleotides on gold*, Electroanalysis **2007**, *19*, 1258-1267.

(28) Ku, S.-Y.; Wong, K.-T.; Bard, A. J., *Surface Patterning with Fluorescent Molecules Using Click Chemistry Directed by Scanning Electrochemical Microscopy*, J. Am. Chem. Soc. F **2008**, *130*, 2392-2393.

(29) Sheffer, M.; Mandler, D., *Scanning electrochemical imprinting microscopy: a tool for surface patterning*, J. Electrochem. Soc. **2008**, *155*, D203-D208.

(30) Sugimura, H.; Uchida, T.; Kitamura, N.; Shimo, N.; Masuhara, H., *Direct-mode scanning electrochemical microscopy with three electrodes: application to fluorescent micropattern formation*, J. Electroanal. Chem. **1993**, *361*, 57-63.

(31) Zhou, J.; Wipf, D. O., *Deposition of conducting polyaniline patterns with the scanning electrochemical microscope*, J. Electrochem. Soc. **1997**, *144*, 1202-1207.

(32) Borgwarth, K.; Rohde, N.; Ricken, C.; Hallensleben, M. L.; Mandler, D.; Heinze, J., *Electroless deposition of conducting polymers using the scanning electrochemical microscope*, Adv. Mater. **1999**, *11*, 1221-1226.

(33) Hess, C.; Borgwarth, K.; Ricken, C.; Ebling, D. G.; Heinze, J., *Scanning electrochemical microscopy: study of silver deposition on non-conducting substrates*, Electrochim. Acta **1997**, *42*, 3065-3073.

(34) Turyan, I.; Krasovec, U. O.; Orel, B.; Saraidorov, T.; Reisfeld, R.; Mandler, D., *"Writing-reading-erasing" on tungsten oxide films using the scanning electrochemical microscope*, Adv. Mater. **2000**, *12*, 330-333.

(35) Borgwarth, K.; Rohde, N.; Ricken, C.; Hallensleben, M. L.; Mandler, D.; Heinze, J., *Electroless deposition of conducting polymers using the scanning electrochemical microscope*, Adv. Mater. **1999**, *11*, 1221-1226.

(36) Li, X.; Geng, Q.; Wang, Y.; Si, Z.; Jiang, W.; Zhang, X.; Jin, W., *Micropatterning of active enzyme with a high-resolution by scanning electrochemical microscopy coupled with a nanometer-sized carbon fiber disk tip*, Electrochim. Acta **2007**, *53*, 2016-2024.

(37) Yang, D. F.; Wilde, C. P.; Morin, M., *Electrochemical Desorption and Adsorption of Nonyl Mercaptan at Gold Single Crystal Electrode Surfaces*, Langmuir **1996**, *12*, 6570-6577.

(38) Treutler, T. H.; Wittstock, G., *Combination of an electrochemical tunneling microscope (ECSTM) and a scanning electrochemical microscope (SECM): application for tip-induced modification of self-assembled monolayers*, Electrochim. Acta **2003**, *48*, 2923-2932.

(39) Williams, D. E.; Mohiuddin, T. F.; Zhu, Y. Y., *Elucidation of a trigger mechanism for pitting corrosion of stainless steels using submicron resolution scanning electrochemical and photoelectrochemical microscopy*, J. Electrochem. Soc. **1998**, *145*, 2664-2672.

(40) James, P.; Casillas, N.; Smyrl, W. H., *Simultaneous scanning electrochemical and photoelectrochemical microscopy by use of a metalized optical fiber*, J. Electrochem. Soc. **1996**, *143*, 3853-3865.

(41) Shi, G.; Garfias-Mesias, L. F.; Smyrl, W. H., *Preparation of a gold-sputtered optical fiber as a microelectrode for electrochemical microscopy*, J. Electrochem. Soc. **1998**, *145*, 2011-2016.

(42) Davoodi, A.; Pan, J.; Leygraf, C.; Norgren, S., *In Situ Investigation of Localized Corrosion of Aluminum Alloys in Chloride Solution Using Integrated EC-AFM/SECM Techniques*, Electrochem. Solid-State Lett. **2005**, *8*, B21-B24.

(43) Fasching, R. J.; Tao, Y.; Prinz, F. B., *Cantilever tip probe arrays for simultaneous SECM and AFM analysis*, Sens. Actuators, B **2005**, *B108*, 964-972.

(44) Gullo, M. R.; Frederix, P. L. T. M.; Akiyama, T.; Engel, A.; de Rooij, N. F.; Staufer, U., *Characterization of Microfabricated Probes for Combined Atomic Force and High-Resolution Scanning Electrochemical Microscopy*, Anal. Chem. **2006**, *78*, 5436-5442.

(45) Kranz, C.; Friedbacher, G.; Mizaikoff, B.; Lugstein, A.; Smoliner, J.; Bertagnolli, E., *Integrating an Ultramicroelectrode in an AFM Cantilever: Combined Technology for Enhanced Information*, Anal. Chem. **2001**, *73*, 2491-2500.

(46) Kueng, A.; Kranz, C.; Lugstein, A.; Bertagnolli, E.; Mizaikoff, B., *Integrated AFM-SECM in tapping mode: Simultaneous topographical and electrochemical imaging of enzyme activity*, Angew. Chem., Int. Ed. **2003**, *42*, 3238-3240.

(47) Macpherson, J. V.; Unwin, P. R., *Combined Scanning Electrochemical-Atomic Force Microscopy*, Anal. Chem. **2000**, *72*, 276-285.

(48) Macpherson, J. V.; Unwin, P. R., *Noncontact Electrochemical Imaging with Combined Scanning Electrochemical Atomic Force Microscopy*, Anal. Chem. **2001**, *73*, 550-557.

(49) Shin, M.; Jeon, I. C., *Frequency-distance responses in SECM-EQCM: a novel method for calibration of the tip-sample distance*, Bull. Korean Chem. Soc. **1998**, *19*, 1227-1232.

(50) Cliffel, D. E.; Bard, A. J., *Scanning Electrochemical Microscopy. 36. A Combined Scanning Electrochemical Microscope-Quartz Crystal Microbalance Instrument for Studying Thin Films*, Anal. Chem. **1998**, *70*, 1993-1998.

(51) Gabrielli, C.; Joiret, S.; Keddam, M.; Perrot, H.; Portail, N.; Rousseau, P.; Vivier, V., *A SECM assisted EQCM study of iron pitting*, Electrochim. Acta **2007**, *52*, 7706-7714.

(52) Gollas, B.; Bartlett, P. N.; Denuault, G., *An Instrument for Simultaneous EQCM Impedance and SECM Measurements*, Anal. Chem. **2000**, *72*, 349-356.

(53) Hess, C.; Borgwarth, K.; Heinze, J., *Integration of an electrochemical quartz crystal microbalance into scanning electrochemical microscope for mechanistic studies of surface patterning reactions*, Electrochim. Acta **2000**, *45*, 3725-3736.

(54) Hsu, C.-Y.; Vasantha, V. S.; Ho, K.-C., *A study of ion exchange at the poly(butyl viologen)-electrolyte interface by SECM*, Electrochim. Acta **2008**, *53*, 6244-6251.

(55) Lee, Y.; Bard, A. J., *Fabrication and Characterization of Probes for Combined Scanning Electrochemical/Optical Microscopy Experiments*, Anal. Chem. **2002**, *74*, 3626-3633.

(56) Maruyama, K.; Ohkawa, H.; Ogawa, S.; Ueda, A.; Niwa, O.; Suzuki, K., *Fabrication and Characterization of a Nanometer-Sized Optical Fiber Electrode Based on Selective Chemical Etching for Scanning Electrochemical/Optical Microscopy*, Anal. Chem. **2006**, *78*, 1904-1912.

(57) Boldt, F.-M.; Heinze, J.; Diez, M.; Petersen, J.; Boersch, M., *Real-time pH microscopy down to the molecular level by combined scanning electrochemical microscopy/single-molecule fluorescence spectroscopy*, Anal. Chem. **2004**, *76*, 3473-3481.

(58) Fan, F.-R. F.; Cliffel, D.; Bard, A. J., *Scanning Electrochemical Microscopy. 37. Light Emission by Electrogenerated Chemiluminescence at SECM Tips and Their Application to Scanning Optical Microscopy*, Anal. Chem. **1998**, *70*, 2941-2948.

(59) Kanoufi, F.; Cannes, C.; Zu, Y.; Bard, A. J., *Scanning Electrochemical Microscopy. 43. Investigation of Oxalate Oxidation and Electrogenerated Chemiluminescence across the Liquid-Liquid Interface*, J. Phys. Chem. B **2001**, *105*, 8951-8962.

(60) Miao, W.; Choi, J.-P.; Bard, A. J., *Electrogenerated Chemiluminescence 69: The Tris(2,2'-bipyridine)ruthenium(II), (Ru(bpy)32+)/Tri-n-propylamine (TPrA) System Revisited-A New Route Involving TPrA.bul.+ Cation Radicals*, J. Am. Chem. Soc. **2002**, *124*, 14478-14485.

(61) Szunerits, S.; Walt, D. R., *The use of optical fiber bundles combined with electrochemistry for chemical imaging*, ChemPhysChem **2003**, *4*, 186-192.

(62) Szunerits, S.; Knorr, N.; Calemczuk, R.; Livache, T., *New approach to writing and simultaneous reading of micropatterns: combining surface plasmon resonance imaging with scanning electrochemical microscopy (SECM)*, Langmuir **2004**, *20*, 9236-9241.

(63) Brucherseifer, M.; Kranz, C.; Mizaikoff, B., *Combined in Situ Atomic Force Microscopy- Infrared-Attenuated Total Reflection Spectroscopy*, Anal. Chem. **2007**, *79*, 8803-8806.

(64) Harrick, N. J. *Internal reflection spectroscopy*; Interscience Publishers: New York, 1967.

(65) Dobbs, G. T.; Balu, B.; Young, C.; Kranz, C.; Hess, D. W.; Mizaikoff, B., *Mid-infrared chemical sensors utilizing plasma-deposited fluorocarbon membranes*, Anal. Chem. **007**, *79*, 9566-9571.

(66) Hansen, D. M.; Albaugh, C. E.; Moran, P. D.; Kuech, T. F., *Chemical role of oxygen plasma in wafer bonding using borosilicate glasses*, Appl. Phys. Lett. **2001**, *79*, 3413-3415.

(67) Taft, E. A., *Diffusion of oxygen in silicon thermal oxides*, J. Electrochem. Soc. **1985**, *132*, 2486-2489.

(68) Bard, A. J.; Mirkin, M. V. *Scanning Electrochemical Microscopy*; Marcel Dekker: New York, 2001.

(69) Engstrom, R. C.; Weber, M.; Wunder, D. J.; Burgess, R.; Winquist, S., *Measurements within the diffusion layer using a microelectrode probe*, Anal. Chem. **1986**, *58*, 844-848.

(70) Niziurski-Mann, R. E.; Scordilis-Kelley, C.; Liu, T. L.; Cava, M. P.; Carlin, R. T., *A mechanistic study of the electrochemical oxidation of 2,5-bis(2-thienyl)pyrroles*, J. Am. Chem. Soc. **1993**, *115*, 887-891.

(71) Rudolph, D.; Neuhuber, S.; Kranz, C.; Taillefert, M.; Mizaikoff, B., *Scanning electrochemical microscopy imaging of rhodochrosite dissolution using gold amalgam microelectrodes*, Analyst **2004**, *129*, 443-448.

(72) Ferraris, J. P.; Hanlon, T. R., *Optical, electrical and electrochemical properties of heteroaromatic copolymers*, Polymer **1989**, *30*, 1319-1327.

(73) Wynberg, H.; Metselaar, J., *A convenient route to polythiophenes*, Synth. Commun. **1984**, *14*, 1-9.

(74) Stetter, H., *New synthetic methods. 17. The catalyzed addition of aldehydes to activated double bonds - a new synthesis principle*, Angew. Chem. **1976**, *88*, 695-704.

(75) Ferraris, J. P.; Skiles, G. D., *'Substitutional alloys' of organic polymeric conductors*, Polymer **1987**, *28*, 179-182.

(76) Brillas, E.; Carrasco, J.; Figueras, A.; Urpi, F.; Otero, T. F., *Oxidized and reduced poly(2,5-di(-2-thienyl)pyrrole): solubilities, electrodissolution and molar mass*, J. Electroanal. Chem. **1995**, *392*, 55-61.

(77) Otero, T. F.; Carrasco, J.; Figueras, A.; Brillas, E., *Electrogeneration of poly(2,5-di-(2-thienyl)-pyrrole) in acetonitrile. Kinetics, productivity and composition of the oxidized form*, Synth. Met. **1996**, *83*, 193-196.

(78) Brillas, E.; Carrasco, J.; Oliver, R.; Estrany, F.; Ruiz, V., *Effects of doping on the electrochemical and electrical properties of poly(2,5-di(2-thienyl)pyrrole)*, Collect. Czech. Chem. Commun. **1999**, *64*, 1357-1368.

(79) Carrasco, J.; Brillas, E.; Fernandez, V.; Cabot, P.-L.; Garrido, J. A.; Centellas, F.; Rodriguez, R. M., *Electrical and electrochemical properties of reduced, oxidized, and overoxidized poly[2,5-di(2-thienyl)pyrrole] films in water/acetonitrile mixture*, J. Electrochem. Soc. **2001**, *148*, E19-E25.

(80) Dobbs, G. T.; Mizaikoff, B., *Shining new light on old principles: localization of evanescent field interactions at infrared-attenuated total reflection sensing interfaces*, Appl. Spectrosc. **2006**, *60*, 573-583.

(81) Charlton, C.; Giovannini, M.; Faist, J.; Mizaikoff, B., *Fabrication and characterization of molecular beam epitaxy grown thin-film GaAs waveguides for mid-infrared evanescent field chemical sensing*, Anal. Chem. **2006**, *78*, 4224-4227.

(82) Charlton, C.; Katzir, A.; Mizaikoff, B., *Infrared evanescent field sensing with quantum cascade lasers and planar silver halide waveguides*, Anal. Chem. **2005**, *77*, 4398-4403.

(83) Shin, H.; Hesketh, P. J.; Mizaikoff, B.; Kranz, C., *Batch Fabrication of Atomic Force Microscopy Probes with Recessed Integrated Ring Microelectrodes at a Wafer Level*, Anal. Chem. **2007**, *79*, 4769-4777.

(84) Stoica, L.; Neugebauer, S.; Schuhmann, W., *Scanning elecrochemical microscopy (SECM) as a tool in biosensor research*, Adv. Biochem. Eng./Biotechnol. **2008**, *109*, 455-492.

(85) Roberts, W. S.; Lonsdale, D. J.; Griffiths, J.; Higson, S. P. J., *Advances in the application of scanning electrochemical microscopy to bioanalytical systems*, Biosens. Bioelectron. **2007**, *23*, 301-318.

(86) Bard, A. J.; Li, X.; Zhan, W., *Chemically imaging living cells by scanning electrochemical microscopy*, Biosens. Bioelectron. **2006**, *22*, 461-472.

(87) Fortin, E.; Chane-Tune, J.; Delabouglise, D.; Bouvier, P.; Livache, T.; Mailley, P.; Marcus, B.; Mermoux, M.; Petit, J.-P.; Szunerits, S.; Vieil, E., *Interfacing boron doped diamond and biology: an insight on its use for bioanalytical applications*, Electroanalysis **2005**, *17*, 517-526.

CHAPTER 5

UME APPROACH MONITORED BY EVANESCENT FIELD ABSORPTION

This chapter presents a novel method for monitoring the relative position of an UME to the IR transparent substrate *via* evanescent field absorption based on the combined SECM-IR-ATR instrument, along with mathematical modeling of the UME approach curve in the evanescent field.

5.1 Motivation

In conventional SECM experiments, positioning of the UME is achieved by monitoring the Faradic current measured at the UME as the UME approaches to the sample surface or substrate.[1] However, this positioning method is limited to amperometric experiments, and requires an UME tip with a well-defined geometry. In addition, the estimation of Faradic current-correlated approach distance is difficult to be determined when the current is affected both by the morphology and the electroconductivity of samples/substrates. As amperometric approaches in SECM utilizing the analytical signal (Faradaic current) itself for determining the electrode-substrate distance render precise positioning of UMEs challenging, alternative positioning techniques independent of the current signal are of significant interest. Single-bounce attenuated total reflection infrared spectroscopy has been combined with scanning electrochemical microscopy (SECM) in this thesis for *in situ* spectroscopic detection of electrochemically induced localized surface modifications using an ultramicroelectrode (UME).[2] The principle of combined

SECM-IR-ATR has been discussed in detail in Chapter 4. This combined instrument has the potential to provide a novel method for controlling the distance between electrode and substrate during the approach independent of the recorded Faradic current. Once the UME penetrates the exponentially decaying evanescent field in close vicinity (several µm) above the ATR crystal surface, the resulting intensity changes of the absorption spectrum characteristic for the borosilicate glass (BSG) sheath insulating the electrode (or of the surrounding displaced matrix, i.e., usually aqueous electrolyte solution) may be correlated with the position of the UME relative to the ATR crystal surface.

5.2 Introduction

With the demonstrated combination of SECM with spectroscopic techniques in the mid-infrared wavelength region within this thesis, it is evident that the SECM-IR-ATR combination could provide a novel current-independent method for positioning the ultramicroelectrode.

During conventional SECM experiment, positioning of the UME is achieved by monitoring the Faradic current measured at the UME once the UME approaches the sample surface within ~ 100µm. Several mathematical models describe in detail such theoretical approach curves, and enable predicting the distance based on the feedback current for electrodes with a wide variety of different geometries approaching samples/substrates with different electroconductivities.[3-11] However, positioning *via* the redox current is limited to amperometric experiments, requires an UME tip with a rather well-defined geometry, and presumes that no other processes are contributing to the observed changes of the Faradic current during the approach. Early non-amperometric approaches for determining the UME distance were based on the measurement of solvent resistance, once the UME tip is close to the sample surface.[12, 13] Later, shear-force based UME positioning – as derived from locating NSOM probes - has been investigated in SECM [14-16] detecting the changes of the shear-force at the tip in close proximity to the sample surface. Shear-force based positioning has nowadays matured into the most commonly utilized non-amperometric method for controlling the distance between tip and sample during conventional SECM imaging. In recent years, combined AFM-SECM probes have been developed for directly correlating surface morphological information with (electro)chemical activity.[17-23] In this case, the distance between electrode and sample surface is well defined by the AFM tip, which acts as a deliberately selected spacer locating and maintaining the electrode at its optimum working distance. The combined SECM-IR-ATR instrument developed in this thesis offers an alternative method for controlling the approach of the electrode to the sample without using the Faradic current. A scheme for the principle of developed dual instrument is shown in **Figure 5.1**.

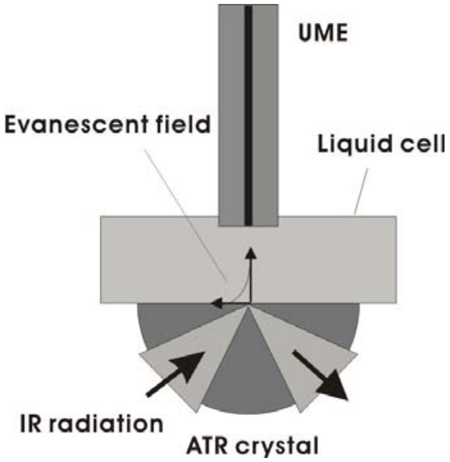

Figure 5.1: Demonstration of the principle of SECM-IR-ATR.

IR-ATR is an attractive IR measurement technique due to its localized surface sensitivity.[24] Strong IR absorbers, such as water, have minimum adverse effect on the IR-ATR measurement compared to transmission and reflection IR spectroscopies, due to the limited probed volume determined by the penetration depth of the evanescent field. Details of evanescent field spectroscopy are provided in Chapter 2 of this thesis. The evanescent wave intensity exponentially decays with increasing distance to the interface, and its penetration depth is typically in the range of a few micrometers (μm) in the MIR regime. Hence, IR absorbing materials or molecules within this evenascent field can be detected by ATR measurements.[24] The sheath of the UME in our study is made from borosilicate glass (BSG), which has several strong and characteristic IR absorption features in the regime 1600-700cm^{-1},[25, 26] such as the B-O stretching vibration at 1380cm^{-1}, the Si-O stretch at 1130 and 875cm^{-1}, and the Si-O bending feature at 760cm^{-1}. If the UME approaches the substrate and penetrates the evanescent field, the IR features of BSG should be detected by the IR-ATR measurement. In addition, with decreasing distance of the UME to the substrate within the evanescent field (i.e., increasing "volume" of UME within the evanescent field vs. e.g., displaced electrolyte solution), the IR intensity of the BSG features should increase, or absorption features of the displaced solution should accordingly decrease.

In this presented IR-ATR approach study, UME approaches to the IR transparent substrate (ATR waveguide) were investigated both at ambient conditions, and in aqueous electrolyte solution. The experimentally obtained IR-ATR data were fitted with a mathematical model derived for the increasing volume of absorbing material within an exponentially decaying evanescent field, and the penetration depths at the selected characteristic wavenumbers. Finally, conventional UME approach curves in solution using the Faradaic current were compared with spectroscopically obtained position information.

5.3 Background

For the fundamentals on IR-ATR and SECM, respectively, please consult the corresponding sections in Chapter 2 and Chapter 4 of this thesis.

5.4 Mathematical Modeling of the UME Approach within the Evanescent Field at Hemispherical IR-ATR Waveguides

A mathematical model of the expected IR absorption changes resulting from the approaching UME *vs.* the distance between UME tip and the surface of the ATR waveguide was derived based on the Lambert-Beer law, and the exponential decay of the evanescent field intensity. Subsequently, this model was used to fit the experimental IR-ATR data obtained in section 5.5.

The IR absorption (A) of an analyte or material within the evanescent field is theoretically described by the Lambert-Beer law:

$$A = \varepsilon l c$$

Eq.5.1

where ε represents the absorptivity of the sample, l is the optical length (thickness) of the sample, and c is the concentration of sample. IR absorption is also proportional to the light source intensity following $-\log I/I_0$ (I – detected radiation intensity after radiation interacts with sample; I_0 – radiation intensity before radiation interacts with sample) If total internal reflection occurs, the electromagnetic field (E) leaking into the adjacent medium[24] is not constant, but follows an exponential decay. Hence, the Lambert-Beer law (**Eq.5.1**) has been modified by a correction term E/E_0 taking into account the change in effective absorption, as the absorbing material (here the UME) is present at an increasing distance from the waveguide surface (i.e., at the surface of the waveguide $E_0 = E$; hence, $E/E_0 = 1$, and the initial expression of the Lambert-Beer law (**Eq.5.1**) is reestablished):

$$A_{IRATR} = \frac{E}{E_0}\varepsilon lc$$

Eq.5.2

where E is the intensity of light in the evanescent field, and E_0 is the light intensity at the surface of ATR waveguide. Their relationship can be described by[24]:

$$E = E_0 e^{\left(\frac{-z}{d_p}\right)}$$

Eq.5.3

where z is the distance from the ATR waveguide surface within the adjacent medium. Replace E in **Eq.5.2** with **Eq.5.3** results in:

$$A_{IRATR} = e\left(\frac{-z}{d_p}\right)\varepsilon lc$$

Eq.5.4

It is evident from **Eq.5.4** that the IR absorption is a function of the sample thickness l, and the distance z. **Figure 5.2** schematically shows the adjacent medium represented by a cylinder with bottom radius r_{ATR} and height d_{max}, into which the UME penetrates as it approaches to the ATR crystal surface. r_{ATR} is the radius of the sensing area of the hemispherical ATR crystal; d_{max} is the minimum distance from the ATR crystal surface where no IR absorption from the UME is detectable *via* IR evanescent field spectroscopy (i.e., the UME is just outside the evanescent field).

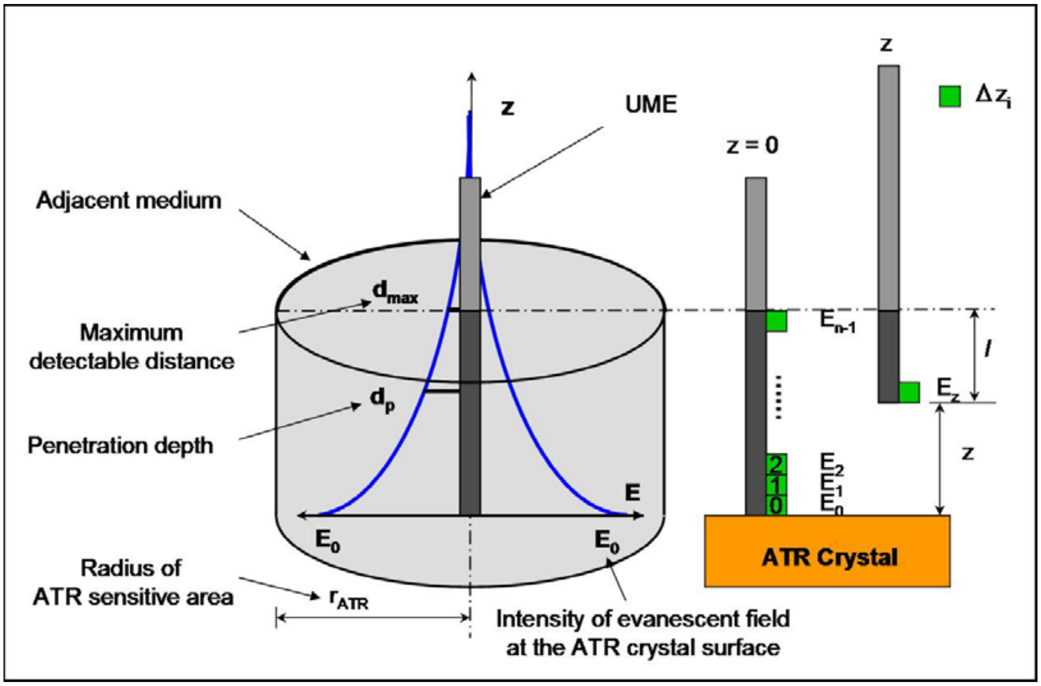

Figure 5.2: Fundamental considerations for modeling the approach of an UME into the evanescent field emanating from a hemispherical ATR crystal surface.

If the UME approaches and penetrates the evanescent field, the IR absorption specific to the UME will change with the UME position due to the change of the evanescent field intensity, as well as the "volume of UME" increasingly present within the evanescent field. **Eq.5.4** can therefore be rewritten as:

$$\begin{aligned} A_{IRATR} &= \sum_{i=0}^{i} e^{-z_i/d_p} \cdot \varepsilon \Delta z_i c \\ &= \int_{z}^{d_{\max}} K e^{-z_i/d_p} \cdot dz \\ &= K(e^{-z/d_p} - e^{-d_{\max}/d_p}) \\ &= P e^{-z_i/d_p} - Q \end{aligned}$$

Eq.5.5

where K, P, and Q are constants, and d_{max} and d_p are assumed constants that will not change with of the UME approaching the waveguide surface. This model reflects that the IR absorption exponentially decays with increasing distance between the UME tip, and the ATR crystal surface.

5.5 Experimental

5.5.1 Instrumental - Combined SECM-IR-ATR Set-up.

The details for this instrumental combination are described in Chapter 4. In brief, broad-band IR radiation from a FT-IR spectrometer (IRCube-M, Bruker Optics Inc., Billerica, MA) is collimated and focused by an off-axis parabolic mirror (OAPM) onto the curvature of a single-bounce hemispherical ZnSe ATR crystal (3mm in diameter, Harrick Scientific, Pleasantville, NY). The internally reflected beam from the top flat surface of the ATR crystal is then collimated by a second OAPM, and focused by a third OAPM onto a liquid-nitrogen cooled mercury-cadmium-telluride (MCT) detector. The ATR crystal waveguide is built into the electrochemical cell as central part of base plate (**Figure 4.7**, Chapter 4). The micropositioning system moving the microelectrode over the fixed ATR crystal is part of a home-built SECM driven by stepper motors (Scientific

Precision Instruments GmbH®, Oppenheim, Germany) with a precision of 0.02μm, and correlated with the positioning of the UME using an A/D-D/A board (DAS 1602-16, Plug-In-Electronic, Eichenau, FRG). All electrochemical experiments are conducted with a CHI 842A potentiostat (CH Instruments, Inc., Austin, TX). The entire combined SECM-IR-ATR system was placed in a dark flexible plastic box, and purged with nitrogen to maintain an inert and constant atmosphere for the IR measurements. All IR spectra obtained using the SECM-IR-ATR platform were collected at a resolution of $4cm^{-1}$, and by averaging 64 scans, and have been analyzed with the OPUS software package.

5.5.2 UME Preparation

Disk–shaped microelectrodes were fabricated as previously described[1] by sealing a 25μm (diam.) Pt wire under vacuum into a borosilicate glass capillary. Successive grinding with diamond paste (6μm and 3μm), and polishing with alumina paste (1μm and 0.05μm), respectively, exposes a disk-shaped microelectrode. Characterization of the UME was performed by optical microscopy and cyclic voltammetry.

5.5.3 Chemicals

$Ru(bpy)_3Cl_2 \cdot 6H_2O$ and KCl (Reagent grade) were obtained from Sigma Aldrich (St. Louis, MO). 0.02M $Ru(bpy)_3Cl_2$ / 0.1M KCl electrolyte solution was prepared in deionized H_2O (Milli-Q water system, Millipore Corp., Billerica, MA). All solutions were deoxygenated by purging with UHP argon (Airgas, Hapeville, GA) prior to electrochemical experiments.

5.5.4 Conventional UME Approach via Amperometric SECM

Experiments were performed in a Faraday cage using a three-electrode configuration with a disk-shaped 25μm (diam.) Pt UME as working electrode, a 1mm (diam.) Pt auxiliary electrode, and an Ag/AgCl quasi reference electrode. The approach current was recorded by applying a constant potential of 1.13V *vs.* Ag/AgCl with other approach parameters set as: scanning speed 1.6μm/s, and data recording interval: 0.4μm.

5.5.5 UME Approach via IR-ATR Spectroscopy in Air

Experiments were performed at ambient conditions. The 25μm (diam.) Pt UME was aligned with the center of the ATR crystal by the precisely controlled micropositioning system, penetrated into the evanescent field by incremental movement toward the surface, and stopped at the surface of the ATR element. The corresponding series of IR absorption spectra was recorded at 0.2μm intervals during the UME approaching the ATR surface.

5.5.6 UME Approach via IR-ATR Spectroscopy in Aqueous Electrolyte Solution

Experiments were performed in 0.02M $Ru(bpy)_3Cl_2$ / 0.1M KCl/H_2O electrolyte solution. The 25μm (diam.) Pt UME was aligned with the center of the crystal, then incrementally penetrated into the evanescent field, and stopped at the surface of the ATR waveguide. The corresponding series of IR absorption spectra in electrolyte solution was recorded at 0.4μm intervals during the UME approaching the ATR surface.

5.6 Results and Discussion

Figure 5.3 shows an example of a series of IR spectra for an UME penetrating the evanescent field in air. The IR features of BSG were observed at different wavenumbers such as the B-O stretch at 1380cm^{-1}, the Si-O stretch at 1130 and 976cm^{-1}, and the Si-O bend at 760cm^{-1}. [25, 26]

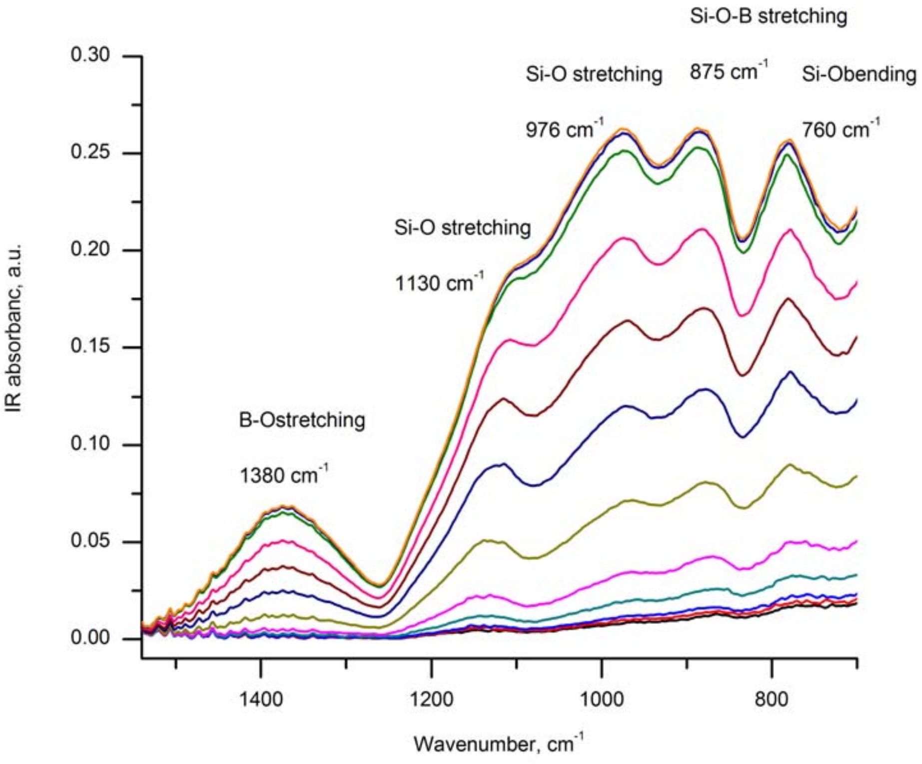

Figure 5.3: IR absorption spectra of an UME approaching the ATR crystal surface and penetrating the evanescent field in air.

With the UME approaching to the ATR surface, the absorption intensities for different features clearly increase, and eventually reach a maximum once the UME tip touches the ATR crystal surface (last three spectra in **Figure 5.3**). The last two IR spectra overlap each other, which indicates that the UME is in contact with the ATR crystal surface.

However, the absorptions are slightly larger than observed in the third spectrum to the last, which may result from UME tilting effects, as the UME tip surface may not be perfectly parallel to the ATR crystal surface. Consequently, further movement downwards increases the contact between the UME and ATR crystal surface due to tilting; therefore, stronger IR absorptions are obtained. Two wavenumbers (1380cm^{-1} and 976cm^{-1}) were selected for plotting an IR-ATR approach curve of the UME in air, as shown in **Figure 5.4** and **Figure 5.5**. The error bars in both approach curves were calculated based on the results of three consecutive experiments of UME approaches in air. The experimental approach curves were fitted with the mathematical model developed (**Eq.5.5**), and were in excellent agreement.

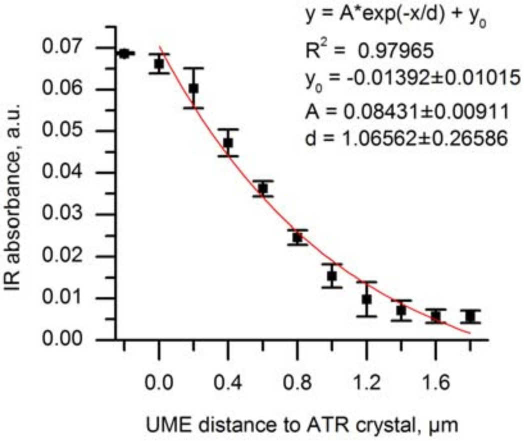

Figure 5.4: IR-ATR approach curve with model fitting at 1380cm^{-1} for BSG B-O stretch.

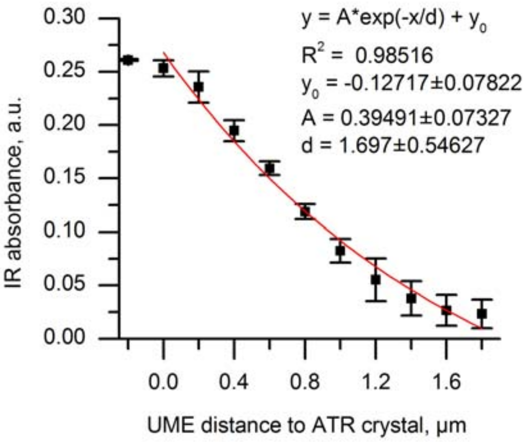

Figure 5.5: IR-ATR approach curve with model fitting at 976cm^{-1} for BSG Si-O bend.

Three consecutive approach experiments were also performed in a 0.02M Ru(bpy)$_3$Cl$_2$ / 0.1M KCl/H_2O electrolyte solution. A representative series of IR measurement results of one approach are displayed in **Figure 5.6**. As expected, the IR absorption intensities of characteristic water peaks, and of the UME absorption features all changed with respect to the relative position of the UME *vs.* the ATR crystal surface.

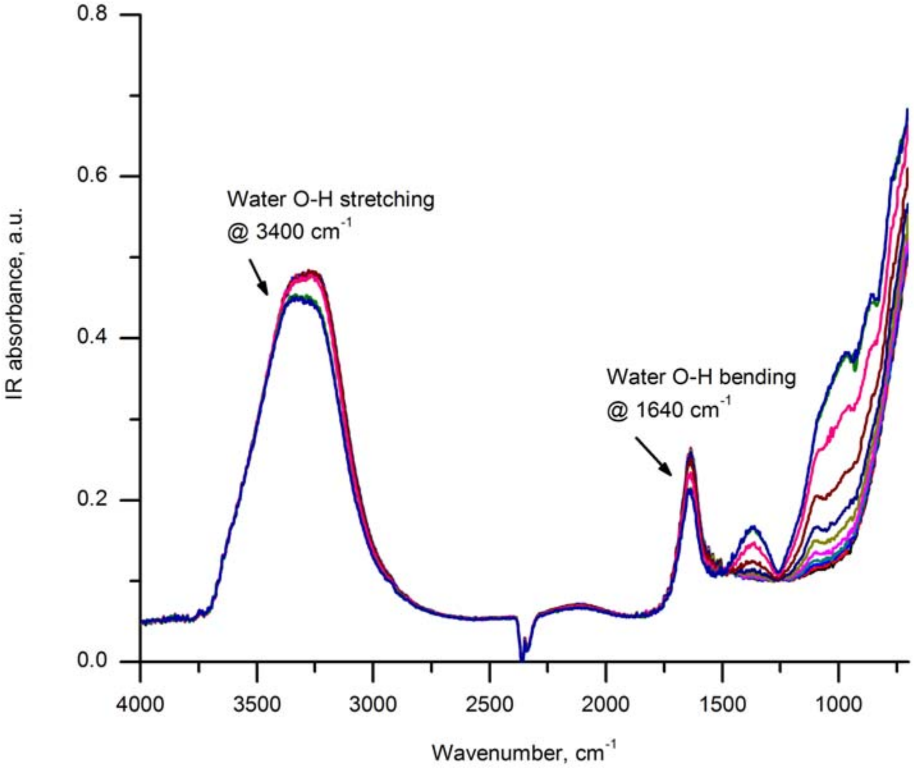

Figure 5.6: IR absorption spectra of the UME approach with IR-ATR in 0.02M $Ru(bpy)_3Cl_2$ / 0.1M KCl/ H_2O electrolyte solution.

The regions in **Figure 5.6** around 1640cm^{-1} and 1500-700cm^{-1} are magnified in **Figure 5.7** and **Figure 5.8**. **Figure 5.7** displays the changes of the O-H bend of water at 1640cm^{-1} during the approach of the UME.

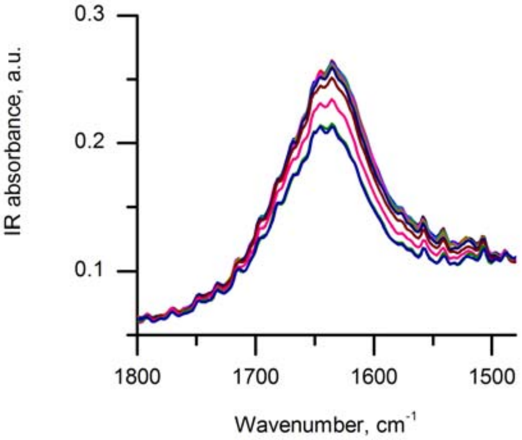

Figure 5.7: UME approach spectra at 1640 cm^{-1} for the water O-H bend in 0.02M Ru(bpy)$_3$Cl$_2$ / 0.1M KCl/ H_2O electrolyte solution.

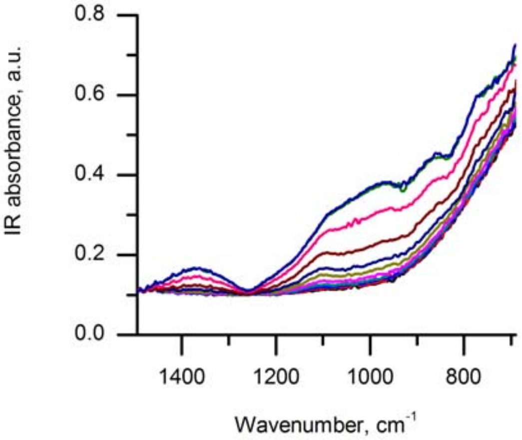

Figure 5.8: UME approach spectra in the region 1500-700cm^{-1} for UME absorption features in 0.02M Ru(bpy)$_3$Cl$_2$ / 0.1M KCl/ H_2O electrolyte solution.

Figure 5.8 displays the most of IR features of the BSG sheath of the UME that are located on the shoulder of the water libration mode in the range 1200–700cm^{-1}.The BSG IR signals increased with decreasing distance between UME and ATR crystal in the evanescent field, in contrast to the water IR signals, which decreased with the decreasing distance. This is expected, as the same volume of water was excluded from the adjacent medium that was introduced by the volume of the UME penetrating the evanescent field. The water feature at 1640cm^{-1} was selected to plot the corresponding IR-ATR approach curve in aqueous electrolyte solution.

The BSG feature at 1380cm^{-1} was selected due to the IR transparent window of water in this spectral region; consequently, no interference from water absorptions should affect the B-O peak evaluation at this wavenumber. The IR absorption spectrum of 0.02M $Ru(bpy)_3Cl_2$ / 0.1M KCl/ H_2O was recorded as reference spectrum with the UME located beyond the evanescent field. The absolute changes of IR absorbance at wavenumbers 1640cm^{-1} and 1380cm^{-1} during approach experiments were used to plot IR-ATR approach curves at these frequencies, respectively. Both experimental approach curves were fitted with the developed mathematical model **Eq.5.5**, and show excellent agreement. The corresponding experimental data with curve fitting results are displayed in **Figure 5.9** and **Figure 5.10**.

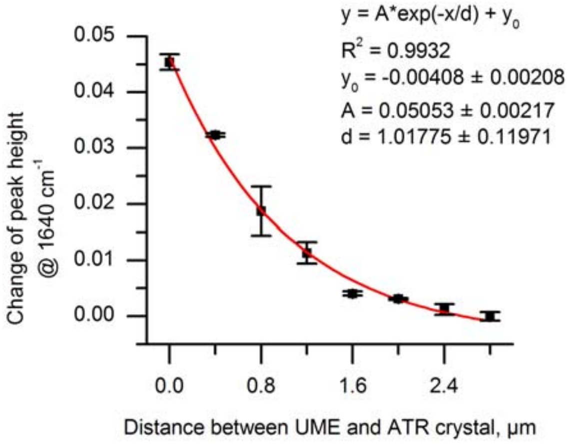

Figure 5.9: IR-ATR approach curve with fitted model for water O-H bend at 1640cm^{-1}.

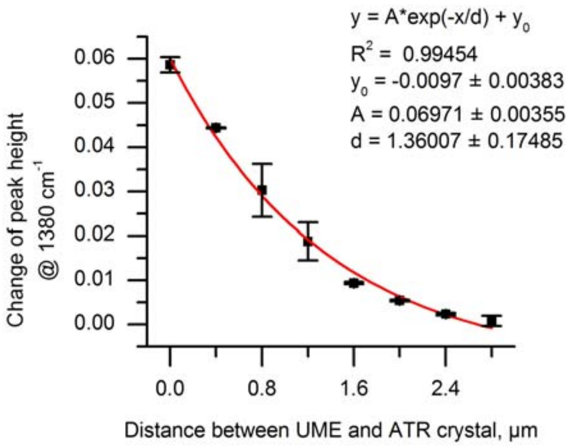

Figure 5.10: IR-ATR approach curve with fitted model for BSG Bi-O stretch at 1380cm^{-1}.

The values for the penetration depth derived from the model fitted to the IR-ATR experimental data were compared to the values calculated using the theoretical equation[24] developed by Harrick:

$$d_p = \frac{\lambda}{2\pi\sqrt{n_1^2 \sin(\theta) - n_2^2}}$$

Eq.5.6

where λ is the wavelength of light, n_1 is the refractive index of the ATR waveguide, n_2 is the refractive index of the sample ($n_1 > n_2$), and θ is the incident angle.

To simplify the calculations of the penetration depths at the selected wavenumbers (1640cm^{-1}, 1380cm^{-1}, and 976cm^{-1}) the refractive indices of pure BSG (1.5), water (1.3), and air (1.0) were used. The results derived from experimental data and theoretical calculations comply well, and are summarized in **Table 5.1**.

Table 5.1: Comparison of penetration depths: mathematical model fitted experimental results *vs.* theoretically calculated results.

		1640 cm^{-1} height	1380 cm^{-1} height	976 cm^{-1} height
Mathematical model fitted experimental penetration depth $A_{IRATR} = Pe^{-z_i/d_p} - Q$	Approach in air		1.07	1.70
	Approach In H2O	1.02	1.36	
Theoretically calculated penetration depth $d_p = \frac{\lambda}{2\pi\sqrt{n_1^2\sin(\theta) - n_2^2}}$	UME, n_2=1.5, n_1=2.4	1.22	1.45	2.05
	H2O, n_2=1.3, n_1=2.4	0.89	1.06	
	air, n_2=1, n_1=2.4		0.84	1.19

Model fitted experimental penetration depth results were located between two calculated penetration depth results using either pure BSG or pure water as rare medium in experiment of UME approach in aqueous electrolyte solution. The same observation was obtained for a trial of the UME approach in air. The variations between the model fitted experimental and theoretically calculated values may come from the assumption and simplification on the refractive indices of rare medium.

Figure 5.11 shows a conventional amperometric SECM approach curve toward a ZnSe substrate recorded in 0.02M Ru(bpy)$_3$Cl$_2$ / 0.1M KCl/H$_2$O electrolyte solution. The UME is usually stopped at a position where the Faradic current drops by about 20-30% of the bulk current during amperometric SECM experiments, in order to avoid damage of UME tip/sample by touching the sample surface. At this value, the electrode is approximately 30μm away from the substrate surface, as indicated by the red arrow in **Figure 5.11**. **Figure 5.12** shows the correlation of the feedback mode SECM approach curve *vs.* the IR-ATR determined approach curve in 0.02M Ru(bpy)$_3$Cl$_2$ / 0.1M KCl/H$_2$O electrolyte

IR-ATR determined approach curve in 0.02M Ru(bpy)$_3$Cl$_2$ / 0.1M KCl/H$_2$O electrolyte solution using the same BSG-shielded UME. Both approach curves display excellent prediction on the UME distance to the ATR crystal surface within the evanescent field, which extends approx. ~3 µm into the electrolyte solution.

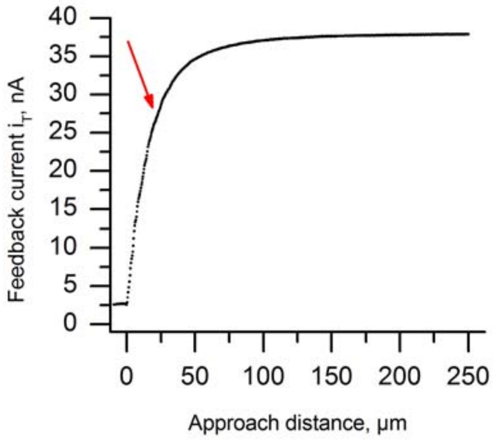

Figure 5.11: Amperometric SECM approach curve to ZnSe substrate in 0.02M Ru(bpy)$_3$Cl$_2$ / 0.1M KCl/H$_2$O electrolyte solution.

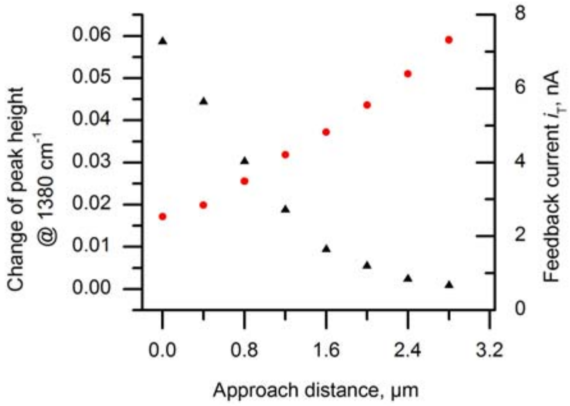

Figure 5.12: Correlation of SECM and IR-ATR approach curves within 3 µm distance to the waveguide substrate. Black triangles – IR-ATR; red dots – amperometric SECM.

5.7 Conclusions

In this study, attenuated total reflection infrared spectroscopy (IR-ATR) was successfully applied to monitor the approach of an ultramicroelectrode (UME) approach toward an IR transparent ATR waveguide (ZnSe) within the penetration depth of the evanescent field. A mathematical model was derived and fitted to the experimental data revealing excellent agreement. Furthermore, the penetration depths derived from the IR-ATR approach experiments comply well with theoretically calculated values. In addition, the IR-ATR approach provided excellent correlation within the evanescent field with feedback mode SECM approach curves recorded in electrolyte solution at the same UME. This novel current-independent UME approach method can be used to position UMEs during non-amperometric SECM experiments, if a combined SECM-IR-ATR platform is used. In addition, the resolution for SECM experiments may be improved upon confined diffusion by reducing the distance between UME tip and substrate given the fidelity of the distance determination via the evanescent field. Finally, the developed IR-ATR approach method is expected to provide enhanced control of the sample-UME distance when additional electroconductivity/electro-reactivity effects convolute the conventionally used amperometric signal.

5.8 Outlook

5.8.1 UME Approach Monitoring via IR-ATR Spectroscopy in Different Solvents

The developed method of IR-ATR monitoring of the UME approach during SECM experiments in aqueous electrolyte solution may also be applied to other solvents, as long as an adequate IR transparent window with respect to the UME material is provided such as e.g., deuterated water (**Figure 5.13**), or organic solvents, such as deuterated acetonitrile (**Figure 5.14**).

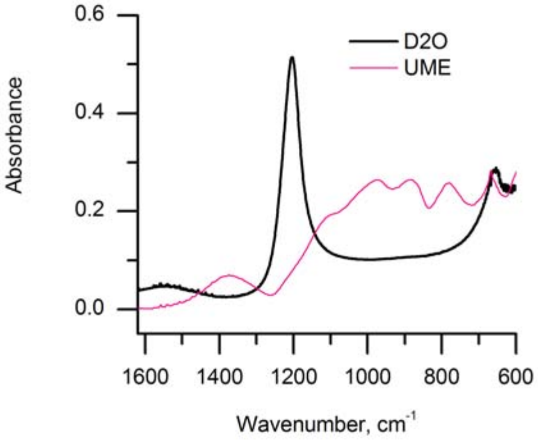

Figure 5.13: IR spectra comparison of BSG shielded UME and deuterated water (D_2O).

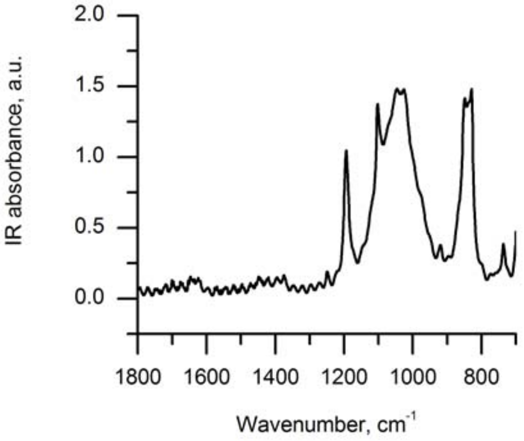

Figure 5.14: IR spectrum of deuterated acetonitrile.

5.9 Reference

(1) Bard, A. J.; Mirkin, M. V. *Scanning Electrochemical Microscopy*; Marcel Dekker: New York, 2001.

(2) Wang, L.; Kowalik, J.; Mizaikoff, B.; Kranz, C. Combination of scanning electrochemical microscopy with infrared attenuated total reflection spectroscopy for in situ investigation of electrochemically induced processes, Anal. Chem., submitted **2008**.

(3) Amphlett, J. L.; Denuault, G. *Scanning Electrochemical Microscopy (SECM): An Investigation of the Effects of Tip Geometry on Amperometric Tip Response*, J. Phys. Chem. B **1998**, *102*, 9946-9951.

(4) Shao, Y.; Mirkin, M. V. *Probing Ion Transfer at the Liquid/Liquid Interface by Scanning Electrochemical Microscopy (SECM)*, J. Phys. Chem. B **1998**, *102*, 9915-9921.

(5) Fulian, Q.; Fisher, A. C.; Denuault, G. *Applications of the Boundary Element Method in Electrochemistry: Scanning Electrochemical Microscopy*, J. Phys. Chem. B **1999**, *103*, 4387-4392.

(6) Selzer, Y.; Mandler, D. *Scanning Electrochemical Microscopy. Theory of the Feedback Mode for Hemispherical Ultramicroelectrodes: Steady-State and Transient Behavior*, Anal. Chem. **2000**, *72*, 2383-2390.

(7) Liljeroth, P.; Johans, C.; Slevin, C. J.; Quinn, B. M.; Kontturi, K. *Disk-Generation/Ring-Collection Scanning Electrochemical Microscopy: Theory and Application*, Anal. Chem. **2002**, *74*, 1972-1978.

(8) Sklyar, O.; Wittstock, G. *Numerical Simulations of Complex Nonsymmetrical 3D Systems for Scanning Electrochemical Microscopy Using the Boundary Element Method*, J. Phys. Chem. B **2002**, *106*, 7499-7508.

(9) Sklyar, O.; Ufheil, J.; Heinze, J.; Wittstock, G. *Application of the boundary element method numerical simulations for characterization of heptode ultramicroelectrodes in SECM experiments*, Electrochim. Acta **2003**, *49*, 117-128.

(10) Zoski, C. G.; Liu, B.; Bard, A. J. *Scanning Electrochemical Microscopy: Theory and Characterization of Electrodes of Finite Conical Geometry*, Anal. Chem. **2004**, *76*, 3646-3654.

(11) Combellas, C.; Fuchs, A.; Kanoufi, F. *Scanning Electrochemical Microscopy with a Band Microelectrode: Theory and Application*, Anal. Chem. **2004**, *76*, 3612-3618.

(12) Wipf, D. O.; Bard, A. J.; Tallman, D. E. *Scanning electrochemical microscopy. 21. Constant-current imaging with an autoswitching controller*, Anal. Chem. **1993**, *65*, 1373-1377.

(13) Alpuche-Aviles, M. A.; Wipf, D. O. *Impedance Feedback Control for Scanning Electrochemical Microscopy*, Anal. Chem. **2001**, *73*, 4873-4881.

(14) Buchler, M.; Kelley, S. C.; Smyrl, W. H. *Scanning electrochemical microscopy with shear force feedback. Investigation of the lateral resolution of different experimental configurations*, Electrochem. Solid-State Lett. **2000**, *3*, 35-38.

(15) Katemann, B. B.; Schulte, A.; Schuhmann, W. *Constant-distance mode scanning electrochemical microscopy (SECM)-part I: Adaptation of a non-optical shear-force-based positioning mode for SECM tips*, Chem.--Eur. J. **2003**, *9*, 2025-2033.

(16) Etienne, M.; Anderson, E. C.; Evans, S. R.; Schuhmann, W.; Fritsch, I. *Feedback-Independent Pt Nanoelectrodes for Shear Force-Based Constant-Distance Mode Scanning Electrochemical Microscopy*, Anal. Chem. **2006**, *78*, 7317-7324.

(17) Macpherson, J. V.; Unwin, P. R. *Combined Scanning Electrochemical-Atomic Force Microscopy*, Anal. Chem. **2000**, *72*, 276-285.

(18) Macpherson, J. V.; Unwin, P. R. *Noncontact Electrochemical Imaging with Combined Scanning Electrochemical Atomic Force Microscopy*, Anal. Chem. **2001**, *73*, 550-557.

(19) Kranz, C.; Friedbacher, G.; Mizaikoff, B.; Lugstein, A.; Smoliner, J.; Bertagnolli, E. *Integrating an Ultramicroelectrode in an AFM Cantilever: Combined Technology for Enhanced Information*, Anal. Chem. **2001**, *73*, 2491-2500.

(20) Kueng, A.; Kranz, C.; Lugstein, A.; Bertagnolli, E.; Mizaikoff, B. *Integrated AFM-SECM in tapping mode: Simultaneous topographical and electrochemical imaging of enzyme activity*, Angew. Chem., Int. Ed. **2003**, *42*, 3238-3240.

(21) Davoodi, A.; Pan, J.; Leygraf, C.; Norgren, S. *In Situ Investigation of Localized Corrosion of Aluminum Alloys in Chloride Solution Using Integrated EC-AFM/SECM Techniques*, Electrochem. Solid-State Lett. **2005**, *8*, B21-B24.

(22) Fasching, R. J.; Tao, Y.; Prinz, F. B. *Cantilever tip probe arrays for simultaneous SECM and AFM analysis*, Sens. Actuators **2005**, *B108*, 964-972.

(23) Gullo, M. R.; Frederix, P. L. T. M.; Akiyama, T.; Engel, A.; de Rooij, N. F.; Staufer, U. *Characterization of Microfabricated Probes for Combined Atomic Force and High-Resolution Scanning Electrochemical Microscopy*, Anal. Chem. **2006**, *78*, 5436-5442.

(24) Harrick, N. J. *Internal Reflection Spectroscopy*; Interscience Publishers: New York, 1967.

(25) Hansen, D. M.; Albaugh, C. E.; Moran, P. D.; Kuech, T. F. *Chemical role of oxygen plasma in wafer bonding using borosilicate glasses*, Appl. Phys. Lett. **2001**, *79*, 3413-3415.

(26) Taft, E. A. *Diffusion of oxygen in silicon thermal oxides*, J. Electrochem. Soc. **1985**, *132*, 2486-2489.

CHAPTER 6
CONCLUSIONS AND OUTLOOK

The main goals of this thesis were the development and application of IR-ATR spectroscopy for monitoring biological/biomedical sample systems *in situ*. The hollow waveguide IR-ATR (HWG-IR-ATR) was for the first time combined with multivariate data analysis techniques for classification of aorta tissue, and has successfully been applied to the identification of lesion and normal rabbit aorta tissue samples.

In addition, the first combination of SECM-IRATR was developed toward *in-situ* biological sample system studies, and its capabilities have been demonstrated by simultaneously *in situ* optically monitoring the locally induced polymerization process of dithiophenylpyrrole (SNS) by feedback mode SECM. In a related study, the novel current-independent monitoring of the UME approach to the IR transparent substrate has been established.

The next steps to continue the research on discriminating rabbit aorta tissues *via* the combination of HWG-IR-ATR and multivariate data analysis, and to study the application of combination of AECM-IRATR on the biological/organic sample systems were described at the ends of chapter 3, and chapter 4 & 5, respectively.